ENGINEERING STEM CELL RESPONSES WITH TWO-DIMENSIONAL NANOMATERIALS

A Dissertation

by

JAMES KENNING CARROW

Submitted to the Office of Graduate and Professional Studies of
Texas A&M University
in partial fulfillment of the requirements for the degree of

DOCTOR OF PHILOSOPHY

Chair of Committee,	Akhilesh K. Gaharwar
Committee Members,	Roland R. Kaunas
	Melissa A. Grunlan
	Ashlee E. Watts
Head of Department,	Michael J. McShane

August 2018

Major Subject: Biomedical Engineering

ABSTRACT

Two-dimensional (2D) nanomaterials are an emerging class of biomaterials that have garnered unprecedented attention due to their unique atomically thin, layered, and well-defined structure. These nanomaterials, however, have limited investigations into their cytocompatibility and potential use in regenerative medicine particularly from the perspective of 3D scaffolds. Here we report two chemically unique 2D nanomaterials and their biophysical and biochemical interactions with stem cells. The first is a naturally occurring nanosilicate which is made up of a unique combination of minerals (Na^+, Li^+, Mg^{2+}, $Si(OH)_4$) within an octahedral sheet sandwiched between two tetrahedral lattices (Laponite XLG®). The second is a transition metal dichalcogenide (TMD) of molybdenum disulfide (MoS_2) which forms 2D sheets nanometers in thickness. Using molecular biology techniques that capture a holistic snapshot of cell signaling, like RNA-sequencing (RNA-seq), we can begin to examine mechanisms behind changes in behavior. With this information, we can then interrogate specific pathways of interest to generate a desired cell response. Furthermore, we can incorporate these nanomaterials into polymeric scaffolds to localize both cells and bioactive materials for delivery *in vivo*. Specifically, we utilized formulations of the polysaccharide kappa-Carrageenan with the nanosilicates and a thiol-modified 4-arm polyethylene glycol (PEG) with 2D MoS_2. Using these studies as a framework, researchers can begin to tailor new polymeric scaffolds around emergent 2D nanomaterials for a variety of regenerative applications including bioprinting.

ACKNOWLEDGEMENTS

First, I would like to thank my family for all of the support and feigning excitement over the smallest of project developments. They have helped immensely throughout my time in grad school from an emotional and academic perspective. They literally helped to set up my life in College Station and put me on track to succeed.

I would like to thank my advisor Dr. Akhilesh Gaharwar. Being able to join you from the beginning has been an extremely valuable experience for me as I look forward to my career. Additionally, I would like to thank my committee members: Dr. Roland Kaunas, Dr. Melissa Grunlan, and Dr. Ashlee Watts. It was a pleasure speaking to each of you both in research and personal capacities throughout the program.

Thank you to the Gaharwar Lab students that have been extremely supportive in a capacity well beyond research. Specifically C.W. Peak and Lauren Cross, you have been ever involved in my growth as a researcher and as a person. It has been a pleasure getting to know and work alongside you.

Additionally, thank you to Dr. Kenith Meissner and his lab, particularly Dr. Sarah Ritter, Dr. Sandra Bustamante, and Dr. Yil-Hwan You. As my first introduction to the Texas A&M program, you provided the warmest of welcomes and invaluable guidance during my first year.

And finally, to my dad, who I wished could have seen the culmination of my work. Even though you are not here to read this, you have been with me each step of the way and have pushed me to better myself each day. Thank you for your love and support.

CONTRIBUTORS AND FUNDING SOURCES

Contributors

This work was supervised by a dissertation committee consisting of Professor Akhilesh Gaharwar (advisor) and Professors Melissa Grunlan and Roland Kaunas of the Department of Biomedical Engineering and Professor Ashlee Watts of the Department of Veterinary Medicine.

The RNA-seq data compiled within Chapter 1 was partially analyzed by Dr. Irtisha Singh at Cornell University. Much of the chemical characterization of molybdenum disulfide in Chapter's 3 and 4 were completed by Dr. Manish Jaiswal in the Gaharwar Lab. Lastly, bioink characterization of methacrylated kappa-Carrageenan was completed by Alexandra Bock under the supervision of the graduate student in the Gaharwar Lab.

All other work conducted for the dissertation was completed by the student independently.

Funding Sources

This work was made possible in part by National Science Foundation (CBET 1705852), the National Institute of Health (DP2 EB026265, R03 EB023454), and the Sigma Xi Grants-in-aid-of-Research Award. Its contents are solely the responsibility of the authors and do not necessarily represent the official views of the NIH, NSF, or Sigma Xi.

NOMENCLATURE

kCA	kappa-Carrageenan
MκCA	Methacrylated kappa-Carrageenan
4-PEG-SH	4-arm Poly (ethylene glycol) thiol terminated
MoS_2	Molybdenum Disulfide
nSi/Laponite	Laponite XLG
UV	Ultra-violet
GF	Growth factor(s)
2D	Two-dimensional
TGF-β	Transforming growth factor-beta
RNA-seq	Ribonucleic acid-sequencing
NMR	Nuclear magnetic resonance spectroscopy
G’	Storage modulus (Pa)
G”	Loss modulus (Pa)

TABLE OF CONTENTS

Page

LIST OF FIGURES

1. INTRODUCTION[*]

1.1 Introduction to Nanomaterial-Cell Interactions within Biomedical Engineering

Nanotechnology is advancing at a lightning pace, resulting in the emergence of novel nanomaterials with custom properties. Undoubtedly, tissue engineering can greatly benefit from this advancement. Throughout this compilation of work, I will focus on nanomaterials that possess at least one physical dimension in 1-100nm range. This feature allows more functionality and manipulation at a small scale. Nanomaterials are not a simple miniaturization of macroscopic counterparts; instead, they exhibit distinctive physical, chemical, optical, and mechanical properties, with an incredibly high specific surface area.[1-6] Their unique properties offer great application opportunities as well as challenges in scientific disciplines, ranging from nanoelectronic devices to advanced therapeutic modalities for presently incurable diseases.[5, 7-10] The applications of nanomaterials in biomedical research emanate from their scale: they operate on the same size scale as the majority of intimate biological moieties. Owing to their small size, nanomaterials can widely interact with the physiological environment and enable the development of systems that mimic complex hierarchical structures of extracellular matrices (ECM) and native tissues. In particular, the ECM is a dynamic structure of different nanofibers (such as collagen, actin filaments, etc.), nanocrystals, nanopores, and signaling molecules.[3, 8, 11-13] Also, a cell itself is essentially a multifunctional particle comprised of nano-compartments such cell membrane,

---

[*] Reprinted with permission from "Carrow, J.K.; Gaharwar, A.K. Bioinspired Polymeric Nanocomposites for Regenerative Medicine. *Macromolecular Chemistry and Physics* 2014." Copyright 2014 John Wiley & Sons, Inc. Reprinted with permission from "Kerativitayanan, P.; Carrow, J.K.; Gaharwar, A. K. Nanomaterials-Stem Cell Interactions: Emerging Trends and Potential Applications in Regenerative Medicine. *Advanced Healthcare Materials* 2015." Copyright 2015 John Wiley & Sons, Inc.

surface proteins, cytoskeletons, and nuclear membrane containing DNA.[13] It is recognized that cells in nature are surrounded by nanostructures, either when they interact with ECM, neighboring cells, or soluble factors.[12-14] Thus, as nanomaterials are small enough to interact and alter cellular level functions, they are expected to provide a new framework for medical intervention to diagnose.

Over the past few years, several nanomaterials have been developed and showed potential in biomedical applications including biosensors, imaging, drug delivery system, cellular therapies, stem cell modulation, and scaffolds for tissue regeneration.[7-9, 11, 13-17] For example, ceramic nanoparticles such as synthetic silicates induce osteogenic differentiation of adult stem cells without using any growth factors.[18] In another study, a nanobioconjugate particle of Polycefin^{TM}, an anticancer drug with polymalic acid (PMLA), is shown to specifically bind and attack breast cancer cells while stimulating an immune response against the tumor. Unlike other conventional anti-cancer drug delivery systems, the nanoconjugate was uptaken by cancer cells and thus have higher efficacy. These novel properties were due to the unique nanostructure of the conjugate.[19]

While *in vitro* success can be achieved, directing cell behavior with engineered nanomaterials in a clinical setting is a complicated task. Part of the challenge stems from a high degree of variability between cell donors and cell types. This plays directly into the clinical translatability of these materials as patients will experience various degrees of therapeutic success. Another issue is that of dosage and duration of exposure. Persistence of nanomaterials increases accumulation of potentially cytotoxic degradative products within the cell; therefore, clearance from the local cell environment is necessary to ensure cell viability. This directly contradicts with the ability of nanomaterials to persist in the local environment to induce changes in cell phenotype. Therefore, researchers must find a balance regarding the timing of interactions to maximize bioactivity while avoiding cytotoxicity.

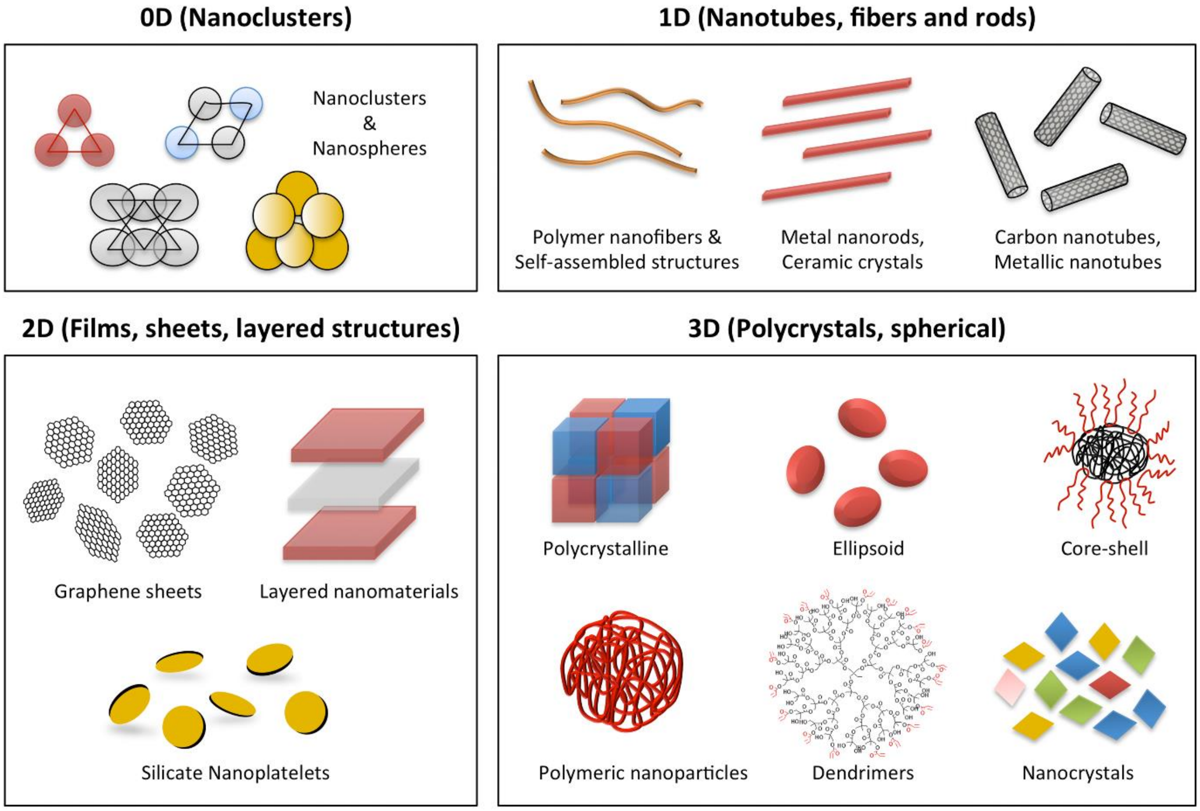

Figure 1-1. Illustrated are the various dimensions (0D, 1D, 2D, 3D) and corresponding materials available for implementation within polymeric nanocomposite designs. Each dimension targets explicit cellular pathways through mimicking physical or chemical cellular environments and consequently offers a multitude of tools for investigators to better control material-cell interactions. Reprinted with permission from Carrow et al., 2014.

From the perspective of the material itself, physical and chemical properties play a vital role in dictating interactions with cells. Uptake into the cell can be limited by size of nanoparticles while shape can improve uptake kinetics through improved membrane energy conformations.[20-22] Along this line, most of the nanomaterials can be divided into four different categories: zero, one, two, and three-dimensional nanomaterials (**Figure 1-1**). Zero-dimensional (0D) nanomaterials are atomic clusters mostly composed of metallic elements. One-dimensional (1D) nanomaterials include use of metal nanorods, nanotubes, ceramic crystals, polymer nanofibers, and self-assembled structures. Most of the two-dimensional nanomaterials have included layered structures such as graphene, synthetic clays, and double layered hydroxides (LDH). Three-dimensional (3D) nanomaterials include polycrystals and spherical particles. Structural anisotropy, or higher aspect ratios of applied particles, increases binding to the cellular membrane, thereby increasing the likelihood of uptake by the cell.[23-24] These improved binding characteristics with cells, as well as polymer chains, provides an additional benefit from using 2D materials. Beyond nanomaterials, however, choice of stem cell source and type are additional parameters for researchers.

Stem cells can be classified into two types: embryonic stem cells (ESCs), obtained from inner cell mass of the blastocyst, and adult stem cells (ASCs), found in postnatal tissues such as umbilical cord, bone marrow, and adipose and neuron tissues.[4, 25-27] Embryonic stem cells (ESCs) are an ideal cell source for regenerative medicine due to their indefinite self-renewal and pluripotency. However, there are some ethical controversies concerning the destruction of embryos to obtain ESCs. Multipotent adult stem cells (ASCs) are the alternative with fewer ethical issues, but they have limited differentiation and self-renewal capacity.[25, 28] Thus, researchers have attempted to reprogram somatic cells into pluripotent stem cells by somatic cell nuclear transfer (SCNT), and inducing the expression of embryonic transcription factors to generate induced pluripotent stem cells (iPSCs). Still, the reprogramming efficiency and the epigenetic abnormalities of the cells differentiated from SCNT and iPSCs are debating.[29-31] With the convergence of nanomaterials and stem cells, the restoration and regeneration of diseased cells and tissues are becoming a clinical possibility.

However, before the therapeutic applications of stem cells can be introduced to clinics, several challenges need to be resolved, specifically controlling the self-renewal processes, proliferation, and regulating the differentiation.[4, 26-27] As discussed, nanomaterials have the ability to control stem cell behavior due to their small-size and biomimetic characteristics. It has been shown that chemical composition, surface topography, mechanical properties, electrical, and morphological properties of nanomaterials significantly affect stem cell responses.[4, 14, 16, 26-28, 32-34] For example, Sjöström *et al.* reported that the height of pillar-like nanostructures on a titanium scaffold greatly influenced mesenchymal stem cells behaviors. Specifically, the stem cells on the 15 nm high pillars well spread with large focal adhesion whereas those on the 100 nm high pillars formed small focal adhesion with poorly defined cytoskeletons.[35] In addition, silver nanoparticles were found to be cytotoxic to stem cells and could cause mitochondria and DNA damages in a dose-dependent manner.[36-37] Furthermore, while a range of multifunctional nanomaterials for tissue engineering applications have been developed and investigated over the past few years, the interactions between nanomaterials and stem cells are not quite understood (**Figure 1-2**). Because of the current deficiencies from the perspective of holistic cell behavior, there is a need to design studies that will more completely uncover these interactions.

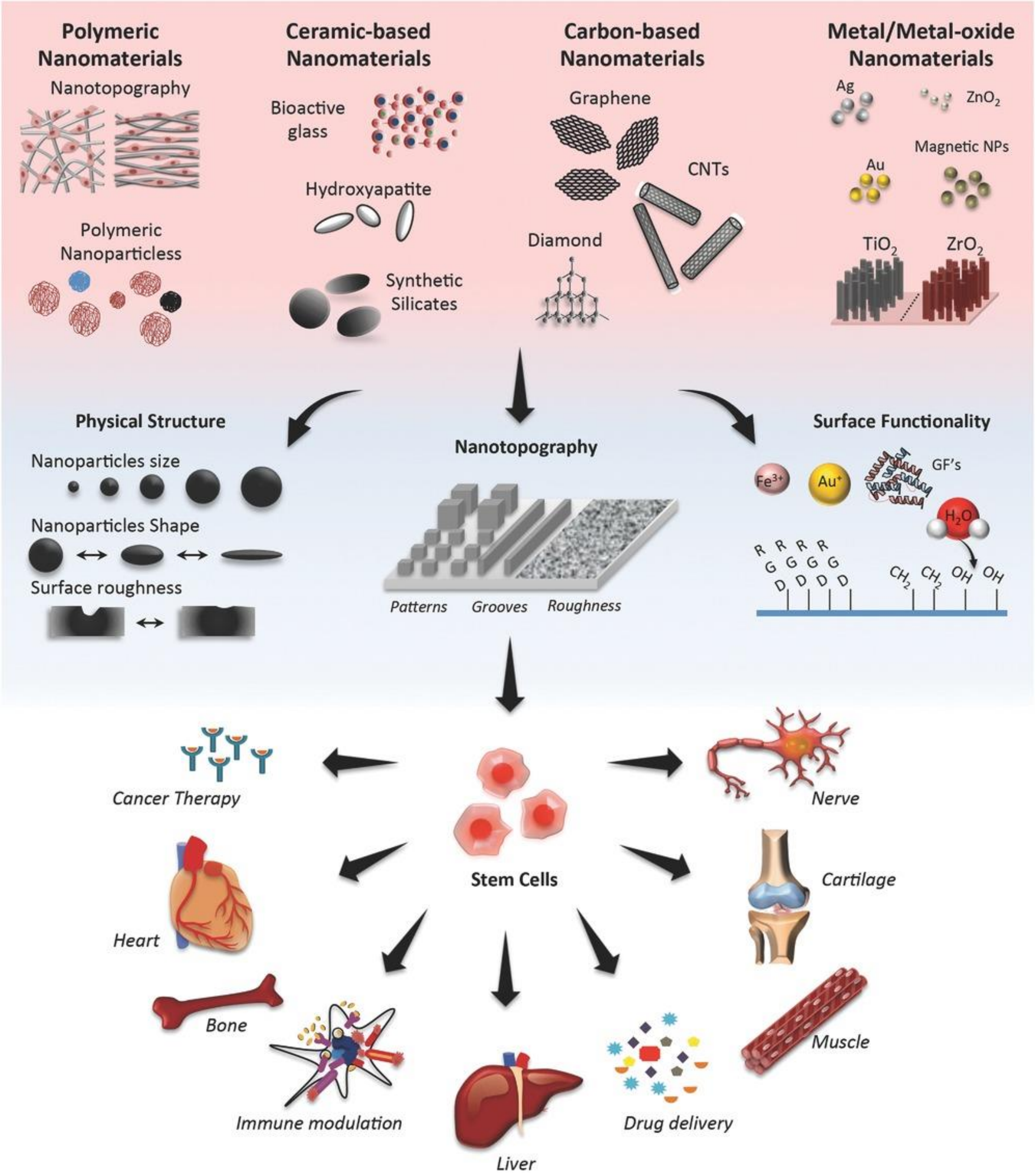

Figure 1-2. Nanoparticle interactions with stem cells comprise interplay of multiple mechanisms, including physical, chemical, or surface interactions. Physical interactions are dependent on size, shape, and stiffness of the nanoparticles, whereas chemical interactions include the presence of ions, growth factors or hydrophilic moieties. Surface interactions revolve around surface patterning, like nanopillar spacing or size and surface roughness. Similarly, chemical modification to the nanomaterial surface via introduction of cell binding sites. The combined effects of these various interactions contribute to the differentiation capabilities of the nanomaterial and can lead to a variety of tissues including but not limited to cardiac, bone, hepatic, muscle, cartilage, and nerve tissues. Some of the emerging applications of nanomaterials include immune modulation and smart drug delivery devices. Reprinted with permission from Carrow et al., 2014.

1.2 Nanomaterials-Stem Cells in Regenerative Engineering

Engineering implantable alternatives for auto- or allografts to replace or restore tissue or organ functions requires that cells organize into tissues with physiological and morphological features resembling those in the body.[3, 32] Several tissue engineering techniques involving nanomaterials have been developed and shown to have tremendous potential (**Figure 1-3**). Nanomaterials have been subsequently designed to provide inductive cues within the microenvironment that mimic the stem cell niche, aiming to direct stem cell differentiation in a controllable manner. Along these lines, research literature has reported success in using nanomaterial-based scaffolds to regulate stem cell differentiation into various types of tissue, including bone, cartilage, and neurons, for instance.[3, 15, 17, 32, 38] Since extracellular matrices (ECM) provide crucial information regulate cell behavior and tissue formation, one approach is to develop scaffolds with nanoscale features mimicking ECM of the engineered tissues.[3, 17] For example, cardiac ECM is composed of a nanoscale interweaving pattern of elastin and collagen fibrils that form a dense network with ECM molecules. This structure forces cardiomyocytes to couple mechanically to one another, forming elongated bundles of anisotropic syncytium.[39] Mimicking the nature, nanogrooved surfaces were found to promote cardiomyocyte differentiation and alignment.[40] In addition, nanomaterials can be designed to mimic structures of natural tissues. For example, bone is a nanocomposite of collagen fibrils and hydroxyapatite nanocrystals. Many studies have shown that nanocomposites of biodegradable polymers and hydroxyapatite could induce differentiation of stem cells to osteoblasts.[3, 32]

Besides a biomimetic microenvironment, controlled release of biomolecules/morphogens, such as growth factors and cytokines, is another key factor for stem cell differentiation and tissue growth.

Incorporation of nanoparticulate delivery systems with high specific surface area into scaffolds was proved to effectively support tissue morphogenesis, viability, and functionality.[3, 17, 41]

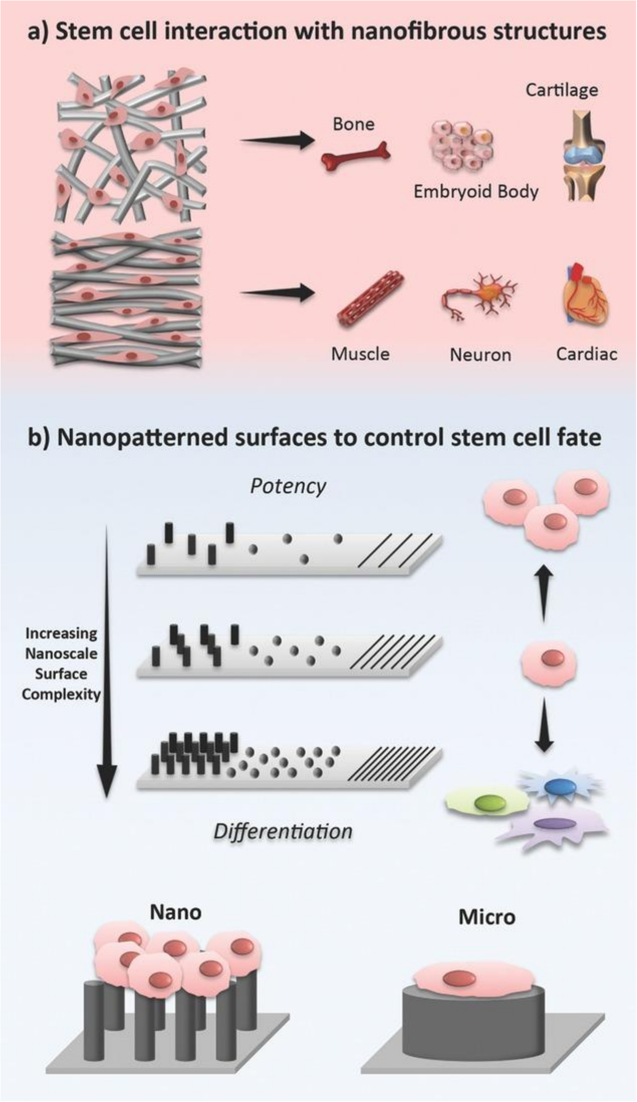

Figure 1-3. Various nanotopographical modifications alter cell behavior and therefore stem cell outcomes. a) Random nanofibers promote embryoid body, bone, and cartilage formation, while aligned nanofibers show enhanced neuronal induction with directed neurite extension as well as cardiac and myogenic induction. b) Surfaces with increasing nano-complexity and roughness via nanopillars, nanodots, or nanogrooves induce differentiation while smoother surfaces are preferential for potency maintenance. Nanopillars augmented cell adhesion and growth versus micropillars while also forming large cell aggregates, while micropillars induced greater cell spreading. Reprinted with permission from Carrow et al., 2014.

Examples of these nanoscale systems include polymeric nanospheres, nanotubes, nanowires, liposomes, and dendrimers.[42] With different nanomaterial designs, we are able to control release of each agent either temporally or by changing the spatial environment through temperature, pH, mechanical stress, and light.[17]

Applications of nanomaterials in regenerative medicine have made drastic progress in the last decade. The advancements in nanotechnology and stem cell research have offered new solutions to many challenging problems of traditional medicine as well as stem cell-based therapy.[4, 6, 9, 14, 16, 28, 43] Quantum dots, fluorescent carbon nanotubes, and magnetic nanoparticles, for instance, have been used for labeling stem cells, permitting a noninvasive monitoring after transplantation, and for drug and gene delivery into stem cells.[4, 9, 16, 43-51] Amongst these applications, engineered nanomaterials have been extensively investigated to regulate the differentiation of stem cells for tissue engineering. One such two-dimensional (2D) nanomaterial that has shown great promise in the field of stem cell induction using synthetic materials is that of nanoclays/nanosilicates, like Laponite XLG. This material has a unique charge distribution with a negative surface charge over both faces and a positive charge around the edge. This enables enhanced interactions with a variety of biomolecules that can dictate future cell behavior.

Specifically, 2D nanoclays have been recently demonstrated to be osteoinductive. Previous studies by Gaharwar *et al.* showed that Laponite nanosilicates (nSi) ($Na^{+}_{0.7}[(Mg_{5.5}Li_{0.3})Si_{8}O_{20}(OH)_{4}]^{-}_{0.7}$) nanoclay could induce osteogenic differentiation of MSCs in an absence of osteoinductive factors such as dexamethasone and BMP-2. This was mainly attributed to their dissolution products: Na^+, Mg^{2+}, $Si(OH)^4$, and Li^+. In particular, Mg^{2+} is known to play an important role in integrin-dependent cell adhesion. Orthosilicic acid ($Si(OH)_4$) upregulates bone-related gene expressions and promotes collagen I synthesis, and Li^+ activates Wnt-responsive genes via regulating Runx-2 transcription factor. Furthermore, the addition of nSi had negligible effects on metabolic activity of MSCs up to a concentration of 1mg/ml. Half maximum inhibitory concentration (IC_{50}), the concentration of nSi at which metabolic activity of MSCs was reduced to 50%, was found to be 4 mg/ml. Compared to nanohydroxyapatite (nHA) and silica nanoparticles with similar size, nSi show cytotoxicity at ten-fold higher concentration, indicating relatively high cytocompatibility.[18] The success demonstrated in these studies push future investigations to uncover methods to localize these bioactive synthetic materials within a 3D cell-laden construct, like those found within the field of tissue or regenerative engineering.

1.3 Polymeric Nanocomposites for Functional Regeneration

The traditional paradigm of tissue engineering includes three integral components: cells, growth factors, and scaffolds, which produce a favorable regenerative response. With the increase in our understanding of the extracellular microenvironment (ECM) and its role in developmental biology, our approaches to material synthesis and scaffold design are continuously evolving. Success of many constructs is often limited by the lack of biological complexity generated, leading to researchers investigating new methods to emulate native tissue environments. Oftentimes, inspirations for scaffold architecture or utilized biomaterials stem from structures preexisting in nature, considering millions of years have resulted in the emergence of highly sophisticated and efficient materials.[52-54] For example, shark skin and lotus leaves have been investigated for inspired surface design due to the anisotropic flow characteristics and superhydrophobic properties of each respectively.[55] Both of these naturally occurring “engineered” arrangements illustrate the nano- and microscale components, leading to macroscale function.

Biology offers the best models for strategies to rationally design high-performance biomaterials with similar properties of natural materials, such as bone, cartilage, nacre, or silk.[56-59] To translate our fundamental understanding of nature into products that are useful in a clinical setting, the chemical, physical, and biological properties of newly developed bio-nanomaterials need to be optimized to support, regulate, and influence long-term cellular activities. Both bottom-up and top-down approaches are considered by materials scientists to design biomimetic components for tissue engineering.[53-55, 60-61] At each level (i.e. nano, micro, macro), mechanisms underlying cellular interactions will vary, leading to a variety of requirements for consideration that will be implemented cohesively during material design. Akin to nature, biomaterial design processes strike a balance between complexity and unification of the individual components. The design and fabrication of bioinspired nanomaterials for tissue engineering applications requires a fundamental understanding of the interactions between polymers, nanostructures, and cells. Most of the biomimetic polymeric nanocomposites consist of two or more types of polymers or polymers combined with different nanomaterials to obtain composite structures with desired properties (**Figure 1-4**). A range of structures including interpenetrating, fibrous scaffolds, and nanocomposite biomaterials that mimics structural and physical properties of extracellular matrix is engineered. The biomimetic materials are used for range of biomedical applications including regenerative medicine, wound dressing, drug delivery, gene therapy, and immune engineering.

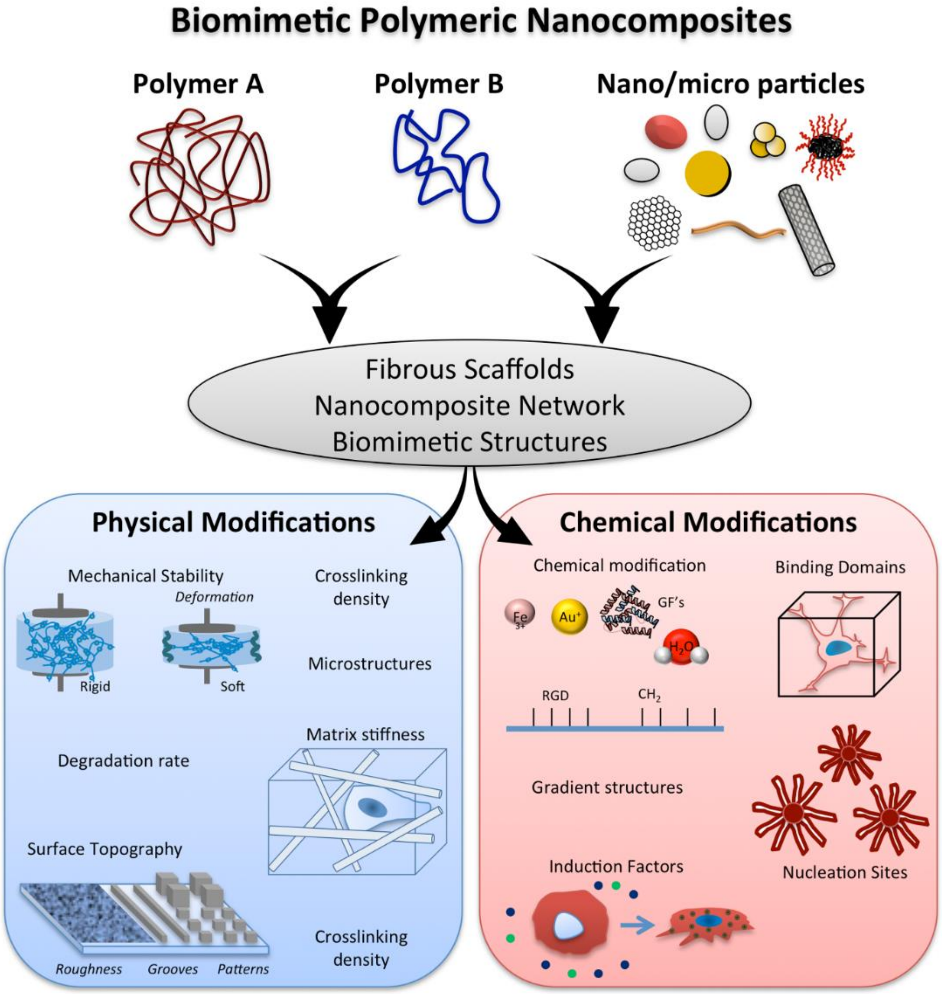

Figure 1-4. To improve scaffold outcomes, bioinspired composite materials can provide additional benefits toward cellular proliferation and induction through a variety of materials and can take multiple forms upon fabrication. Basic materials include multipolymer systems or the introduction of nano/microparticles into a polymeric network. Two main components from this inspiration are physical and chemical modifications of the base polymers present within the scaffold. The integration of various materials can result in enhanced mechanical stability through additional crosslinking sites, ECM mimesis, or interactions between the cell membrane and material surface. Additionally, these same materials enable spatially controlled protein binding for cellular adhesion, nucleation of mineralized matrix, or provide vital factors for the motivation of stem cells toward specific lineages. Reprinted with permission from Carrow et al., 2014.

1.3.1 Traditional Tissue Engineering Constructs

In order to design biomimetic nanomaterials for the repair of native tissues, we need to consider and compare the structures and properties of the natural tissue, along with the biological influence of cells on the synthetic biomaterial properties. For example, bone comprises a hierarchical structure that provides the tissue with its advantageous mechanical and functional properties, yet also significantly hampers replication in an *in vitro* setting.[62] Therefore, to recapitulate native complexity, bioactive materials can motivate specific cellular activity in a spatially confined manner. Among popular fillers, nanoceramics, such as synthetic silicates, nHA, and bioactive glass, instill tissue engineering scaffolds with a supplementary influence over stem cell behavior. While the underlying mechanisms of their bioactivity are still under evaluation, evidence points to the combination of degradation products, surface interactions with cellular membranes, and charge. Novel microscale technologies have emerged in order to fabricate polymeric-based structures with additional nanofillers, thus providing investigators with an architecture or material inspired from nature.[60]

Integrated composites not only establish additional sources of bioactive factors, they can also fortify the polymer network via physical or chemical interactions.[52, 63-66] While many naturally-based polymers demonstrate useful cytocompatibility or synthetics enabling extensive tailorability to the polymer chain, often a purely polymeric system lacks the necessary mechanical strength or degradation characteristic *in vivo*, particularly for load-bearing regenerative applications. Most extensively investigated natural polymers for biomedical applications include collagen, gelatin, starch, cellulose, alginate, chitosan, and fibrin, while synthetic polymers include use of poly(ethylene glycol) (PEG), polyvinyl alcohol (PVA), poly(caprolactone) (PCL), poly(lactic-co-glycolic acid) (PLGA), and poly(glycerol sebacate) (PGS). To overcome the limitations of a basic polymeric scaffold, additional nanomaterials are integrated into the architecture to form a nanocomposite with combinatorial benefits of each biomaterial, including bioactivity, adhesiveness, environmental-sensitivity, and mechanical improvements.[67] These modifications can employ bioinspiration via mimesis of naturally occurring molecular processes or microenvironment induction of cellular behavior (**Figure 1-4**). Through reversible physical interactions (e.g. electrostatic, dipole, hydrogen-bonding) or chemical crosslinks (e.g. thiol-based, radical polymerization), superior distribution of stresses imparted onto a polymeric composite scaffold can be achieved. Similarly, degradation profiles of networked polymer composites can be extended to allow sufficient cell migration and tissue formation *in vivo*.

Similar to considerations for direct exposure between nanomaterials and stem cells, physical attributes play a role in nanocomposite outcomes. Due to differences in surface to volume ratio, these nanomaterials interact with polymers via substantially different mechanisms and result in unique property combinations compared to their micro- and nano- counter parts. Dimensionality of incorporated nanomaterials will stimulate specific cellular pathways via multiple channels, providing investigators with a host of tools for controlling cell behavior. Thus the type of biomaterials used to make a composite structure play a major role in determining the end application of these structures.

Polymeric nanocomposites take a variety of forms for regenerative medicine applications, each with associated tradeoffs resulting from varying fabrication methods and materials. Persistent efforts to improve cellular and subsequently tissue outcomes have encouraged creative approaches toward material design. The methods by which nanomaterials are introduced to polymeric matrices are not only dependent on these fabrication strategies but also desired biological response. For example, internalization of many inorganic nanomaterials can alter differentiation status of encapsulated stem cells; however, these same materials present in the extracellular environment can act as nucleation sites for deposition of mineralized matrix, effectively mimicking those found on collagen fibrils in bone tissue.[68-69] While multiple groups have integrated both polymer and additive prior to scaffold polymerization, some have investigated the effects of creating nucleation sites after polymer network formation through incubation with simulated body fluid (SBF) in the presence of carboxyl-groups on the polymer chain.[70-73]

Another promising application is the integration of nanostructures into microfabricated 3D scaffolds to compensate for matrix limitations.[3, 17] For example, one of the main challenges in neural tissue engineering is the loss of conduction within cell-seeded constructs. Incorporation of carbon nanotubes into the scaffolds resulted in increased signal transmission of neurons.[3, 74] Also, growing nanotitanate wires perpendicular to the pore walls of 3D microstructures was shown to increase cell viability by enhancing hydrophilicity and cell-matrix interactions.[75] Souza *et al.* (2010) reported another approach to guide cell assembly into a 3D structure with desired geometry using magnetic nanoparticles. In this study, hydrogels composed of bacteriophage, iron oxide, and gold nanoparticles, were uptaken by stem cells. Subsequent magnetic levitation and spatial control of magnetic field during cell proliferation allowed the engineering of complex tissues composed of several cell types in specific locations.[76] Notwithstanding the achievements, understanding stem cell-nanomaterial interactions behind these phenomena will create a plenty of room for improvement.

Due to preliminary studies previously described indicating bioactivity of 2D nanosilicates, multiple studies have incorporated these materials into polymer matrices to improve regeneration of localized cells. Gaharwar *et al.* fabricated cross-linked silicate-PEO nanocomposites and showed high silicate concentration (60% and 70%) significantly enhanced attachment, proliferation, and osteogenic differentiation of hMSCs. This was mainly attributed to high protein adsorption on silicates. Also, silicate nanoparticles may serve as focal adhesion sites for the cells. On the other hand, nanocomposites with low silicate concentration (40% and 50%), where non-cell adhesive PEO chains dominated, cells growth was limited.[77]

In addition, Wang *et al.* incorporated nSi to electrospun PLGA nanofibers. It was found that more serum proteins were adsorbed on PLGA/nSi than on pure PLGA nanofibers. This could be a consequence of a slight increase in hydrophilicity and an expansion of nanofibers upon nSi addition, making them more favorable for protein adsorption. As a result, cell adhesion and proliferation were enhanced.[78] Agreeing with the studies by Gaharwar *et al.*[18], PLGA/nSi nanofibers induced osteogenic differentiation of MSCs in growth medium without any inductive factors. Similarly, Gaharwar *et al.* reported that an addition of nanoclays to electrospun poly(Ɛ-caprolactone) (PCL) induced osteogenic differentiation. They support adhesion and proliferation of hMSCs. Also, osteogenic differentiation increased with increasing nanoclay content from 0.1% to 10%, as evidenced by enhanced ALP activity and matrix mineralization. Since protein adsorption was comparable amongst samples, it was postulated that enhanced differentiation was mainly attributed to increased surface roughness with increasing nanoclay content. It has been shown that cells preferably anchor and stretch their filopodia on micro-scale rough surface, leading to enhanced metabolic activity. [79] While these studies begin to highlight the push towards nanomaterial integration within 3D polymeric structures, particularly for nanosilicates, there are application-specific compositions that have yet to be developed.

1.3.2 Bioprinting Within Tissue Engineering

Engineering artificial tissues offers great promise for treating patients with organ failures that are associated with disease, injury and degeneration. Current approaches to engineer 3D tissue structures are based on encapsulating cells within a porous scaffold and providing structural and molecular clues to facilitate formation of tissue structure.[80] These scaffolds serve as synthetic ECM that assist in cellular organization into a 3D architecture by providing appropriate chemical and physical stimuli for facilitate their growth and maturation.[81] The tissue engineering techniques have been applied to generate a range of tissues including cartilage and skin, as these tissues can survive without presence of extensive vascularization. However, engineering tissues with complex structure such as heart, and liver, is not possible until numerous challenges regarding their development are addressed. These challenges include our inability to generate a functional vasculature that can supply the tissue with nutrients and oxygen and the inability to mimic the complex cell-microenvironment interactions that regulate the formation of functional tissue. The ability to recapitulate the structural and architectural complexity of many of these tissues and interfaces (*e.g.* between bone and cartilage) necessitate the development of a capable fabrication technique at the macro and micro scale.

Bioprinting is a process of precisely designed scaffolds using 3D printing technologies for functional organ engineering. Due to the pressing need for functional organ engineering, precisely designed scaffolds for tissue repair and organ replacement are needed. The emergence of nano- and microscale printing technologies, resulted in development of 3D printed scaffolds consist of spatially-controlled cell patterns that may be loaded with appropriate biological moieties to control or direct cell fate.[82-85] The rationale for such significant control over spatially-driven design is to better coordinate cellular arrangements into tissues and organs of interest and therefore lead to the successful production of functional and implantable constructs. While challenges exist to maintain the intended shape and cell distribution of the construct over time, researchers have employed a variety of novel methods and technologies, such as modified 3D printing techniques, multi-nozzle printers, and chemical modifications to bioinks for printability and biological stimulation, to improve upon the bioprinting process.[86-89]

Recently, bioprinting technique has shown promising in mimicking tissue complexity by controlling cell-matrix, cell-cell interactions.[60, 90-94] This bottom-up approach uses layer-by-layer printing of cell-laden polymeric bioinks. The very essence of bioprinting emanates from bioinspiration as materials are meticulously printed to mimic cellular arrangement in the body. The merging of synthetic and natural polymer bioprinting systems can more aptly control material properties, and these hybrid polymer designs strive to incorporate the benefits of both types of polymers, for example, the tunability of synthetic materials with the biomimetic characteristics of natural polymers. Due to the inherent complexity of native tissues, both types may be justified for functional regeneration. Tissue engineers utilize copolymeric systems to avoid the shortcomings of single polymer type systems. While synthetics demonstrate acceptable mechanical strength and fair biocompatibility, they lack cell-recognizable binding sites to improve adhesion or migration; however, hybridization with natural polymers can better mimic the ECM, leading to superior cellular outcomes.[95] Development of hybrid systems that apply synthetic polymers as scaffolding for structure and shape with the cell-laden naturally-based bioink as filler closely follows the work of those group integrating electrospun mats into hydrogel networks. This method benefits from including synthetic thermoplastic polymers due to improved mechanical strength that typical hydrogel materials cannot provide,[96-97] and this system permits numerous bioinks laden with multiple cell types, either differentiated or potent cells, for printing in a single construct.[96] It was possible to print lower viscosity hydrogels due to the mechanical strength provided by the thermoplastic materials, typically PCL or PLA, enabling researchers to print with a greater amount of bioink materials. Another benefit arises from XYZ-controlled nozzles printing these thermoplastic polymers, with similar spatial resolution as applied hydrogels, enabling additional control over the final structure or through electrospinning, layers of randomly aligned PCL fibers can separate sections of hydrogels, which could allow variation of printed cell type and hydrogel material at different layers.

While bioprinting has only recently demonstrated its true impact as an exciting field of regenerative medicine research, recent trends attempting to propel these technologies into areas of even greater clinical relevance have surfaced. To overcome the shortcomings of a purely polymeric system (e.g. insufficient mechanical strength, inefficient cellular stimulation, etc.), nanocomposites have been introduced to improve upon these lacking characteristics for those same factors expressed for 2D and 3D scaffolds.[52, 98-99] Through force distribution and greater variation of chemical groups among multiple materials, multi-nozzle printing systems can also enhance mechanical integrity as well as inductivity. These two aspects are crucial for bioprinting design to more suitably mimic the native ECM. One group chemically functionalized 3D printed PLA with multi-walled carbon nanotubes (MWCNTs), induces stem cell differentiation into both osteogenic and chondrogenic lineages.[100] Polymer-nanocomposite interfaces boosted mechanical strength of the modified scaffold, with a Young's Modulus similar to that of subchondral bone (30-50 MPa), therefore providing stem cells with a desirable substrate as well as limiting possible stress shielding effects.[100] By subjecting MWCNTs with poly-L-lysine after H_2 treatment, hydrophilicity of the MWCNTs increased and consequently biocompatibility of the construct. From successful biomimesis, the scaffold increased stem cell proliferation. One could imagine in future work if cells were encapsulated in a hydrogel bioink and printed layer-by-layer simultaneously with the functionalized PLA-MWCNT scaffold, tissue formation could be further improved. Similarly, dispersal of nano-titania in a printed poly(lactic-co-glycolic acid) (PLGA) scaffold established surface roughness comparable to native bone, comparable to nHAp electrospun scaffolds.[99] Osteoblast adhesion and tensile modulus increased in well-dispersed scaffolds resulting from topographical modifications to PLGA fibers as well as physical crosslinking between the polymer and nanofiller. Lastly, these nanoparticles shield the scaffold from the acidic degradation products of PLGA during hydrolysis, reducing autocatalysis effects and thus extending mechanical stability for longer periods of time. Again, printing a polymer hydrogel bioink concurrently with the nanocomposite 3D scaffold could provide the correct microenvironment for tissue formation *in vivo*.

In this dissertation, the interactions between stem cells and two different bioactive nanomaterials in tissue engineering will be examined. From a material property perspective, varied chemical and physical characteristics will play a prominent role in dictating cell behavior. Specifically, we will evaluate two different types of two-dimensional nanomaterials including ceramic nanosilicates and transition metal dichalcogenides and their interactions with stem cells, focusing exclusively on tissue engineering applications. Lastly, the formation of 3D nanocomposite hydrogels with each of these materials will be explored as potential scaffolds to achieve regeneration.

2. WHOLE-TRANSCRIPTOME ANALYSIS OF 2D NANOSILICATE TREATED STEM CELLS[*]

2.1 Introduction

2D nanomaterials have gained unprecedented attention due to their unique atomically thin, layered, and well-defined structure that provides distinctive physical and chemical properties compared to bulk 3D counterparts.[101-105] As the dimensions of 2D nanomaterials are only a few nanometers thick, they interact with biological moieties in a unique way and have raised exciting questions about their interactions with cellular components. In addition, different physical (*e.g.* size, shape, and charge) and chemical characteristics of 2D nanoparticles have a multitude of effects on cells including toxicity, bioactivity, or therapeutic capabilities, which are not well understood.[106-107]

Understanding cellular responses following treatment with 2D nanomaterials will aid in evaluating their application for biomedical and biotechnology applications.[106] Some of these 2D nanomaterials are investigated for tissue engineering and therapeutic delivery.[104-105] Currently, the impact of nanoparticles on cellular machinery are evaluated by quantifying targeted gene families involved in signaling pathways, while neglecting those outside the scope of the study.[108-112] Uncovering molecular targets and affected signaling pathways at the whole transcriptome level provides a holistic view of nanomaterial interactions with the cellular machinery. High throughput sequencing of transcripts (RNA-seq) is a powerful tool for an accurate quantification of expressed

---

[*] Reprinted with permission from “Carrow, J.K.; Cross, L.M.; Reese, R.W.; Jaiswal, M.K.; Gregory, G.A.; Kaunas, R.; Singh, I.; Gaharwar, A. K. Widespread changes in transcriptome profile of human mesenchymal stem cells induced by two-dimensional nanosilicates. *PNAS* 04/24/2018.” Copyright 2018 National Academy of Sciences.

transcripts that largely overcomes limitations and biases of microarrays.[113-116] This high throughput technique will not only give an unbiased global view of the cellular activity but will also provide pivotal insights about the affected cellular pathways.

Synthetic 2D nanoclays have been recently investigated for regenerative medicine, due to their biocompatible characteristics, high surface-to-volume ratio, and uniform shape compared to other types of 2D nanomaterials.[105, 117-119] Synthetic clays such as nanosilicates ($Na^+_{0.7}[(Mg_{5.5}Li_{0.3}Si_8O_{20}(OH)_4]^-_{0.7}$, Laponite XLG®) have a disc-shaped morphology and exhibit a dual charged surface.[120-122] Nanosilicates dissociate into nontoxic products (Na^+, Mg^{2+}, $Si(OH)_4$, Li^+) in physiological conditions and show cytotoxicity only at ten-fold higher concentrations (LD_{50}~4 mg/mL)[123-124] compared to other 2D nanomaterials such as graphene (LD_{50}~100 μg/mL)[125]. These 2D nanosilicates are investigated for a range of biomedical applications including, tissue engineering, drug and therapeutic delivery, and bioprinting.[126-133] While these studies have generated encouraging results for 2D nanosilicates, their interactions affecting the transcriptome profiles remain unknown.

Here, we investigate the interactions of 2D nanosilicates with hMSCs to uncover key triggered biophysical and biochemical cellular pathways by examining transcriptome dynamics. We observed widespread changes in gene expression profile (> 4,000 genes) following nanosilicate exposure, which has not been reported previously. Our study further probes surface-mediated kinase signaling triggered by 2D nanosilicates. In addition, transcriptomic dynamics of nanosilicate treated-hMSCs identifies key genes and enriched gene ontology (GO) pathways and categories related to stem cell differentiation, specifically towards osteochondral lineages, which has not been previously reported. We validated the RNA-seq findings using *in vitro* studies which support the ability of nanosilicates to direct hMSC differentiation towards bone and cartilage lineages. This enables further development of nanomaterials-based therapeutics for regenerative medicine. More generally, transcriptomic analysis by next-generation sequencing provides a comprehensive and objective snapshot of cellular behavior following nanomaterial exposure/attachment. Furthermore, this study demonstrates the utility of next generation sequencing for the study of cellular interactions on nanoengineered substrates, and the key role of this approach is likely to play in this rapidly expanding field of regenerative medicine.

2.2 Materials and Methods

2.2.1 Nanosilicate Characterization: Synthetic clay nanosilicates (Laponite XLG®, $Na^+_{0.7}[(Mg_{5.5}Li_{0.3}Si_8O_{20}(OH)_4]^-_{0.7})$, were obtained from BYK Additives (Gonzales, TX). Authentication was performed by determining chemical composites, crystal structure, size and shape of nanosilicates. Specifically, inductively coupled plasma mass spectrometry (ICP-MS, Elemental Analysis (PerkinElmer NexION 300D) and X-ray photoelectron spectroscopy (XPS, Omicron XPS system with Argus detector) were used to determine chemical composition of nanosilicates. For ICP-MS, nanosilicates was dissolved in 0.5% hydrogen peroxide solution for 24 hours. ICP-MS analysis was performed to determine the concentrations of Si, Li, and Mg. Dried nanosilicates were used for XPS analysis, where binding energies for magnesium (Mg *2s*, *2p*), sodium (Na *1s*), oxygen (O *1s*), lithium (Li *1s*), and silicon (Si *2p*) were determined. The raw values were deconvoluted *via* Lorentzian function using GraphPad Prism. X-ray diffraction (XRD, Bruker D8 Advanced) was used to determine crystalline structure of nanosilicates. XRD was performed with a copper source on both powdered nanosilicates and exfoliated nanosilicates (in water) that were then flash-frozen in liquid nitrogen and lyophilized. Atomic force microscopy (AFM, Bruker Dimension Icon Nanoscope) and transmission electron microscopy (TEM) were performed to determine the size and shape of the nanosilicates. For both AFM and TEM, a dilute solution of exfoliated nanosilicates was placed on silicon substrate or carbon grid. For AFM, nanosilicate thickness was observed via tapping mode and the data was analysis using Nanoscope Analysis software. For TEM, an accelerating voltage of 200 kV using a JEOL-JEM 2010 (Japan) was used to determine the morphology of nanosilicates. The zeta potential and hydrodynamic size of nanosilicate-FBS solutions were measured with a Zetasizer Nano ZS (Malvern Instrument, U.K.) furnished with a He−Ne laser at 25°C. Filtered particles were achieved through utilization of a 0.2 µm filter.

2.2.2 In vitro Studies – Cytocompatibility, Cell uptake, and Retention: Human mesenchymal stem cells (hMSCs) were acquired from the Texas A&M Institute for Regenerative Medicine (College Station, TX, USA) previously isolated and subsequently expanded from voluntary donors under an institutionally approved tissue recovery protocol. hMSCs were cultured under normal media conditions consisting of α-minimal essential media (alpha-MEM, Hyclone, GE Sciences) with 16.5% fetal bovine serum (Atlanta Biologicals, USA) and 1% penicillin/streptomycin (100 U/100 µg/mL, Gibco). After every 2-3 days, half of culture media was exchanged for fresh media. Cells were passaged with 0.5% trypsin-EDTA upon reaching confluency of ~70% and seeded at ~2500 cells/cm^2. All experiments were completed with cell populations under P5. Metabolic activity was monitored via MTT (ATCC) and Alamar Blue (Thermo Scientific) assays, per manufacture protocols. The BD Accuri C6 Flow Cytometer and a propidium iodide (PI, 40 µg/mL) stain with

RNase (100 μg/mL) were used to perform cell cycle analysis following earlier protocol.[134] Prior to seeding, hMSCs were serum starved (only 1% FBS in media) for 24 hours to synchronize cell populations and then treated with nanosilicates. After 48 hours of exposure, cells treated with various concentrations of nanosilicates were trypsinized and fixed in ice cold 70% ethanol. Formed cell pellets were washed in PBS, followed by incubation in a PI staining solution at 37 °C for 30 minutes. Cells were stored at 4°C until flow cytometer analysis. For endocytosis inhibition analysis by flow cytometry, cells were cultured under normal conditions in 6-well plates. Cells were washed three times with PBS and then treated with inhibitors of clathrin-mediated, calveolar-mediated, or macropinocytosis (35 μM chlorpromazine hydrochloride, 10 μM nystatin or 400 nM wortmannin, respectively) (Sigma–Aldrich) at 37 ˚C for 30 minutes. After this pretreatment, silicate nanoparticles fluorescently tagged with Rhodamine B were added to the culture (final concentration 100 μg/ml) and incubated for a further 60 minutes. Subsequently, the cells were washed with PBS, trypsinized, and then suspended in cell culture medium. Particle uptake was then analyzed via flow cytometry. Hyperspectral images and data were captured using an Olympus research grade optical microscope equipped with CytoViva (Auburn, AL) patented enhanced darkfield illumination optics and full spectrum aluminum halogen source illumination. The system was also equipped with the CytoViva hyperspectral imaging system, producing spectral image files from 400nm-1,000nm at 2nm spectral resolution. CytoViva's customized version of ENVI hyperspectral image analysis software was used to quantify the sample's spectral response and conduct any spectral mapping of the sample elements.

For evaluation of reactive oxygen species (ROS) production, the BD Accuri C6 Flow Cytometer was used. hMSCs were cultured in a 12 well-plate to ~70% confluency then treated with an ERK inhibitor (PD184352, 5 µM) for 2 hours at 37 °C. Cells were then incubated with dihydroethidium (DHE, 25 µM) for 10 minutes 37 °C. Then, cells were washed with PBS and treated with 50 µg/mL nanosilicates in phenol-red free and serum free media for 2 hours at 37 °C. After 2 hours, cells were washed with PBS, trypsinized, spun down, and then re-suspended in PBS for flow cytometer analysis.

For lysosomal staining and actin staining, hMSCs were cultured in a 12-well plate to ~70% confluency. hMSCs were treated with 1 µL of CellLight® Lysosomes-GFP and incubated overnight at 37 °C for lysosomal staining. Then, hMSCs were treated with rhodamine-labelled nanosilicates for 3 hours at 37 °C and later fixed with 2.5% glutaraldehyde. Similarly, for actin staining, hMSCs were treated with nanosilicates for 24 hours, then fixed with 2.5% glutaraldehyde and permeabilized with 0.1% TritonX-100. Phalloidin stain was then added and samples were incubated for 1 hour at 37 °C. The stain was removed, washed with 1X PBS, and then samples were treated with propidium iodide/RNAase for 30 minutes at 37 °C. Both lysosomal stained and actin stained samples were imaged via a confocal microscope (Nikon). Further tracking of nanosilicates and lysosomal activity was done using the BD Accuri C6 Flow Cytometer. hMSCs were treated with rhodamine-labelled nanosilicates for 1, 3, and 7 days and then treated with CellLight® Lysosome-GFP overnight. Cells were then washed with PBS, trypsinized, spun down, and resuspended in PBS for analysis.

For investigating nanosilicate dissociation within hMSC culture, inductively coupled plasma mass spectrometry (ICP-MS, Elemental Analysis (PerkinElmer NexION 300D)) was performed. hMSCs were cultured with nanosilicates for 1, 3, and 7 days and then cells were washed with PBS, trypsinized, spun down and then resuspended in deionized water. After re-centrifugation, the pellet was digested in a 1% nitric acid, 0.5% hydrogen peroxide solution for ICP-MS analysis in which the concentrations of Si, Li, and Mg were determined. This digestion protocol was modified from earlier study.[135]

2.2.3 Whole-transcriptome sequencing and analysis: For RNA-seq analysis, cells were cultured until 65% confluent and were subjected to two different media compositions for one week. One subset of cells maintained normal media conditions as a negative control (2 replicates); another group was treated with nanosilicates (50 µg/mL) for 48 hours (2 replicates), after which the media was replaced with normal media for the remaining five days. Excess nanosilicates were removed as they are expected to be cleared within 48 hours. Upon completion of the week, cells were washed with PBS and pelleted. RNA was isolated and collected via a Roche, High Purity RNA Isolation kit following the manufacturer's protocol. Initial quality of nucleic material (~1.5-2.0 µg) was evaluated using spectrometer absorbance ratios between 280/260 nm around 2.0. Samples were analyzed via a high-output HiSeq platform with TruSeqRNA sample preparation and single-end read length of 125 bases (Genomics and Bioinformatics Service, Texas A&M AgriLife Research, Dr. Charlie Johnson). The sequenced reads were trimmed and aligned to the human genome (hg19) using a RNA-seq aligner, STAR.[136] For the control group, 21,563,695 (uniquely mapped 20,153,164) and 24,531,989 (uniquely mapped 22,900,448) sequenced reads successfully aligned to the genome for the two replicates. Similarly, 22,266,394 (uniquely mapped 20,623,575) and 15,769,384 (uniquely mapped 14,633,793) reads aligned to the genome for the nanosilicate treated group for both the replicates. For further analysis, only uniquely mapping reads were utilized. Expression of a gene was determined by counting the number of uniquely mapped reads overlapping the coding exons normalized by gene length. Genes >1 RPKM (reads per kilobase million) were considered to be expressed in any condition if they were expressed in both the replicates. Genes expressed in at least one of the condition were then tested for differential expression. Generalized linear models (GLM) were used to identify the differentially expressed genes where the expression counts were modelled as negative binomial distribution.[137] The bioconductor DESeq package was used for this purpose. All other analyses were done in statistical software R. The GO enrichment analysis was done using GOStats bioconductor package. REVIGO[138] was used to refine the extensive list of significant CC GO-terms. It reduces the functional redundancies and clusters the terms based on semantic similarity measures. Visualization of gene networks was accomplished through Cytoscape[139] and GeneMANIA[140] and ClueGO[141] by direct comparisons to a *Homo sapiens* reference genome. DAVID Bioinformatics Resources were also utilized for genetic network analysis.[142] Only genes with a p adjusted-value (false discovery rate) less than 0.05 were included within the network and subsequent GO term network formation.

2.2.4 RNA-seq Validation Using qRT-PCT and Western Blot: For quantitative Reverse Transcription polymerase chain reaction (qRT-PCR), cells were cultured under similar conditions as RNA-seq. Following RNA isolation, cDNA was synthesized from 1 µg of RNA for each sample via SuperScript III Reverse Transcriptase (Thermo Fisher, United States) following manufacturer's protocol. SYBR Green reagent was then used for amplification quantification. Expression and fold change values were calculated from fluorescence using the program DART-PCR.[143] For Western Blot analysis, cells were cultured under similar conditions as qRT-PCR and RNA-seq. Protein samples were isolated via a Laemmli Buffer (4% SDS, 20% glycerol, 10% 2-mercaptoethanol, 100 mM Tris HCl, and 0.2% bromophenol blue). Gel electrophoresis

(Invitrogen, Mini Gel Tank) was performed on protein samples and subsequent gels were transferred (Invitrogen, iBlot 2) to a nitrocellulose membrane according to manufacture protocol. The membranes were blocked with 5% BSA in PBST (PBS + 0.1% Tween 20) for 30 minutes then western processed (Invitrogen, iBind). β-actin, COMP, p-MEK1/2, and COL1A1 primary antibodies and HRP conjugated secondary antibodies were purchased from Boster Bio and incubation was performed per manufacture protocols. Blots were developed (SuperSignalTM West Pico PLUS Chemiluminescent Substrate, ThermoFisher) and imaged via LI-COR® 3600 C-Digit Blot Scanner. Protein bands were quantified with LI-COR software. The blots were then restored and re-blocked with 5% BSA in PBST for further protein analysis.

2.2.5 In vitro Functional Study: For osteogenic differentiation samples were fixed with 2.5% glutaraldehyde at 14 and 21 days and stained for alkaline phosphatase (1-Step NBT (nitro-blue tetrazolium chloride)/BCIP (5-bromo-4-chloro-3'-indolyphosphate p-toluidine salt) substrate solution, ThermoFisher Scientific) and mineralization (Alizarin Red S stain, Electron Microscopy Sciences), respectively. Alizarin Red was quantified via acetic acid extraction and subsequent colorimetric detection.[144] For chondrogenic differentiation, samples were fixed with 2.5% glutaraldehyde at various time points, washed with PBS, 1% acetic acid, and then quickly stained with 0.1% Safranin O for 5 minutes. Samples were washed again with PBS twice and then imaged. For immunostaining, fixed cells were incubated with a 1% BSA in PBST (PBS + 0.1% Tween 20) for 30 minutes to block nonspecific binding. Cells were then incubated with a mouse anti-human aggrecan primary antibody (Abcam, MA, USA) within a 1% BSA solution overnight at 4°C. The primary antibody was then removed and cells were washed with PBS multiple times. Subsequently, cells were incubated for 1 hour at room temperature with a goat anti-mouse IgG with conjugated Alexa Fluor® 647 (Abcam, MA, USA) in a 1% BSA solution. The secondary antibody was then decanted and cells were washed multiple times with PBS. Samples were stored in PBS in the dark at 4°C until imaging.

2.3 Results and Discussion

2.3.1 Biophysical and Biochemical Characterization of Nanosilicates.

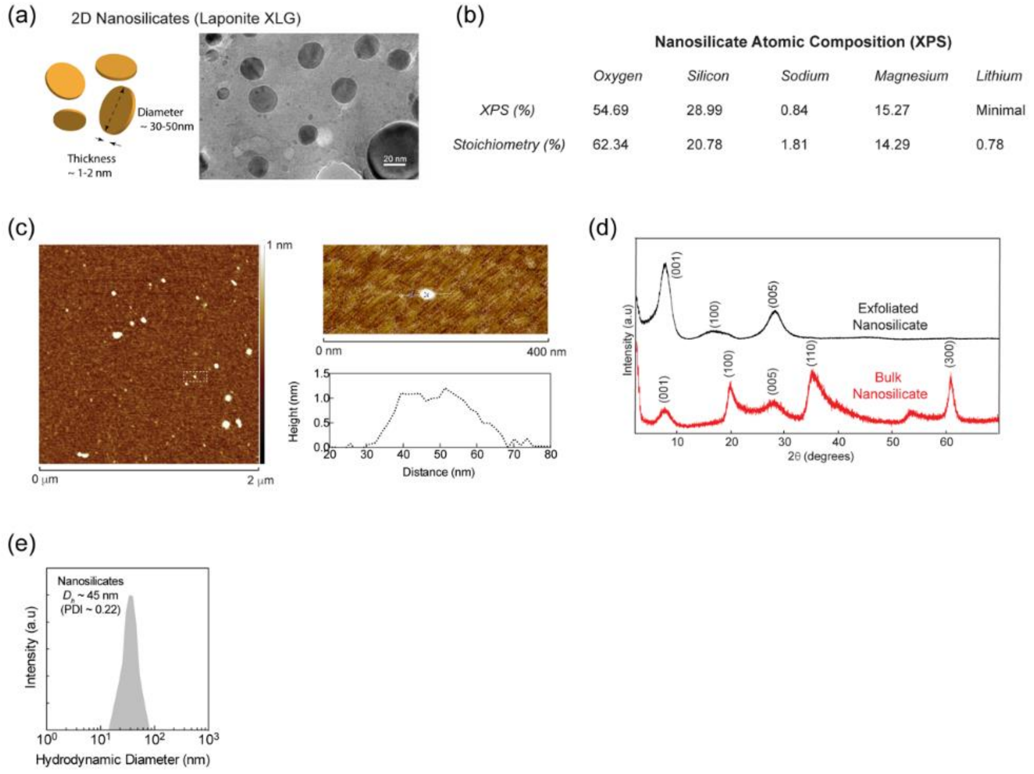

Figure 2-1. Material characterization of nanosilicates. Physical characterization of nanosilicates was completed to evaluate particles prior to introducing to hMSCs. (a) TEM of nanosilicates demonstrated disc morphology and nanoscale size. (b) XPS analysis revealed an elemental composition similar to that of the idealized stoichiometric ratio found within a unit cell of the nanosilicates. (c) AFM corroborated the nanoscale diameter (25-50 nm) and thickness (1-1.5 nm) of the nanosilicates. (d) XRD of both bulk and exfoliated (flash frozen with subsequent lyophilization) nanosilicates generated peaks at diffraction planes (001), (100), and (005) for both, with (110) and (300) present in the bulk sample. (e) DLS measurements quantified variability of nanosilicate hydrodynamic size in particles and displayed a narrow range of diameters (PDI – 0.22) around 45 nm. Reprinted with permission from Carrow, Cross et al., 2018.

Chemical and structural characteristics of 2D nanomaterials will dictate their interactions with cells.[107] A range of material characterization techniques were used to establish the chemical composition, crystalline nature, shape, and size of nanomaterials.[145] Transmission electron microscopy (TEM) showed that nanosilicates were 20-50 nm in diameter (**Figure 2-1a**). X-ray photoelectron spectroscopy (XPS) revealed the presence of oxygen (54.68%), silicon (28.99%), magnesium (15.27%), sodium (0.84%), and lithium (trace), which is similar to expected stoichiometry ($Na^{+}_{0.7}[(Mg_{5.5}Li_{0.3}Si_{8}O_{20}(OH)_{4}]^{-}_{0.7}$). The thickness of nanosilicates was determined to be around 1-2 nm using atomic force microscopy (AFM). The crystalline structure of nanosilicates was corroborated by observing characteristics diffraction plan (001), (100), (005), (110), (200), and (300) using x-ray diffraction (XRD). After exfoliation, a decrease in 2θ (20.1° to 16.8°) for diffraction plane (100), indicates an increase in *d*-spacing between nanosilicates, which is similar to previously reported studies.[122, 146] In biological media, such as blood plasma, cerebrospinal fluid or even culture media, the surface of nanoparticles become coated with various biomolecules forming a protein this initiates cellular internalization of nanoparticles *via* receptor-mediated endocytosis (**Figure 2-2a**). The binding of proteins from media to the nanosilicate surface was evaluated by monitoring hydrodynamic diameter (D_H) and zeta potential (ζ). After mixing of nanosilicates with media (containing fetal bovine serum), zeta potential of the nanoparticles shifted from -40 mV to -25 mV, indicating that the negatively charged surface of the nanosilicates were coated with biomolecules. Similarly, an increase in hydrodynamic diameter was

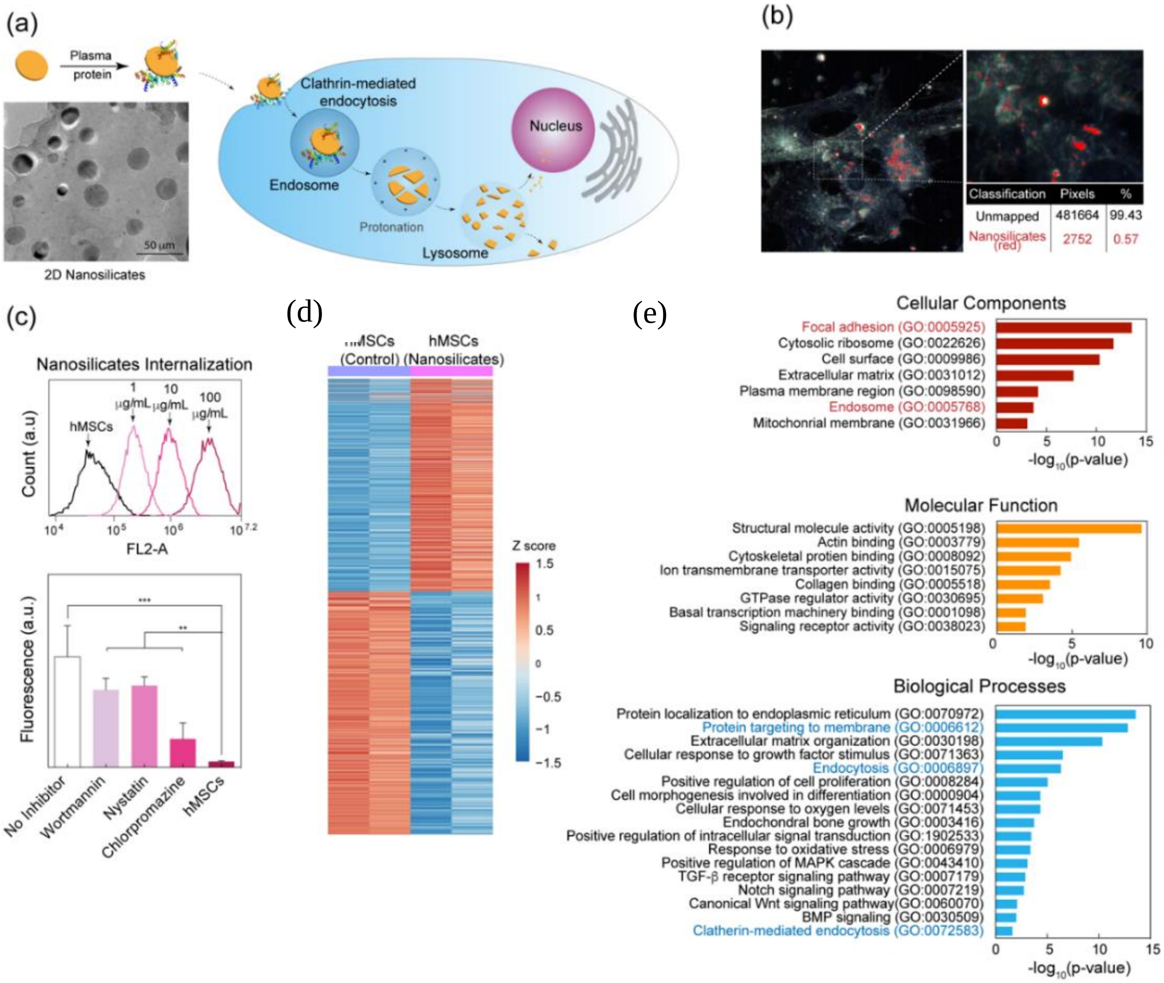

Classification	Pixels	%
Unmapped	481664	99.43
Nanosilicates (red)	2752	0.57

Figure 2-2. Biophysical interaction of nanosilicates and hMSCs. (a) Two-dimensional nanosilicates electrostatically bind to proteins from biological fluids and are subsequently internalized by cells via surface-mediated endocytosis. (b) Hyperspectral imaging indicating distribution of nanosilicates throughout the cell body following endocytosis. The image was captured from transverse section of cell body. (c) Flow cytometry analysis of rhodamine-tagged nanosilicates demonstrate dose-dependent cellular uptake. The nanosilicates were primarily internalized via clathrin-mediated process (chlorpromazine) as opposed to macropinocytosis (wortmannin) or caveolar mediated (nystatin). **$P < 0.01$; ***$P < 0.001$. (d) Significant GO terms of associated biological processes, cellular components, and molecular functions from differentially regulated genes ($P < 0.05$). Terms related to biological process and cellular components indicate strong biophysical interactions between cells and nanosilicates. (e) Clustering of significant 244 cellular component gene ontology (GO) terms into broader cellular component categories. Reprinted with permission from Carrow, Cross et al., 2018.

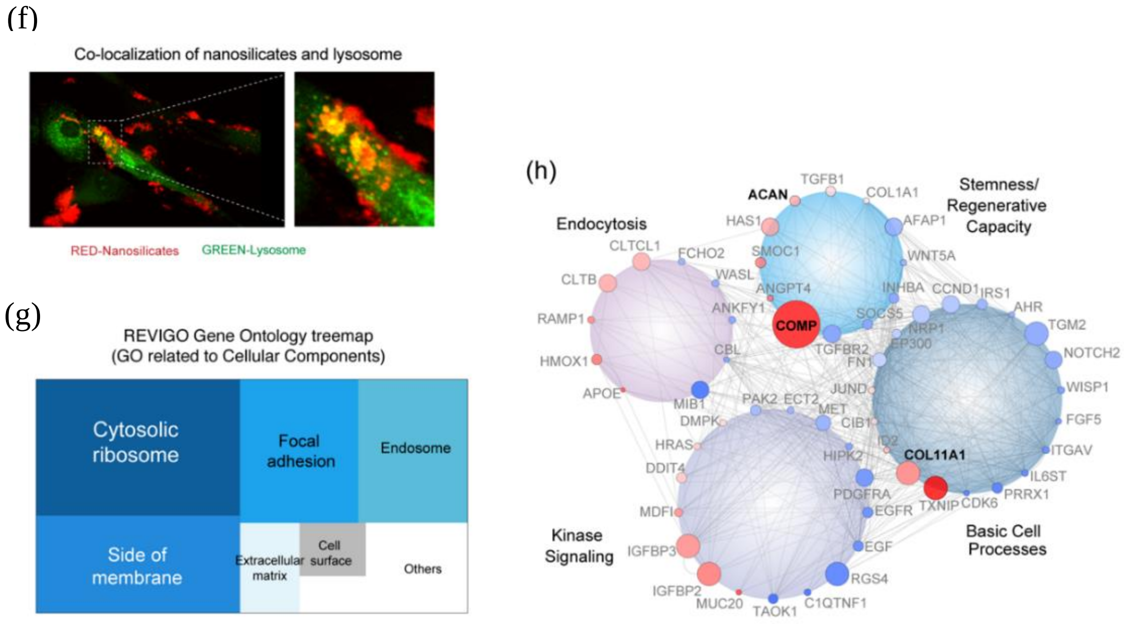

Figure 2-2 Continued. Biophysical interactions of nanosilicates and hMSCs. (f) LAMP1 staining (green) for lysosomal membranes further tracks nanosilicates (red) following endocytosis. (g) Row-scaled z-scores of quantile normalized gene expression [in log2(RPKM)] of >4,000 genes following treatment with nanosilicates (padjust < 0.05, red, up-regulated: 1,897 genes; blue, down-regulated: 2,171 genes). (h) Gene network displaying interconnected genetic targets after nanosilicate treatment with high degrees of expression and statistical significance (red, up-regulated; blue, down-regulated; size increases with significance). Reprinted with permission from Carrow, Cross et al., 2018.

observed from ~45 nm to ~90 nm after treatment with biological media. These results indicated corona. Oftentimes, that nanosilicate surfaces strongly interacted with biomolecules *via* electrostatic interactions to result in physical adsorption.

The effect of nanosilicates on cell health was evaluated by monitoring cytoskeletal organization, metabolic activity and cell cycle. An investigation into cell health *via* metabolic and viability assays (Alamar Blue and MTT) confirmed cytocompatibility of nanosilicates until the concentration of nanosilicates reached 100 μg/mL. In addition, hMSCs treated with nanosilicates showed similar cytoskeletal organization to untreated hMSCs. Cell cycle analysis also supported that the majority of cells were in G1 and G2 phases when treated with <100 µg/mL nanosilicates. These studies highlight that nanosilicates are highly cytocompatible.

2.3.2 Receptor-mediated Endocytosis of Nanosilicates.

The adsorbed proteins on the nanomaterial surface are predicted to influence cell-surface receptor mediated cellular uptake. We used hyperspectral imaging[147] to visualize internalized nanosilicates (**Figure 2-2b**), thereby allowing visualization of internalized nanosilicates without requiring chemical modifications that could have impacted uptake dynamics. Flow cytometry also demonstrated uptake of fluorescently-labeled nanosilicates in a concentration-dependent manner (**Figure 2-2c and 2-3a;** R^2=0.996).

The mechanism behind nanosilicate internalization was evaluated using chemical inhibitors to block specific endocytic pathways with a nanosilicate concentration of 50 µg/mL. We observed a significant decrease in cellular uptake of nanosilicates (79.5% reduction) when treated with a clathrin-inhibitor (chlorpromazine hydrochloride) (**Figure 2-2c**). Alternatively, other endocytic mechanisms such as caveolar-mediated (nystatin), and macropinocytosis (wortmannin) played a less prominent role in nanosilicate uptake. Furthermore, nanosilicate binding to the cell membrane and subsequent rapid internalization within 5 minutes (**Figure 2-3b**) is consistent with clathrin vesicle dynamics[148]. Co-localization of nanosilicates near or within lysosomal vesicles further confirmed nanosilicate localization (**Figure 2-2d**). These results indicated that nanosilicates are readily internalized by cells *via* clathrin-mediated endocytosis and transported to degradative cell machinery.

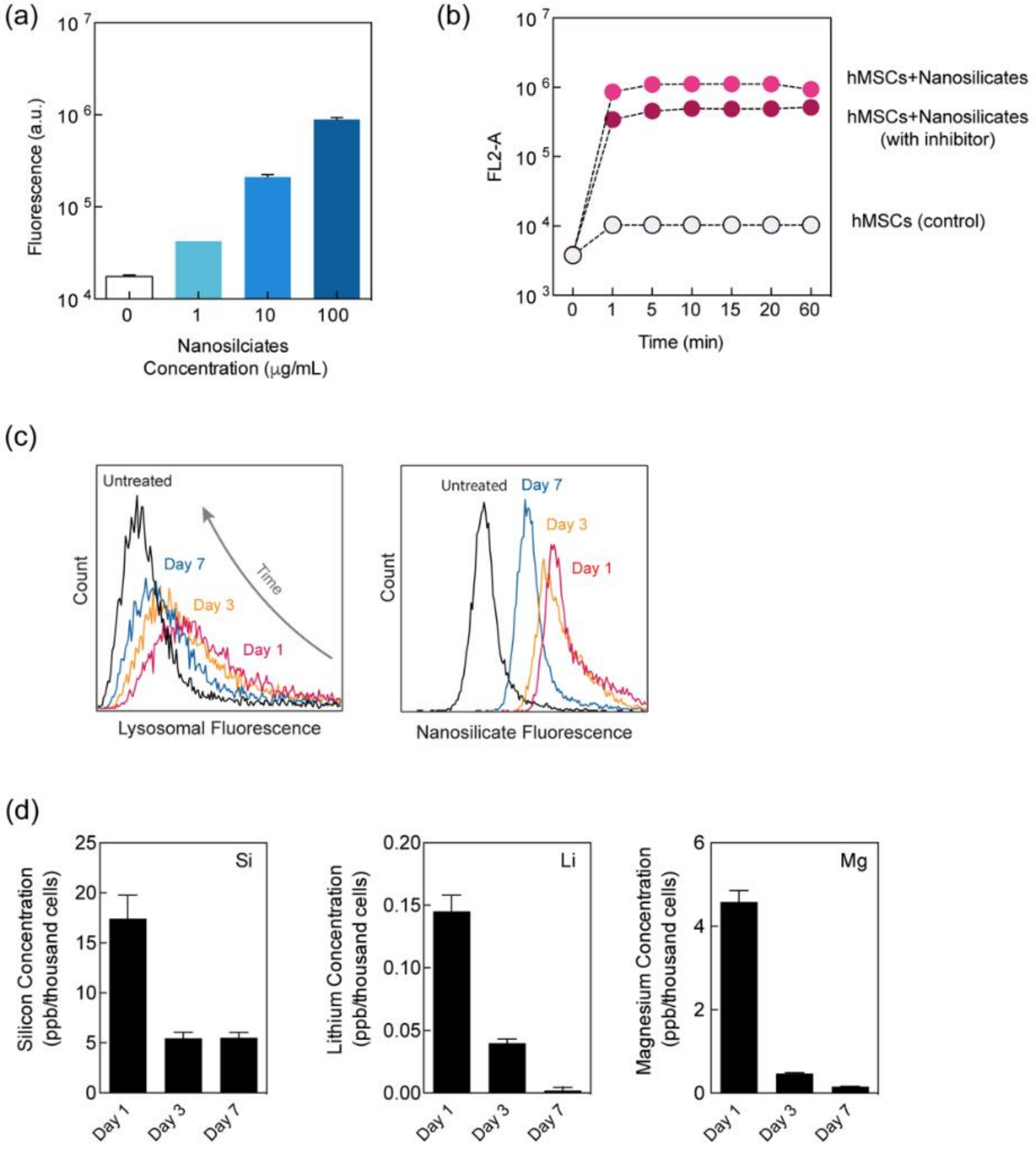

Figure 2-3. Silicate interactions with hMSCs were monitored using flow cytometry and ICP-MS. (a) Uptake of fluorescently-tagged nanosilicates displayed concentration dependent internalization. (b) Endocytosis of particles occurred rapidly with chemical inhibition of a clathrin-mediated process reducing uptake. (c) Following internalization, tagged-particles were trafficked to lysosomal bodies with an increase in these vesicles observed after 24 hours and returning to basal levels over the course of a week. (d) Introduction of nanosilicates to low pH environments of late endosome/lysosome vesicles initiated dissolution of the particles over a week. Ion products was greatest at 24 hours and decreased over time as nanosilicates continued to be trafficked in and out of the cell in addition to particle dissociation. Reprinted with permission from Carrow, Cross et al., 2018.

Following uptake, nanosilicates remained within the cell for more than 7 days and were not exocytosed or dissociated immediately. The retention of nanosilicates by cells was determined using flow cytometry. A steady decrease was observed over a course of 7 days in cells staining positive for nanosilicates i.e. day 1 (96.3 ± 4.8%), day 3 (69.0% ± 10.6%), and day 7 (32.8% ± 19.5%) (**Figure 2-3c**). To further confirm this, we monitored nanosilicate retention by cells over a week with ICP-MS (**Figure 2-3d**). The nanosilicate content was decreased by 31% on day 7, compared to day 1. Over the course of 7 days, cells also maintained an enhanced lysosomal vesicle response (**Figure 2-3c**). The stability of nanosilicates in physiological microenvironment was evaluated at pH 7.4 (mimicking cell body) and pH 5.5 (mimicking an intracellular compartment such as lysosome). A significantly higher release of minerals at pH 5.5 was observed compared to 7.4, indicating predicted *in vitro* dissociation of nanosilicates. After 7 days, release of silicon (~10%), magnesium (~6%) and lithium (~16%) was observed at pH 5.5. These results indicate that nanosilicates were retained by hMSCs and possibly dissociate within lysosomes over a course of 7 days.

Dissolution of nanosilicates inside cells can trigger biochemical signaling *via* release of minerals in the cytosol. Earlier studies have shown that mineral ions can significantly influence cell functions. For example, silicon ions have shown to direct stem cell differentiation by triggering cWnt signaling pathways[149] and are critical for cartilage development[150]. Likewise, magnesium ions have been shown to upregulate production of COL10A1 and VEGF in hMSCs[151]. Lithium, an inhibitor of glycogen synthetase kinase-3β (GSK-3β), activates Wnt-responsive genes by elevating cytoplasmic β-catenin.[152-153] These studies suggest that intracellular release of ionic dissolution products of nanosilicates (Si(OH)$^{+}_{4}$, Mg^{+}, Li$^{+}_{,}$) could stimulate hMSC differentiation.

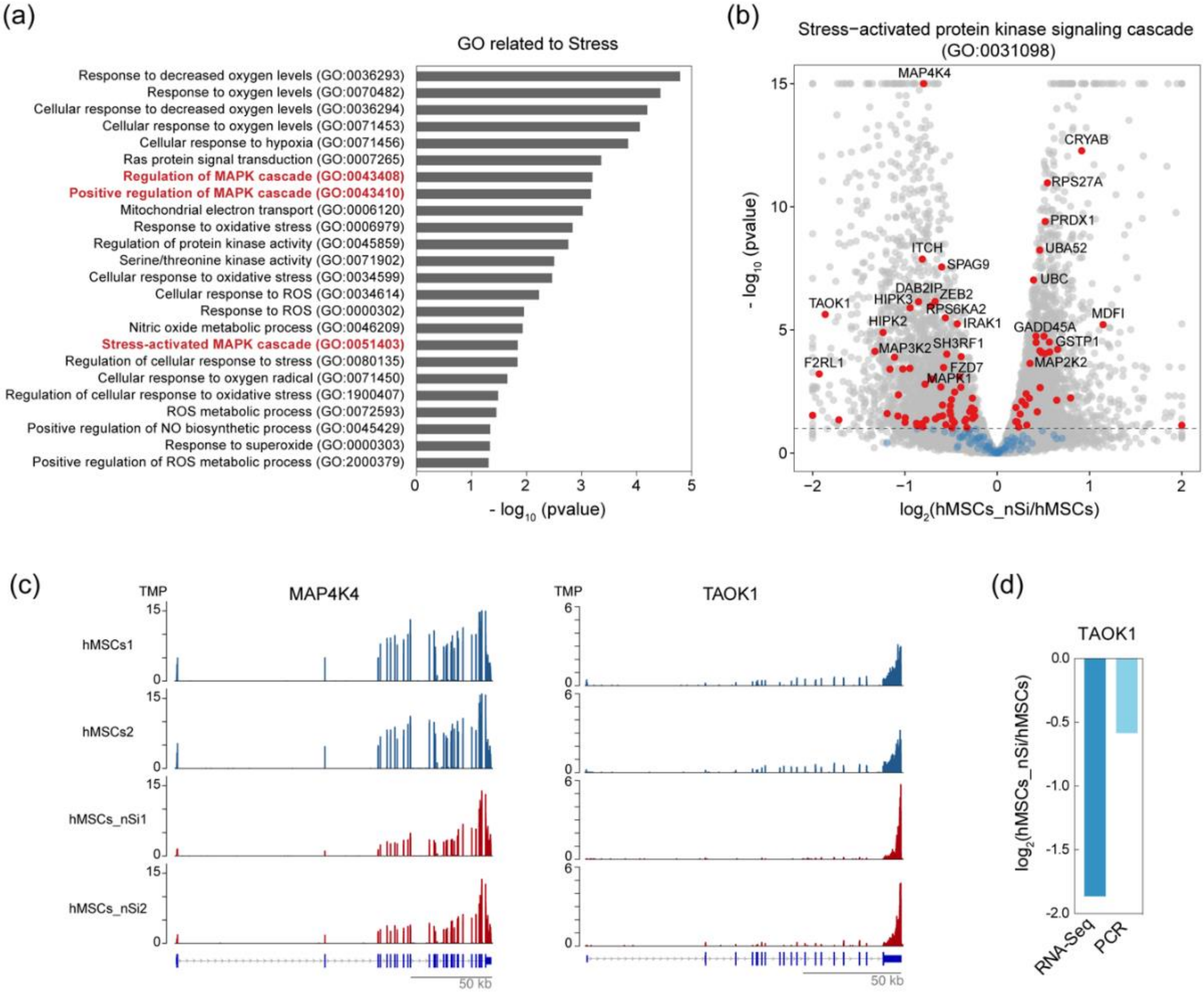

Figure 2-4. Nanosilicates lead to stress-induced MAPK signaling. (a) Nanosilicate treatment results in activation of stress-related response. A list of GO terms related to stress after nanosilicate treatment indicate signal propagation *via* MAPK/ERK signaling pathways. (b) The volcano plots evaluating DGE were generated for GO:0031098 and (c) gene expression profile of MAP4K4 and TAOK1 demonstrating stimulation of nanosilicate-induced MAPK/ERK signaling pathways. (d) Comparison of TAOK1 gene expression obtained from RNA-Seq was validated using qRT-PCR. Reprinted with permission from Carrow, Cross et al., 2018.

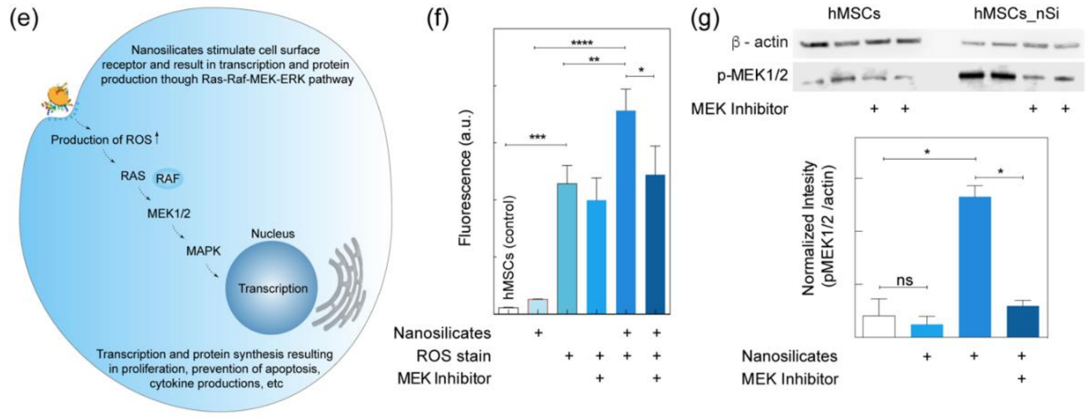

Figure 2-4 Continued. Stress induction of nanosilicate treated hMSCs. (e) Nanosilicates trigger a stress-responsive kinase cascade (Ras-Raf-MEK-ERK pathways), leading to changes in reactive oxygen species (ROS) production and subsequent RNA transcription and protein synthesis. (f) Flow cytometric analysis was performed to measure the stress-responsive kinase cascade, by measuring ROS production with a ROS-sensitive fluorescent reporter dye. Experiments were performed in the presence or absence of a MAPK inhibitor. A significant increase in ROS-mediated fluorescent signal is observed upon exposure to nanosilicate, and this is abrogated after treatment with the MAPK inhibitor. (g) Production of p-MEK1/2 was determined using western blot in presence of nanosilicates and MEK inhibitor, establish the role of nanosilicate in MAPK/ERK signaling. Reprinted with permission from Carrow, Cross et al., 2018.

2.3.3 Widespread Transcriptomic Changes Triggered by Nanosilicates.

Sequencing of expressed mRNAs by RNA-seq can be used to determine genome-wide changes in gene expression resulting from cellular response to external stimuli.[154] hMSCs (2500 cell/cm^2) were exposed to nanosilicates (50 μg/mL) and whole transcriptome sequencing (RNA-seq) was performed after 7 days (**see Methods**). The 7-day time point was chosen to provide a broad overview of cell processes, ranging from endocytosis and proliferation to early differentiation. Two replicates of untreated and treated hMSCs were sequenced. The sequenced reads were aligned to reference genome (*hg19*) using RNA-seq aligner. The replicates for both the conditions showed high concordance ($r=0.99$). The normalized gene expression levels were determined by calculating the reads per kilobase of transcript per million (RPKM). We used generalized linear models

(GLMs) to identify differentially expressed genes (DGE) between nanosilicate treated hMSCs and untreated hMSCs (**see Methods**). This comparison revealed significant changes in the expression level of 4,068 genes (**Figure 2-2e**), 1,897 up-regulated genes, 2,171 down-regulated genes, FDR-adjusted $p < 0.05$). Such wide-spread changes in gene expression profile have not been reported earlier. For example, human dermal fibroblast cells treated with gold nanoparticles were shown to differentially regulate 1439 genes[155], while another study demonstrated that human immune cells treated with graphene oxide experienced differential regulation of 1147 genes.[156] It is important to note that these previously reported studies were performed using microarrays[155-156] and the widespread effect of nanoparticles on whole-transcriptome was not investigated. Thus, our result strongly suggests that nanoparticle treatment leads to a widespread cellular response which is reflected by the change in transcriptome profile of hMSCs treated with nanosilicates, requiring further exploration into prominent cellular pathways.

The genes that change their expression due to nanosilicate treatment are part of various cellular pathways and biological processes. Thus, to identify the key biological processes and pathways that are affected when the cells interact with nanosilicates, we performed gene ontology (GO) enrichment analysis for the three GO categories (biological processes-BP, cellular components-CC, and molecular functions-MF). Nanosilicate treatment showed significant enrichment for 1,132 GO terms ($p < 0.05$), including 884 for BP, 134 for CC, and 114 for MF. We then narrowed down key GO terms based on high significance (*p-value*) in each category to highlight the widespread effect of nanosilicates on hMSCs (**Figure 2-2f**). The key GO terms significantly enriched in BP are endocytosis [GO:0006897], and endochondral bone growth [GO:0003416]. The analysis also indicated positive regulation of MAPK cascade [GO:0043410], transforming growth factor beta

(TGF-β) receptor signaling pathway [GO:0007179], notch signaling pathway [GO:0007219], canonical *Wingless* (cWnt) signaling pathway [GO:0060070], and bone morphogenic protein (BMP) signaling [GO:0030509]. GO analysis also supported our observation that nanosilicates are internalized *via* clathrin-mediated endocytosis [GO:0072583]. Overall, the GO enrichment analysis indicated that the predominant downstream effect of nanosilicates was on kinase activity, cell differentiation, and ECM reorganization.

Functional annotation clustering performed using DAVID[142], highlights the role of cell-membrane mediated signaling due to nanosilicate treatment. We then used REVIGO[138] to refine the extensive list of significant CC GO-terms by reducing functional redundancies and clustering the terms based on semantic similarity measures. GO for CC were enriched for cytosolic, ribosome, focal adhesion, and endosomal processes (**Figure 2-2g**). These results further suggested a sequence of events initiated at the cell membrane through protein localization to membrane [GO:0072657] and endocytic vesicle formation [GO:0006897, GO:0006898] accompanied by protein targeting to membrane [GO:0006612], and trafficking by lysosome [GO:0043202, GO:0005764]. Specifically, genes involved in clathrin-mediated endocytosis [GO:0072583] were significantly affected, corroborating the endocytosis inhibition studies. To validate the clathrin-mediated endocytosis, change in expression level of clathrin heavy chain like 1 (CLTCL1), an important gene that encodes a major protein of the polyhedral coat of coated pits and vesicles, was confirmed using quantitative reverse transcription polymerase chain reaction (qRT-PCR). We then clustered differentially expressed genes ($p<0.05$) using Cytoscape [139] into different cellular processes such as basic cell processes, kinase signaling, endocytosis and stemness/regenerative capacity (**see Methods**). Networks between genes from same pathways were generated to illustrate connected and interdependent genes regulated by nanosilicate treatment (**Figure 2-2h**). Overall, these results demonstrate that nanosilicates significantly affect the transcriptomic profile of hMSCs, which can translate to measurable changes in behavior.

2.3.4 Nanosilicates Activate Surface-mediated Signaling.

The high surface-to-volume ratio and dual charged surface of nanosilicates are expected to facilitate strong interactions with the cell membrane. The physical interactions between cells and nanoparticles are expected to stimulate a variety of intracellular signaling events including proliferation and differentiation.[107-108, 157] Of which, many are coupled with GTPase activity. Accordingly, a significant change in expression of upstream regulators of Ras (*e.g.* RalB, DDIT4, and HRAS) and Rho (*e.g.* DMPK, PAK2, ECT2) subfamilies of GTPases was observed upon nanosilicate treatment. These Ras and Rho genes are associated with peptidyl-serine phosphorylation [GO:0033135] and protein serine/threonine kinase activity [GO:0071900]. Both Ras and Rho GTPase subfamilies affect cell behaviors such as cytoskeletal arrangement, cell migration, and stem cell fate.[158-159] From analyzing enriched GO pathways related to stress, two prominent membrane-activated cascades emerged; the mitogen-activated protein kinase (MAPK) cascade and Janus kinase/signal transducers and activators of transcription (JAK/STAT) pathways (**Figure 2-4a**). Genetic markers specific to extracellular signal-regulated kinases (ERKs) ERK1/ERK2 regulation [GO:0070374, GO:0071363], stress-activated MAPK [GO:0032872, GO:0031098] cascades, and JAK/STAT cascade [GO:0007259] were also significantly altered following nanosilicate treatment. Among these enriched GO terms, multiple genes displayed notable $\log_2$fold changes in expression such as IGFBP2 ($\log_2$fold:1.358), IGFBP3 (1.149), TAOK1

(-1.864), PDGFRA (-1.394), and HIPK2 (-1.237). A significant change in gene expression of key MAPK signaling regulators was observed.

We also observed that a large number of genes (76 out of 170 genes) related to stress-activated protein kinase signaling [GO:0031098] were differentially expressed due to nanosilicates treatment (**Figure 2-4b**). Specifically, TAOK1, TXNIP and MAP4K4 exhibited a distinct difference in expression between nanosilicate treated hMSCs compared to control hMSCs (**Figure 2-4c**). TAOK1 is an activator of the p38/MAPK14 stress-activated MAPK cascade.[160] The change in mRNA expression levels of TAOK1 *via* RNA-seq was further validated using qRT-PCR (**Figure 2-4d**). These data strongly support the ability of nanosilicates to stimulate MAPK cascade, specifically that of the ERK and p38 pathways (**Figure 2-4e**).

To experimentally validate the role of MAPK signaling pathways following nanosilicate treatment. Reactive oxygen species (ROS) produced by cells treated with and without nanosilicates in presence of ERK inhibitor (PD184352, mitogen activated protein kinase 1 (MEK1) inhibitor) were then monitored using a ROS-sensitive reporter fluorophore (**Figure 2-4f**). ROS play a role in the ERK cascade, in addition to a multitude of other cellular signaling pathways.[161] For nanosilicate-treated hMSCs, a significant reduction in ROS production was observed due to the presence of ERK inhibitor as seen by reduced fluorescence signal (~32% reduction, $p < 0.05$). This regulation of ROS *via* the ERK inhibitor indicates the stimulation of MAPK signaling, specifically that of ERK, by the nanosilicates. The mechanism of this activation may stem from the biophysical cell-nanoparticle interaction, biochemical dissolution, or both in conjunction. This study validates that hMSCs recognize and respond to nanosilicates by engaging intracellular programs such as MAPK cascade (ERK1/2, and p38 kinases).

While RNA-seq analysis provided insight about the role of nanosilicate in stimulating MAPK-related pathways, including those typically stimulated by growth factors in addition to stress-responsive kinases, monitoring protein levels can further provide functional evidence. Differential expression was observed in both upstream (*e.g.* Ras, PRKCA, BRAF) and downstream (*e.g.* ELK1, MKNK2) genes of MEK1/2. In MAPK/ERK cascade, MEK1 and MEK2 are shown to control cell growth and differentiation. [162-163] Activation of MEK1 and MEK2 occurs through phosphorylation by Raf. MEK1/2 inhibitors have been used extensively to implicate ERK1/2 in a wide array of biological events. To validate MAPK/ERK pathways, we monitored synthesis and phosphorylation of MEK1/2 (p-MEK1/2) with and without a MEK1/2 inhibitor (**Figure 2-4g**) via western blot. hMSCs had relatively low production of p-MEK1/2, while nanosilicate treatment results in more than six-fold increase in p-MEK1/2. In the presence of MEK1/2 inhibitor, production of p-MEK1/2 in the presence of nanosilicates was suppressed, demonstrating the role of nanosilicates in activating the MAPK/ERK pathway.

Beyond intracellular phosphorylation events within MAPK cascades, we also investigated genes that may play a role in controlling background processes of hMSCs, like multipotency and motility, that have been identified in previous literature.[164] RNA-seq analysis revealed a significant change in gene expression: AFAP1 ($\log_2$foldΔ: -1.152), SOCS5 (-1.192), WNT5A (-1.162), INHBA (-1.179) from a variety of pathways including TGF-β, JAK/STAT, Wnt/β-catenin, and phosphatidylinositol-3-kinase (PI3K) signaling. These pathways are involved in cell proliferation, cell multipotency, and extracellular matrix production,[165-167] indicating nanosilicate exposure can affect these processes.

2.3.5 Nanosilicates Direct Stem Cell Differentiation.

Following nanosilicates treatment, activation of the membrane can lead to differentiation and extracellular matrix deposition, following either an ERK-based cascade or that of p38.[108-110, 168] The kinase signaling follows similar progressions in hMSCs after growth factor stimulation to promote osteochondral differentiation.[169-173] GO enrichment analysis indicated that nanosilicate-treated hMSCs have a strong ability to differentiate towards bone and cartilage lineages (**Figure 2-5a**). Enriched GO pathways and biological processes related to osteogenesis, such as bone development (GO:0060348), endochondral bone growth (GO:0003416), biomineral tissue development (GO:0031214), and canonical Wnt signaling pathway (GO:0060070) were favored towards osteogenesis. For chondrogenesis, cellular response to transforming growth factor beta stimulus [GO:0071560], cartilage development involved in endochondral bone morphogenesis [GO:0060351], and hyaluronan metabolic process [GO:0030212] were significantly altered. We observed that a large fraction of the genes defining the complete pathway changed their expression due to nanosilicate treatment. For example, 49 genes out of 92 genes were differentially expressed for bone development [GO:0060348], while 10 genes out of 14 genes were differentially expressed for cartilage development [GO:0060351] (**Figure 2-5b**). Genes from these GO categories including cartilage oligomeric matrix protein (COMP), collagen type I alpha 1 chain (COL1A1),

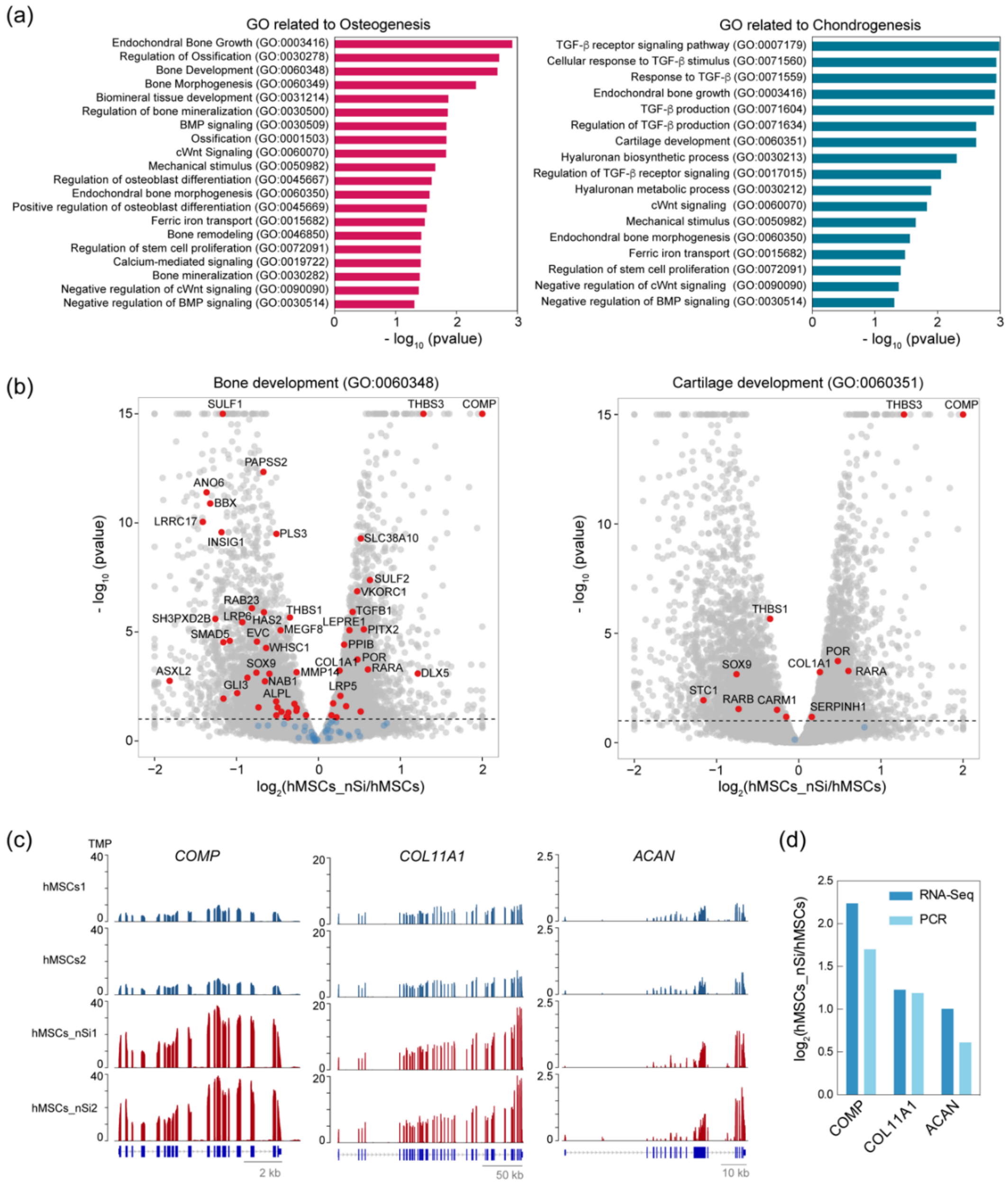

Figure 2-5. Transcriptomic analysis elucidate nanosilicate-induced bioactivity. (a) GO related to osteogenesis and chondrogenesis indicates nanosilicate-induced hMSCs differentiation. (b) Volcano plots from bone development (GO:0060348) and cartilage development (GO:0060351) highlight key differentially regulated genes due to nanosilicate treatment. (c) Gene expression of COMP, COL11A1, ACAN, and COL1A1 demonstrating significant upregulation due to nanosilicate treatment. (d) Differential gene expression from RNA-Seq was validated using qRT-PCR, indicate similar trend. Reprinted with permission from Carrow, Cross et al., 2018.

collagen type XI alpha 1 chain (COL11A1), and aggrecan (ACAN), were significantly upregulated due to nanosilicate treatment (**Figure 2-5c**). We further validated these genes using qRT-PCR and observed comparable gene expression to that of RNA-seq (**Figure 2-5d**).

To validate the translation of mRNAs to protein, western blot of COMP and COL1A1 was performed on day 7. Both COMP and COL1A1 showed a significant increase in expression due to nanosilicate treatment, indicating the role of nanosilicates in hMSCs differentiation (**Figure 2-6a**). Based on the changes in transcriptomic profile and *in vitro* validation, we hypothesize that the activation of MAPK/ERK pathways by nanosilicates may lead to differentiation of hMSCs into osteochondral lineages. To confirm the role nanosilicate in stimulating MAPK/ERK signaling for hMSC differentiation, a MEK1/2 inhibitor was utilized. The presence of MEK1/2 inhibitor resulted in a significant decrease in COMP and COL1A1 synthesis in hMSCs treated with nanosilicates. This confirmed the role of nanosilicates in the activation of MAPK/ERK signaling to direct the differentiation of hMSCs.

Finally, to further substantiate the ability of nanosilicates to drive hMSC differentiation towards bone and cartilage lineages, staining of lineage specific proteins and matrix mineralization was performed. The effect of nanosilicates on chondrogenic and osteogenic differentiation was monitored by subjecting nanosilicate-treated hMSCs to chondro-conductive (lacking TGF-β) and osteo-conductive (lacking bone morphogenetic protein 2 (BMP2) or dexamethasone) media. After 21 days, production of chondro- and osteo-related ECM was observed even in the absence of inductive supplements. An increase in both glycosaminoglycan (GAGs) and aggrecan production were observed in nanosilicate treated hMSCs indicating chondrogenic differentiation (**Figure 2-**

6b), while for osteogenic differentiation, an increase in alkaline phosphatase production as well as matrix mineralization were observed after nanosilicate treatment (**Figure 2-6c**). These results validate the ability of nanosilicates to induce hMSC differentiation into the bone and cartilage lineages without the use of inductive agents and growth factors.

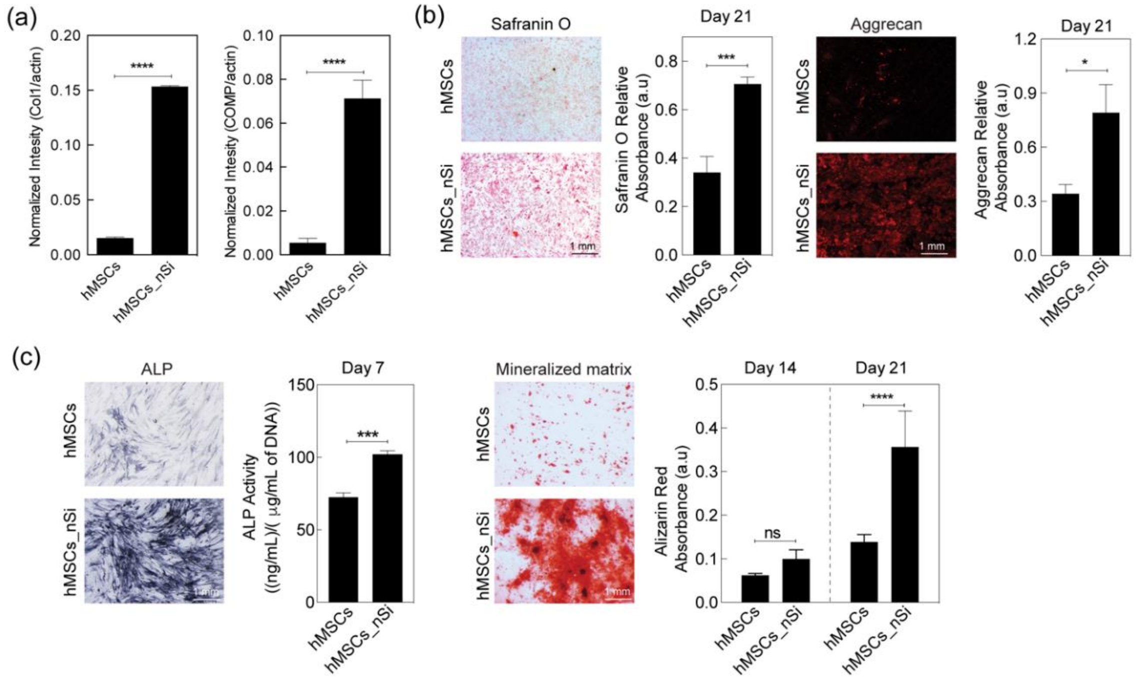

Figure 2-6. Nanosilicate-induced hMSCs differentiation. (a) Western blot data showing production of collagen type I and COMP after exposure to nanosilicates for 7 days in normal media. (b) The effect of nanosilicates on production of GAGs was determined by staining safranin O and aggrecan staining after culturing hMSCs in chondro-conductive media for 21 days. (c) The effect of nanosilicates on osteogenic differentiation was determined by ALP activity and formation of mineralized matrix after culturing hMSCs in osteo-conductive media for 21 days. Reprinted with permission from Carrow, Cross et al., 2018.

The broader relevance of our study is that "*omics*" techniques can be used to determine the effect of nanomaterials on cells in a non-targeted and non-biased approach. The physicochemical properties of engineered nanomaterials such as size, shape, surface charge and chemical composition, will have profound effects on cellular behavior.[107, 157] Therefore, we absolutely do not speculate that the transcriptomic changes observed in this study will be universal to all type of nanomaterials. Recent studies have used "*omics*" approaches to understand the nanotoxicology and mechanism-based risk assessment of nanomaterials.[174] The current study demonstrates the capabilities of next generation sequencing to provide an unbiased mRNA expression levels of all the expressed genes in the cell due to nanomaterials treatment. Our approach of performing RNA-seq overcomes the limitation of measuring expression levels of fewer pre-selected genes on the microarrays, which will help in identifying the potential of nanomaterials for regenerative medicine. Additionally, unlike microarrays technology, RNA-seq delivers low background signal and sequenced reads that can be unambiguously mapped to unique regions of the genome, which will help in precise identification of the expressed genes. For example, the transcriptomic insight on the role of surface-mediated cellular signaling confirms the ability of nanosilicates to induce hMSC differentiation into the bone and cartilage lineages in the absence of inductive agents. This new insight can help in reducing or eliminating the use of supraphysiological doses of growth factors that are currently used in clinical practice for regenerative therapies. These "*omics*" techniques can be used to understand cell-materials interactions that are unique to different nanoparticles and can contribute directly to the design of next-generation bioactive materials for regenerative medicine.

2.4 Conclusion

Overall, we investigated the transcriptomic dynamics in hMSCs following exposure to 2D nanosilicates. A widespread change in transcriptomic profile was observed in response to nanosilicate exposure and more than 4,000 genes were differentially regulated. Such widespread effects due to nanosilicate treatment are probably attributed to both biophysical and biochemical mechanisms. The interaction of nanosilicates with the cell membrane stimulated various surface receptors, including the stress-responsive and surface receptor mediated mitogen activated protein kinase (MAPK) pathways. Similarly, the data indicates that internalization of nanosilicates and subsequent release of mineral ions in the cytosol trigger biochemical signaling, that could enhance osteochondral differentiation of hMSCs. Accordingly, analysis of the transcriptomic snapshot of hMSCs treated with nanosilicates uncovered families of genes with gene ontologies related to osteochondral differentiation. *In vitro* studies validated the RNA-seq findings and further supported the observation that nanosilicates have the capacity to direct hMSC differentiation towards bone and cartilage lineages. Lastly, RNA-seq was demonstrated as a viable technique to evaluate the regenerative potential of novel nanomaterials.

3. NANOSILICATE-POLYSACCHARIDE COMPOSITES FOR CARTILAGE BIOPRINTING[*]

3.1 Introduction

Tissue engineering aims to regenerate tissues and organs in three-dimensional (3D) space with precisely controlled microenvironments for tissue repair following a variety of disease pathologies.[175-177] Recently, there has been tremendous progress in developing multifunctional biomaterials for facile cellular encapsulation and delivery to shield cellular material from high shear forces, thereby improving cell viability.[178-180] Polymeric hydrogels are often used towards this because they are highly hydrated network and can mimic some of the characteristics of native microenvironment.[91, 94, 181-182] However, inability to retain microstructural integrity of polymeric hydrogels under dynamic stress limits their utility for various biomedical applications. Hence designing hydrogels with high stiffness and toughness with physiological stability is imperative.[183-184] Therefore, despite recent progress, designing a multifunctional hydrogel scaffold to accomplish the cellular encapsulation and delivery for tissue regeneration is challenging. Some of the challenges that need to be addressed to obtain functional tissues include weak mechanical properties, lack of control over the scaffold architecture, and limited ability of biomaterials to interact with cellular components.[185-186]

A range of nanomaterials such as polymeric, carbon-based, metallic oxide and inorganic nanomaterials are incorporated within the polymeric network to obtain multifunctional

---

[*] Unpublished work J.K. Carrow, A. Bock, A.K. Gaharwar, "Dual-Crosslinked Polysaccharide Nanoclay Composite for Cartilage Bioprinting" (*in prep*). *Supplemented with permission* from "Thakur, A.; Jaiswal, M.K.; Peak, C.W.; Carrow, J.K.; Gentry, J.; Dolatshahi-Pirouz, A.; Gaharwar, A.K. Multifunctional Hydrogels Reinforced with Two-dimensional (2D) Nanomaterials for Cell Delivery," *Nanoscale* 2016. Copyright 2016 Royal Society of Chemistry

hydrogels.[1, 187-189] A new family of two-dimensional (2D) nanomaterials have been shown to have exceptional mechanical strength, and electrical conductivity, due to their ultrathin 2D structure.[190-193] These 2D nanomaterials have high structural anisotropy and surface-to-volume ratio. Although these 2D nanomaterials are in early stage of development, they have shown potential in engineering multifunctional biomaterials for various medical applications including photothermal therapies, therapeutic delivery, tissue regeneration, bioimaging, and biosensors.[191]

Synthetic silicates, an ultrathin class of 2D nanomaterials, have been shown to strongly interact with synthetic and natural polymers due to high surface-to-volume ratio, similar to other types of 2D nanomaterials.[117] These nanosilicates results in the formation of shear-thinning hydrogels when combined with long-chain polymers.[194-197] Our earlier work has shown high cyto- and bio-compatibility of these 2D nanosilicates (nSi).[194, 198-199] Moreover, these 2D nanosilicates also interact with growth factors and are explored for tissue engineering[198] and therapeutic delivery[200]. Thus, by reinforcing polymeric hydrogels with these 2D nanosilicates, we can develop multifunctional hydrogels for biomedical and biotechnological applications.

Here, we fabricate a dual-crosslinked, mechanically robust kappa-Carrageenan (κCA) hydrogels reinforced with 2D nanosilicates (**Figure 3-1**). This hydrogel system will likewise be tailored toward bioprinting applications with special consideration around printability of the bioink compositions as well as viability of cells following extrusion. κCA is a natural polysaccharide that resembles native glycosaminoglycans (GAGs) such as chondroitin-4-sulphate and dermatan sulphate, which are major components of native extracellular matrices (ECM).[201-203] Previous studies have shown that in the presence of potassium ions (K^+), κCA can form brittle hydrogels.[204] Under physiological conditions, ionically crosslinked κCA loses its mechanical integrity, thereby limiting its biomedical application. To overcome these limitations, we propose to develop a multifunctional dual-crosslinked κCA hydrogels. The chemical modification of the κCA backbone with photocrosslinkable methacrylate group can provide enhanced structural stability under physiological conditions. Furthermore, by reinforcing the covalently crosslinked κCA network with 2D nanosilicates, an increase in the mechanical stiffness, elastomeric characteristics, and physiological stability is expected. The proposed multifunctional hydrogel networks have the potential to be used for delivery of cells and therapeutics for soft tissue regeneration and 3D bioprinting.

3.2 Materials and Methods

3.2.1 Synthesis of Methacrylated kappa Carrageenan (MκCA). Kappa-Carrageenan (κCA, Tokyo Chemical Industries, Japan), Methacrylic anhydride (MA,> 94%, Sigma Aldrich, USA) and nanosilicates (nSi, BYK Additives Pvt. Ltd, USA), potassium chloride (KCl, Alfa-Aesar, USA) were used without further purification. For all experiments ultrapure water (resistivity > 18.2 MΩ.cm) was used unless otherwise stated. Methacrylation of κCA was carried out by dissolving 2% κCA solution in 150 mL water and then vigorously mixed with 12 mL of MA at 50°C. To maintain the pH (>7.4), 5M NaOH was added drop-wise. After 6h the resulting precipitate was dialyzed using cellulose dialysis membrane (Mol. wt. cut-off ~ 12-14 kDa) at 4°C against ultrapure water for a week to remove any unreacted reagent and by-products (e.g. methacrylic acid). The dialyzed product was lyophilized and stored at -20°C for further use.

3.2.2 Fabrication of dual crosslinked hydrogels. Prepolymer solutions of various wt. % concentrations of MκCA, up to 5%, were prepared in ultrapure water. Nanocomposites of MκCA with nanosilicates (MκCA-nSi) were fabricated by adding multiple wt. % of nSi, up to 8% and vortexed vigorously for 2 min. nSi were allowed to mix and exfoliate within the solution overnight to ensure particles were homogenously distributed. Samples were prepared by injecting the prepolymer solution in disc-shaped polydimethylsiloxane molds (7mm diameter and 2mm height). For κCA loaded solutions, 5% potassium chloride (KCl) was added to molds until they were fully covered. Following 1 min incubation, the molds were gently agitated to remove hydrogels. Preparation of MκCA and MκCA-nSi dual crosslinked gels was achieved by 60 sec UV irradiation (7 mW/cm2) prior to 1 min KCl incubation.

3.2.3 Physiochemical and structural characterization. Attenuated total infra-red reflection (ATR) was performed for nanocomposite hydrogels along with kCA using ATR spectrophotometer (Bruker Vector 22, PIKE Technologies, USA). ^{1}H NMR (300 MHz, D2O, δ): 3.75 ppm (d, G6; $-\mathrm{CHC}\mathbf{H_2}\mathrm{OH}$), 5.5 ppm (s, vinyl; $-\mathrm{C}{=}\mathrm{C}\mathbf{H_2}$), 1.81 ppm (s, methyl; $-\mathrm{C}\mathbf{CH_3}$) confirmed methacrylation of κCA. Specifically, the ratio of integrated new peaks to that of G6 protons was used to calculate degree of methacrylation (DM). Methacrylation of κCA was confirmed by X-ray photoelectron spectroscopy (XPS, Omicron DAR 400) equipped with Mg (K_α) X-ray sources. Casa XPS software was then used for deconvolution of the peaks and further analysis.

3.2.4 Rheological and mechanical analyses. A Discovery Hybrid Rheometer 2 (DHR-2) (TA Instruments) with attached 20 mm parallel plate was set to a gap height of 0.25 mm and 37 °C for all experiments unless otherwise specified. Compositions were tested in uncrosslinked forms, except during creep experiments where a crosslinked gel was used. For creep experiments, gap height was set to 1 mm and a temperature of 25 °C. A constant stress of 2.0 Pa was applied for 4 minutes followed by 12 minutes of no stress applied. For printing mimic rheology studies, temperature was 25 °C three separate shear rates (0.023, 2000, 0.015 1/s) were applied to the ink correlating with each region of the extruder (barrel, nozzle, and bed, respectively).[205] Furthermore, the duration spent at each of these shear rates differed to model time spent in each location during the printing process. UV light (7 mW/cm^2) was likewise applied within the final low shear region to simulate on-demand crosslinking from the extruder. Rotational temperature sweeps were executed at 1 Pa, 1 Hz over a temperature range of 20-50 °C to evaluate stability of bioinks upon heating. An oscillatory stress sweep at 1 Hz was completed over a range of stresses spanning 0.1 to 1000 Pa, with 10 points measured per decade. An ADMET eXpert 7600 Single Column Testing System was used for cyclic compression testing of mold casted hydrogels. Strain rate of 20% strain/min was used to compress the samples to 50% of original height. The compressive modulus and energy dissipated was calculated and plotted to compare gels versus native cartilage from an equine osteochondral explant (acquired from Comparative Orthopedics and Regenerative Medicine Lab, Texas A&M).

3.2.5 Analysis of Aqueous Stability. For line swelling evaluation, a HYREL 3D printer was used to print the lines with a 23-gauge needle. The extruder temperature was held constant at 37˚C. The layer height was 413 microns and the bed movement speed was set to 1800 mm/min. The lines were imaged with ZEISS stereomicroscope prior to being submerged in either PBS or a media solution for 24 hours. The width of the line was then taken again after 24 hours for comparison to pre-swelling width. Degree of hydration studies were completed over the course of 5 weeks. Briefly, 5% MκCA gels (8 mm diameter, 2 mm height) with varying nSi concentrations were cast into silicone molds and prepared with either a UV or UV/KCl crosslinking mechanism. UV exposure was limited to 45 seconds at an intensity of 7 mW/cm^2 and KCl incubation, following

UV crosslinking, lasted 5 minutes at room temperature. As prepared gel weights at Day 0 were compared against swollen gels at various time points following the addition of cell media. Media was changed following each measurement.

3.2.6 In vitro Cell Analysis and 3D Bioprinting. Human mesenchymal stem cells (hMSC) and preosteoblasts (MC3T3) obtained from Lonza were cultured in growth media supplemented with 16.5% FBS and 1% Streptomycin/Penicillin (αMEM, Life Technologies, USA) at 37 °C under 5% CO_2 atmosphere. hMSCs and MC3T3s were encapsulated in prepolymer solutions containing κCA, MκCA, or MκCA-nSi at a density of 10^5 cells/gel. Cellular viability was assessed using Calcein AM for live cells and ethidium homodimer for dead cells according to manufacturer's protocol (Life Technologies, USA). In typical procedure, prepolymer solutions were physically mixed with cells, injected using a flow rate of 1000 µL/mL with a 27-gauge needle, and covalently crosslinked to form hydrogels in a 48-well plate. All samples were carried out in triplicates. After 24 and 72 h, samples were washed with 1X DPBS, incubated in stains for 30 mins at physiological conditions. The stained samples were subsequently washed with 1X DPBS and imaged with fluorescence microscope (Nikon, TE2000-S). Percent viability was calculated by using Image *J* (NIH) software. To determine the cell morphology, encapsulated cells were stained with actin cytoskeletal staining (Phalloidin-Alexa 488, Invitrogen) was performed according to manufacturer's protocol and nucleus were counterstained with propidium iodide (PI).To evaluate the metabolic activity of seeded hMSCs on nanocomposite hydrogels surface, alamarBlue assay at 24h and 72h after seeding was performed.

Encapsulated viability following the printing process and UV crosslinking was also examined with MC3T3s. Printed scaffolds with encapsulated cells were evaluated at time points of 1, 3, 14, and 28 days of culture. To determine the dispersion of cells within scaffolds over the course of the printing process, a CellTracker Green CMFDA dye (ThermoFisher Scientific) was used according to manufacturer's protocol. Briefly, the dye was incubated with cells prior to the resuspension in the bioink solution and subsequent loading into the extruder barrel. Barrel and printing bed temperature were maintained at 37 °C.

A HYREL System 30 M 3D printer was utilized for scaffold printing. Bioink with or without encapsulated cells were loaded into a HYREL VCD-25 extruder for temperature control and UV on-demand crosslinking. The nozzle was equipped with a luer lock adapter and 23 gauge needle (5 mm, blunt stainless steel, Jensen Global Inc., USA). Scaffolds were modeled in Solidworks 3D CAD Design, which was imported into Slic3r ver. 1.2.9. The Slic3r generated G-code files were then uploaded to the HYREL-based software, Repetrel, and printed at 37 °C onto a glass slide with a layer height of 410 µm and bed speed of 1800 mm/min. During the printing process, layers were crosslinked with UV light at an intensity of 7 mW/cm^2.

3.2.7 Statistical analysis: The data presented as mean ± standard deviation of the experiments (n=3, unless otherwise stated). Statistical analysis was performed using nonparametric test, one-way analysis of variance (ANOVA) with Tukey's *post-hoc* pairwise mean comparisons. The statistical significance was defined as $^*p<0.05$, $^{**}p<0.01$, $^{***}p<0.005$.

3.3 Results and Discussion

3.3.1 Polymer Characterization and Substitution

Carrageenan (CA) is an anionic natural hydrophilic biopolymer extracted from seaweed and is available in many forms based on chemical configuration.[206] It is widely used in several applications such as a gelling agent, wound healing, cell therapy, emulsifier, and food enhancer.[207]

Chemically each unit of CA is comprised of alternating disaccharide repeating subunits of 3-linked β-D-galactopyranose (G subunits) and 4-linked α-D-galactopyranose (D subunits). Based on the configuration and number of sulfate groups in CA, it is divided into three major classes.[208-209] CA with one sulfate group forms kappa carrageenan (κCA), while with two and three it forms iota (γCA) and lambda carrageenan (λCA), respectively. Because of the structural resemblance with natural glycosaminoglycans (GAGs), κCA, is the most widely used carrageenan polymer.[210] The network formation in κCA occurs by binding of cationic agents (e.g. K+) to the sulfates present in the structural backbone.[209] Chemical modification of the polymer can be achieved to render the solution UV crosslinkable. Furthermore, the ionic network formation mechanism can remain intact to provide a dual-crosslinking capability (**Figure 3-1**). To obtain a covalently crosslinked polymer network, we modified the κCA backbone with methacylic anhydride (MA) to obtain methacrylated κCA (MκCA).

The methacrylation of κCA was achieved on the primary and secondary hydroxyl groups of the two subunits of the polysaccharides (**Figure 3-2a).** The chemical modification of κCA was confirmed using X-ray photoelectron spectra (XPS) analysis. Specifically, we obtained spectra for core-level carbon electron (C 1*s*) and oxygen electron (O 1*s*) for κCA, MκCA, and crosslinked MκCA (UV crosslinked) (**Figure 3-2b**). The atomic ratios of oxygen to carbon (O/C) and sulfur to oxygen (S/O) along with their individual values for samples kCA and MkCA, estimated from area under the curve from XPS spectra are presented in the table (Fig. 2b). In kCA the overall contribution from carbon is approx. three times to oxygen (O/C, 0.32) and of oxygen is ten times to sulfur (S/O, 0.10). Due to methacrylation, the methacrylic groups contributed to the oxygen content and the ratio of carbon is reduced only two times to oxygen (O/C, 0.52). Also S contribution is slightly enhanced (S/O, 0.16).

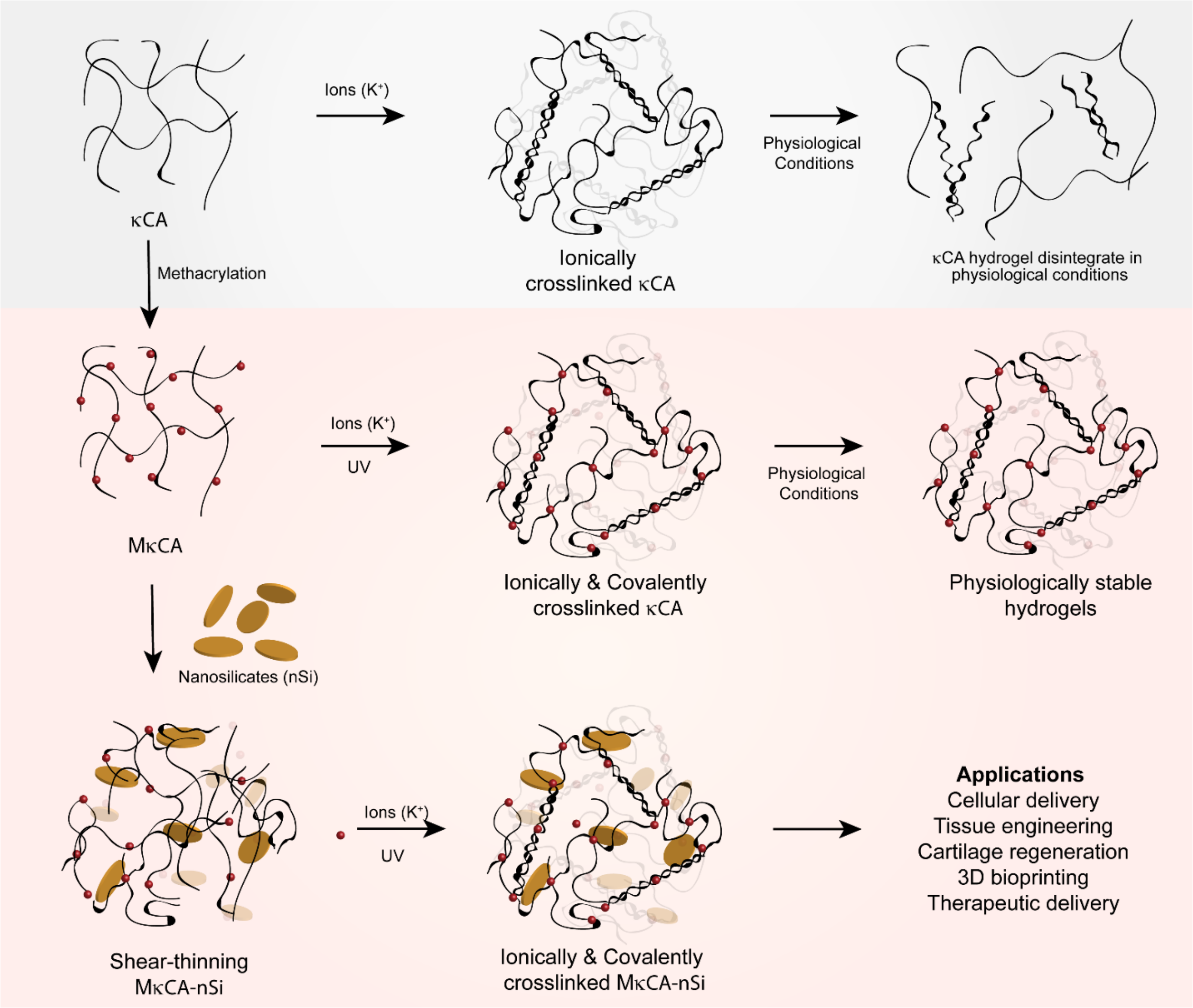

Figure 3-1. Schematic outlining the design strategy to synthesize multifunctional nanocomposite hydrogels. κCA is predominantly crosslinked in the presence of potassium ions (sulfate groups interact with K^+ ions to drive a helical polymer conformation), which loses its mechanical stability under physiological conditions. Methacrylation of κCA results in a covalently crosslinkable polymer. The addition of nanosilicates provides shear thinning and bioactive properties to the polymer that can be used in various tissue engineering applications. Reprinted with permission from Thakur et al., 2016.

After UV exposure, due to the formation of crosslinked gel via C-C, there occurs reduction in O owing to water formation as by product (O/C, 0.26) suggesting carbon contribution up to four time to oxygen and sulfur content raised to about fifty percent of oxygen (O/S, 0.52). The overall atomic ratio estimation clearly corroborated the formation of covalently crosslinked gel after UV exposure. The deconvoluted peaks of C 1*s* core-level for κCA shows the presence of C-OH (287.8 eV), C-O (286.1 eV), and C-C at 284.7 eV. After methacrylation, additional peaks at 287.1 and 285.8 eV from MκCA (prepolymer) revealed the presence of C=O and C=C, which are attributed to methacryloyl. This confirms the successful methacrylation of κCA backbone. MκCA was used to obtain covalently crosslinked network after UV exposure in the presence of photoinitiator (Irgacure 2959). After UV exposure, the C=C bonds from vinyl groups in MκCA disappear, indicating the formation of a covalent crosslinked network. The remnant peaks seen in the modified formulation exist from incomplete crosslinking; suggesting that some C=C might still be available. Similarly, XPS analysis of core-level oxygen electron (O 1*s*) supports the covalent modification of κCA. For κCA, the presence of C-OH (534.5 eV) and C-O-C (534.2 eV) were observed. After methacrylation, disappearance of O 1*s* peak corresponding to C-OH and appearance of a new peak (533.8 eV) attributed to C=O was observed. The O 1*s* peaks corresponding to O-C, O-S and C-O-C have shifted toward lower binding energies due to methacrylation. After UV exposure, the O 1*s* peaks remained nearly unchanged, as oxygen does not take part in subunits crosslinking and polymerization. The incorporation of nanosilicates (nSi) to MκCA, showed minimum effect on the crosslinking process. With the addition of 2% nSi the overall contour of the C 1*s* profile became broader, without affecting the peak position, confirming the electrostatic interaction between nSi and MκCA backbone. In addition to XPS data, NMR analysis indicated successful modifications to the polymer backbone (**Figure 3-2c**). Specifically, to determine degree of substitution, peaks correlating to the added methyl and vinyl groups, ~1.8-1.9 ppm and ~5.2-5.6 ppm respectively, were calculated against methylene protons of the β-galactose subunit (G6). Integration of these peaks indicated a degree of methacrylation ~25%, similar to previous reports using the same volume of methacrylic anhydride. Overall, XPS and NMR data confirms the chemical modification of κCA and subsequent formation of covalently crosslinked network from MκCA upon UV exposure.

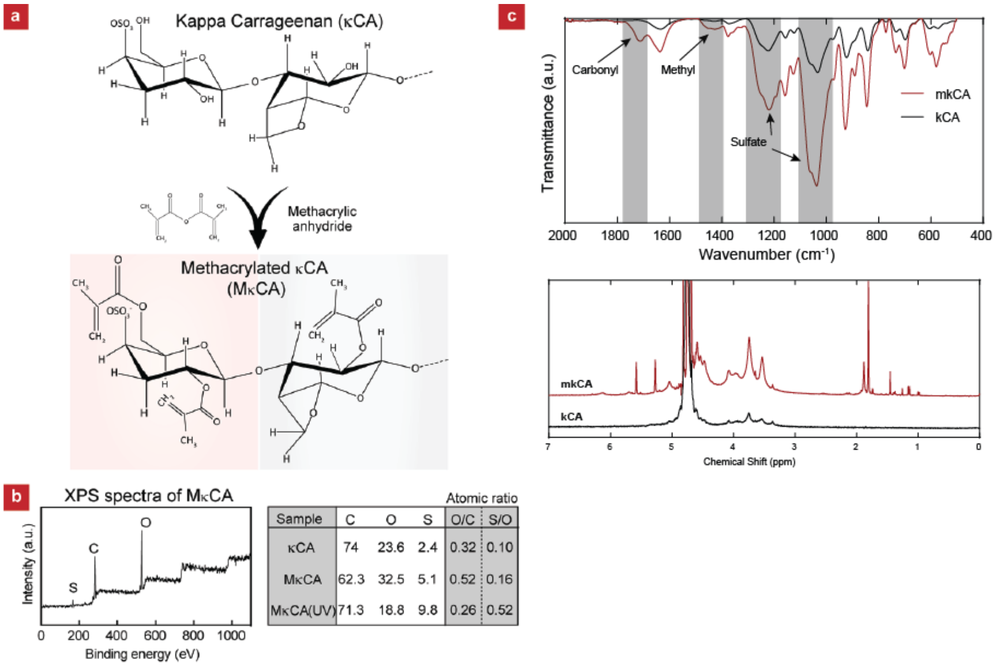

Atomic ratio

Sample	C	O	S	O/C	S/O
κCA	74	23.6	2.4	0.32	0.10
MκCA	62.3	32.5	5.1	0.52	0.16
MκCA(UV)	71.3	18.8	9.8	0.26	0.52

Figure 3-2. Synthesis of photocrosslinkable MκCA. (a) The hydroxyl groups (-OH) in the polymer backbone were modified with photocrosslinkable methacrylates. (b) Full x-ray photoelectron spectroscopy (XPS) of MkCA. (c) FTIR reveals vibrational absorption peaks correlating with the formation of carbonyl and methyl functional groups. Sulfate groups responsible for ionic crosslinking remain intact. NMR corroborates the XPS and FTIR findings which indicated successful chemical modification of MκCA. Reprinted with permission from Thakur et al., 2016.

3.3.2 Physical Characterization of Hydrogel Formulations

κCA is used as a thickening agent in various applications due to its ability to form 3D double helices network that results in strong interactions between sulfate groups present on polymer backbone.[201] The chemical modification of κCA backbone is expected to influence the sol-gel behavior of prepolymer network. Specifically, the addition of methacrylate side groups is expected to change the stacking of κCA polymer chains and disrupting the sol-gel behavior. Solution of 2% κCA showed a "gel-like" behavior at room temperature, while MκCA showed a "sol-like" behavior **(Figure 3-3a)**.

The mechanical properties of hydrogels govern cellular response since cells sense and respond to mechanical cues.[211] A range of soft and stiff hydrogels have shown to modulate the cell adhesion, proliferation and fate.[212-213] Ionically crosslinked κCA hydrogels are mechanically stiff initially, but quickly lose the mechanical integrity after being subjected to hydrated microenvironment as a result of ion exchange. In addition, ionically crosslinked κCA hydrogels are not elastomeric **(Figure 3-3b)** and this limits their use in biomedical applications. When subjected to cyclic stress, the ionically crosslinked κCA hydrogels do not recover to original size and show significant plastic deformation. By incorporating methacrylate groups to κCA backbone, significant loss in mechanical stiffness was observed. This is similar to previously reports suggesting that methacrylate groups present on the MκCA backbone limit the ability of polymer to form ionic crosslinks.[214] Interestingly, continuously increasing the concentration of nSi content at two separate MκCA concentrations did not display continuous improvement in mechanical properties. In actuality, compositions with 2 wt. % nSi provided the strongest matrix in compression. These compositions, however, also dissipated the greatest amount of energy, indicating a reduction in the elastic nature.

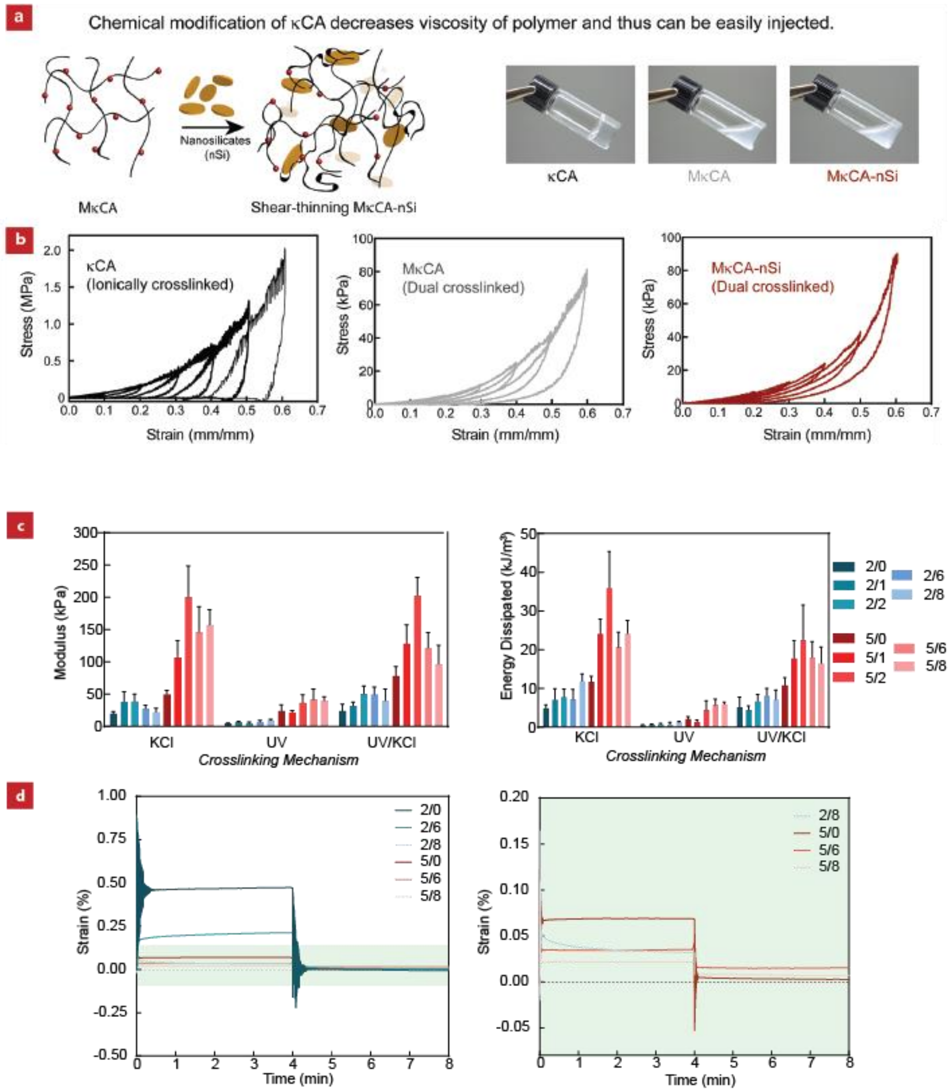

Figure 3-3. Nanosilicates effects on nanocomposite. (a) The addition of nanosilicates (nSi) decreases viscosity of prepolymer solution. (b) The cyclic stress/strain curves for κCA, MκCA and MκCA-nSi shows the elastomeric characteristics of hydrogel network. Both MκCA and MκCA-nSi hydrogels recovery after cyclic deformation. (c) Mechanical properties of each composition are dependent on crosslinking mechanism with ionic crosslinking generating a strong/brittle gel and UV imparting elasticity onto the network. (d) Creep response on UV crosslinked compositions further indicates the elastic response to dynamic stresses. The addition of nSi's decreases resulting strain across the gel for both low and high polymer compositions. Modified with permission from Thakur et al., 2016.

Mechanical comparisons between crosslinking mechanism also showed a decrease in mechanical strength between physically and chemically crosslinked gels. For dual-crosslinked gels, compressive mechanics displayed components of both ionic and UV mechanisms.

The modulus values for all compositions resided between ionic and chemical alone; in addition, the mechanism strongly dictated these dynamic responses to load with very little energy dissipation occurring within pure UV crosslinked constructs (**Figure 3-3c**). In the case of dual-crosslinked hydrogels, the ionic crosslinks were a greater contributor to scaffold mechanics; however, the presence of covalent crosslinks did slightly reduce dissipated energy. UV crosslinked gels also provided substantial elastic recoil during time-dependent creep rheology, indicating the covalent bonds formed via this mechanism provide the majority of elastic behavior under dynamic stress, which is imperative for cartilage applications (**Figure 3-3d**).

3.3.3 Characterization of Bioink under Printing Conditions

To further evaluate optimal formulations of the MκCA-nSi composites, extrusion and subsequent line width out of multiple needle gauges at various flow rates was evaluated. Specifically, line width was normalized against the inner diameter of either an 18 or 22 gauge needle (**Figure 3-4a**). While for the larger needle size and at each flow rate, the trends remained consistent with a decrease in line size correlating with an increase in nSi concentration. In contrast, extruded line width from the smaller needle gauge displayed greater dependency on polymer concentration and flow rate. Interestingly, the 5%/8% MκCA-nSi composition displayed desirable control over the deposition for both needle gauge sizes and the range of flow rates. Due to mechanical stability and beneficial extrusion characteristics, the higher nSi concentrations as well as 5% MκCA compositions were of further interest.

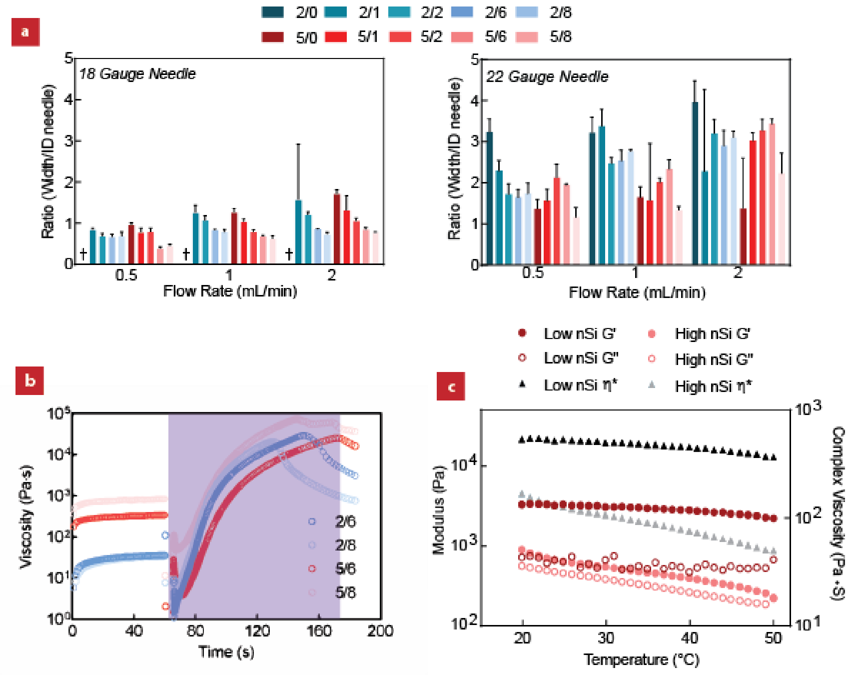

Figure 3-4. Evaluation of bioprinting capabilities. (a) Compositions were extruded over multiple flow rates through two sets of needle sizes to evaluate extrudate swelling upon exiting the nozzle. Greater control over fiber size was maintained at lower flow rates. (b) Rheology mimicking the printing process evaluated the ability of the material to regain mechanical stability after experiencing high shear through the nozzle (purple region indicates UV exposure). (c) A temperature sweep evaluated the stability of two bioink compositions with increasing temperature. (Low nSi – 2%; High nSi – 8%)

The timing of bioink recovery and crosslinking after extrusion plays a significant role during the printing process and can be attributed in part to the organization of solution components within the extruder and nozzle. The presence of nanosilicates within the bioink provides a potential source of stability within low shear domains due to electrostatic interactions between particles in addition to between particles and the polymer. Specifically, charged side groups (i.e. sulfate) off of the κCA backbone may interact favorably with the positive edge of the nanosilicates. Upon methacrylating κCA, the inherent shear-thinning characteristic of the polysaccharide is nearly eliminated.[215] Previous studies have documented the ability of nanosilicates to endow viscoelastic properties, like shear-thinning behavior, to polymeric solutions.[205, 216] Specifically, the structured organization of nanosilicates in aqueous environments results in a complex integrated network with the polymer, directly impacting flow properties. These electrostatic interactions can be disrupted via an application of high shear stresses, thereby reducing the effective viscosity. A rheometer was utilized to simulate shear rates and UV crosslinking (purple region) experienced during the printing process in the barrel, nozzle, and on the printer bed (**Figure 3-4b**). Following extrusion and subsequent UV exposure, ink viscosity surpassed values within the low shear region after 30 seconds for all tested compositions. For compositions with high nanosilicate content (6% and 8%), these solutions demonstrated favorable for printing shear-thinning properties. Additionally, the ratio of polymer:nSi impacted flow as a higher polymer concentration reduced potential electrostatic interactions between particles, subsequently reducing the measured viscosity.

During an extrusion-based printing process, syringe barrel, nozzle, and/or printer bed may be heated to ensure cell viability is maintained over the course of fabrication. The impact of heating on extrusion and structure fidelity, however, is highly dependent on bioink polymer in addition to any additives.

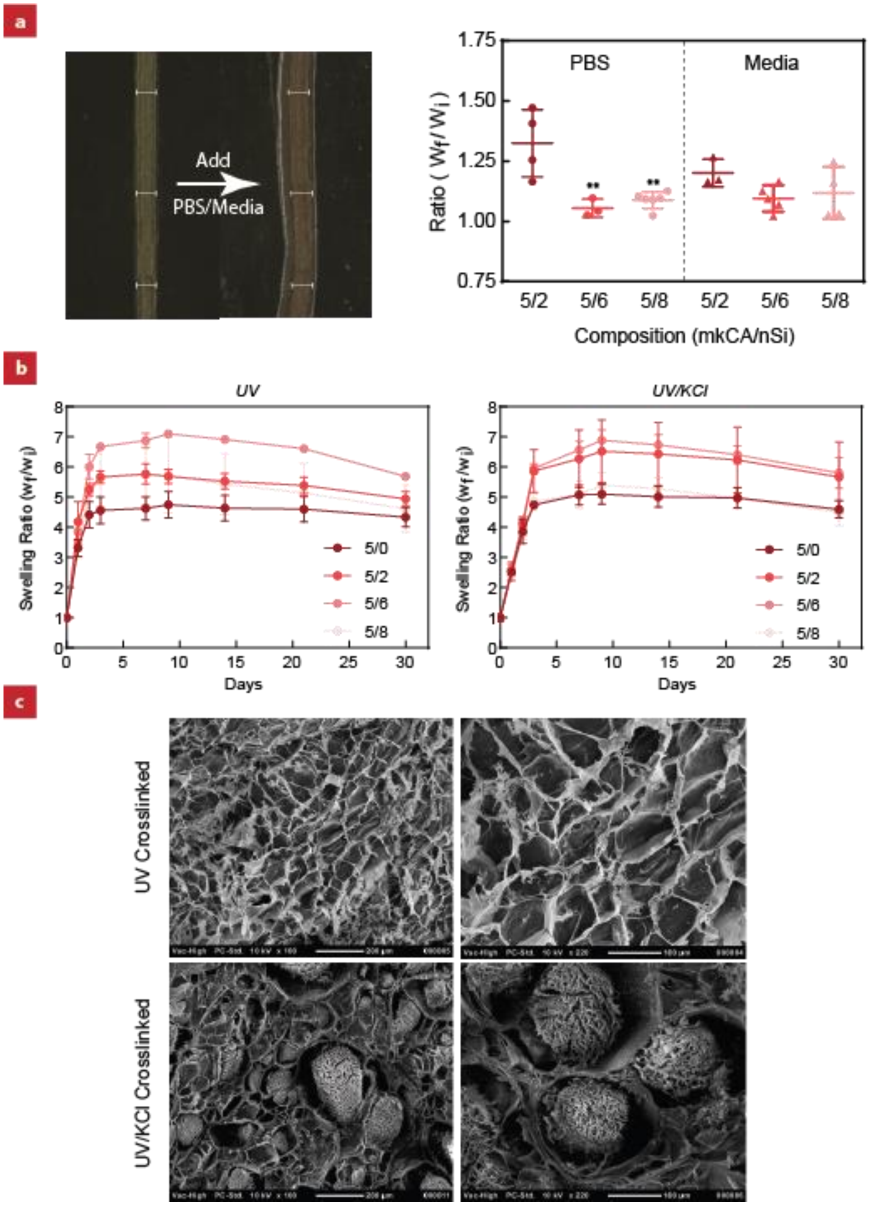

Figure 3-5. Nanocomposite response to aqueous environments. (a) Swelling of extruded and UV crosslinked fibers evaluated degree of physical swelling following placement into two biologically relevant aqueous environments for 24 hours. (b) Bulk gels were placed within media following either UV or UV/KCl crosslinking to evaluating degrees of mass swelling for multiple compositions over 30 days. (c) SEM images of both UV and UV/KCl crosslinked hydrogels indicate the presence of a secondary network formation following the presentation of K^+ ions.

Prior to methacrylation, κCA solutions experience a high degree of temperature dependence regarding gelation. At low temperatures, the κCA backbone conformation transitions from a coil into double helix, through a sulfate side group-mediated mechanism, thereby increasing the viscosity. Upon further cooling and introduction of monovalent cations (e.g K^+, Na^+), the helices can further rearrange into helix-helix aggregates, resulting in stable gel formation. The chemical functionalization via methacrylic anhydride may disrupt this organization, thereby reducing the viscosity of MκCA solutions at similar concentrations to their κCA counterparts. To ensure these modifications would not translate to thermal instability at physiological temperatures, a thermal rheological sweep was completed over both low nSi and high nSi bioink formulations (**Figure 3-4c**). Both compositions showed mechanical stability with little effect on modulus and viscosity, particularly between room and body temperature (25-37 °C). These results indicate that control over extrusion could be maintained even with the addition of temperature; furthermore, architecture of deposited hydrogel fibers would not be expected to shift due to maintenance of ink stability. On-demand UV crosslinking further constrains fiber architecture to limit post-extrusion spreading. This subsequently maintains the nozzle to substrate height over the course of the printing process, improving interlayer and overall construct stability.

3.3.4 Bioink Stability in Aqueous Conditions

While interactions between printed layers during the printing process are vital to the overall stability of the scaffold, swelling effects following placement into aqueous media can also disrupt these interactions. Hydration is key for the survival of encapsulated cells within the hydrogels for nutrient and waste transport; however, swelling of the polymer matrix can alter the geometry that was initially controlled during extrusion. For example, the occlusion of macroscopic pores or a lumen in the case of vascular engineering can severely limit flow of media throughout the scaffold, leading to regions of limited nutrients and oxygen and subsequent cell death. Therefore, knowledge regarding swelling characteristics within aqueous environments is necessary to predict scaffold success. To examine these properties of MκCA-nSi compositions, we explored both individual line swelling and bulk gel hydration over time in relevant biological media. UV crosslinked 5% MκCA compositions with greater nSi content displayed reduced swelling compared to the lowest nSi concentration in both PBS and cell media conditions (**Figure 3-5a**). We hypothesize that the electrostatic interactions between the polymer sulfate groups and the positive edge of the nSi's reduce the potential swelling deformation. It is important to note, however, that in each composition tested, on average, the diameter of the fibers did not expand beyond 33% of the original size, indicating an acceptable degree of line swelling for these compositions, particularly 5%/6% and 5%/8% MκCA-nSi. Further, for bulk gels undergoing either UV or UV/KCl crosslinking mechanisms, swelling ratios were comparable to other polymeric hydrogels typically used as bioinks, like alginate and PEG (**Figure 3-5b**).[217-219] Swelling ratio of all compositions were largely independent of crosslinking mechanism as those gels that received only UV exposure would be subsequently placed into a buffered media solution, where the presence of ions would further enable ionic crosslinking to take place. This ion exchange within the gels would essentially result in a dual-crosslinked network, similar to the UV/KCl subset. Interestingly, bulk gels lacking nSi's maintained the lowest degree of swelling out of all compositions.

To understand the material changes from the perspective of the cellular environment following dual-crosslinking and placement into an aqueous environment, SEM images were captured of both

UV and UV/KCl crosslinked gel networks (**Figure 3-5c**). Covalently crosslinked 5%/8% MκCA-nSi gels displayed a network typical of polymer hydrogels with a fairly uniform mesh size appearing after lyophilization. In contrast, the exposure to both a covalent and ionic crosslinking mechanism generated a unique network organization. Specifically the visualization of intramesh crosslinking may indicate the formation of secondary networks after the introduction of KCl. Residual polymer chains that failed to crosslink during UV exposure may enable the formation of these secondary clusters of highly crosslinked polymer. The formation of high density polymer regions may also be responsible for the increase in mechanical strength measured previously. The impact of these domains on cell viability after completing the printing process and crosslinking, requires further investigation.

3.3.5 Bioink Interactions with Cellular Components

Shear-thinning and injectable hydrogels can be used for minimally invasive therapies and 3D printing. Injectable hydrogels have been shown to protect encapsulated cells from the damaging effects of extensional flow.[178-179] We expect that the shear-thinning characteristics of nanocomposite hydrogels can be explored for these applications in the future. The ability of the ink to recover after extrusion contributes directly to resolution of the printed architecture. Printing of lattice structures can qualitatively demonstrate the ability to control fiber deposition in addition to assessing fiber sag between struts. Lattices printed with the 5%/8% composition demonstrated a high degree of control over fiber diameter during printing while also minimizing fiber sag due to the internal structure provided by the nSi's (**Figure 3-6**). Upon crosslinking, lattices were durable and could be easily handled for further analysis. We have investigated the effect of shear forces by encapsulating stem cells within prepolymer solution and injecting though 27-gauge syringe **(Figure 3-7a)**. The encapsulated hMSCs showed high viability after 24 h post-encapsulation in dual-crosslinked hydrogels (MκCA, and MκCA-nSi) when stained for calcein AM (live cells) and ethidium homodimer (dead cells) **(Figure 3-7b)**. Both MkCA and MkCA-nSi, showed high cell viability after injection. Due to faster dissolution of κCA under physiological conditions, we performed cell studies only with dual crosslinked hydrogels.

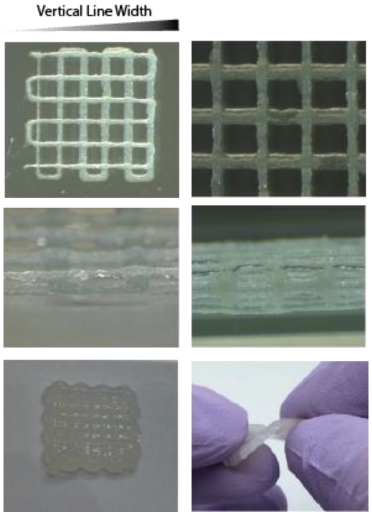

Figure 3-6. Lattices printed with and without cells were attainable. Control over fiber diameter could also be achieved. Fibers crossing struts of previous layers displayed minimal overhang, which facilitates printing of more layers above. UV crosslinked lattices were extremely durable and could be handled easily following printing.

The effect of nanosilicates on cell spreading was monitored over a period of 7 days. HMSCs encapsulated within both hydrogel networks showed circular morphology (**Figure 3-7c**), indicating that these compositions can be used for hMSC delivery for cartilage regeneration. Our results are consistent with earlier studies that have shown kCA-based hydrogels do not support cell spreading. Although, the addition of nanoparticles increases the mechanical stiffness of nanocomposite hydrogels, no significant change in cell morphology was observed. This is in contrast to earlier reported studies, where increase in mechanical stiffness of gelatin-based hydrogels, support cell spreading.[213, 220-221] The contradiction with other studies is due to the use of kCA, which is shown to be non-cell adhesive as the polysaccharide lacks any inherent cell-binding moieties. This morphological control may stimulate cell behavior as previous reports have demonstrated κCA-based hydrogels promote chondrogenic differentiation of stem cells.[222-223] The lack of membrane receptor binding sites (e.g. RGD), may limit cell growth on the hydrogel surface, as indicated by no notable increase in cell proliferation after 3 days of culture (**Figure 3-7d**). Cells placed within a 3D matrix, however, may still proliferate due to the 3D environment simulating native cartilage.

Over the course of the printing process, the bioink should maintain the spatial distribution of cells to ensure each printed layer incorporates the same concentration of cellular material to synthesize new matrix. An ink that lacks a sufficient viscosity will enable cell settling, in which case early printed layers will receive much greater concentrations of cells that later layers. To qualify the success of the 5%/8% MκCA-nSi bioink as a cell vehicle during printing, cell distribution and viability following printing were both examined. Microscopy of a single fiber and multilayered cylinder both demonstrated the ability of the bioink to maintain a homogeneous concentration of cells throughout the printing of the scaffold (**Figure 3-6e**). Additionally, the presence of cells within the bioink had no negative effects on the printability of the structure as printed cylinders could be easily handled following crosslinking. Cells that survived the printing and crosslinking process within printed cylinders were able to proliferate over a 4 week span, which indicated the ink composition provided a suitable environment for encapsulated cells. Future work will look to characterize the phenotype changes of these cells to demonstrate the bioactivity of these inks for cartilage regeneration.

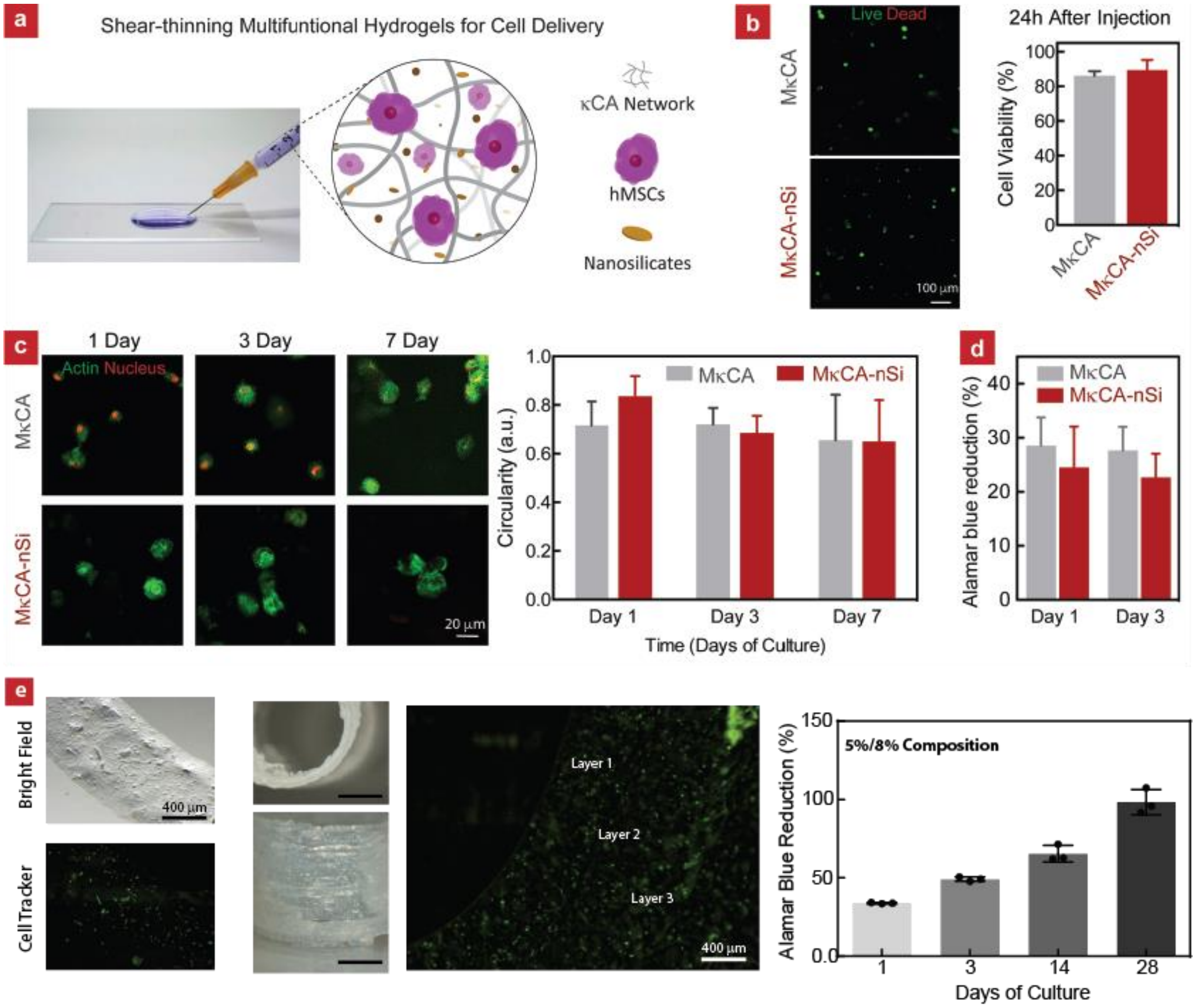

Figure 3-7. Biological evaluation of MκCA compositions. (a) MκCA and MκCA-nSi show higher viability of encapsulated hMSCs compared to κCA hydrogels. (b) Alamar blue assay showed no significant change in metabolic activity of encapsulated cells in MκCA and MκCA-nSi. (c) Encapsulated cells remained round after a week of culture, which provides 3D stimulation towards a chondrogenic phenotype. (d) hMSCs cultured on the surface of either MκCA or MκCA-nSi gels demonstrate little proliferation due to a lack of cell binding sites. (e) Cells printed within a 5%/8% MκCA-nSi ink maintain even distribution throughout the printing process. These cells also proliferate over the course of 4 weeks. Modified with permission from Thakur et al., 2016.

3.4 Conclusion

In this study, we developed a dual-crosslinked bioink system that was cytocompatible and maintained viability over the course of the printing process. The addition of 2D nanosilicates not only improved the mechanical durability of these scaffolds but also endows the system with shear-thinning characteristics. These nanocomposites provide advantageous rheological properties that can be exploited during printing to ensure a high degree of spatial control is achieved. Cells extruded within the nanocomposite were well distributed throughout printing layers and maintained viability and proliferative capabilities. Further, it is expected that these hydrogel bioinks will provide a bioactive environment for hMSCs to stimulate a chondrogenic phenotype due to the chemical and mechanical similarities of the polymer matrix to native cartilage in addition to the embedded bioactive nanosilicates.

4. CHEMICALLY EXFOLIATED MOS_2 FOR REGENERATIVE ENGINEERING[*]

4.1 Introduction

Two-dimensional (2D) materials have garnered widespread attention due to their unique physical and chemical properties stemming from their anisotropic, layered structure.[224-225] One such class of 2D materials with potential in a variety of applications is transition metal dichalcogenides (TMDs). While TMDs, like molybdenum disulfide (MoS_2), have been developed primarily for electronic applications as an alternative for transistor development, they have expanded into the biomedical domain.[226-230] Specifically, the generation of nanothin sheets via exfoliation processes of MoS_2 for transistor applications enables the formation of a direct bandgap and subsequent photoluminescent spectrum, which could be utilized as biosensors or photothermal therapies.[229, 231-234] From the MoS_2 atomic structure, the absence of dangling bonds from terminal sulfur atoms and potential surface modification render the nanomaterial stable in aqueous environments.[227, 231] This chemical stability can be exploited to introduce optically active nanosheets into biological environments containing human cells for biosensing, photo-stimulated drug delivery, or direct cell activation.

One mechanism to achieve the exfoliation of MoS_2 has been the chemical intercalation of lithium between crystal lattice sheets that are typically held in place by weak van der Waals forces.[231, 235]

---

[*] Unpublished data J.K. Carrow, A. Ramirez, M.K. Jaiswal, K.A. Singh, A.K. Gaharwar, "Chemically Exfoliated Molybdenum Disulfide for Photothermal Activation of Stem Cells" (*in prep*)

Following intercalation, exfoliation of MoS_2 nanosheets is achieved via exposure to water with multiple washing steps to remove potential cytotoxic materials.[236-237] Optimization of this chemical method has resulted in new protocols to reduce time and improve yield of low-layer nanosheets.[238] One disadvantage of these chemical methodologies, however, is the introduction of potentially cytotoxic materials that may initiate cell apoptosis through a variety of mechanisms due to insufficient washing following synthesis. As researchers continue to uncover the capabilities of MoS_2 nanomaterials within biomedicine and develop new fabrication protocols for TMDs with enhanced characteristics, a comprehensive evaluation of their interactions with human cells will be required.

The emergence of these new optically and electronically active nanomaterials has the potential to push regenerative medicine into undiscovered territory. Researchers continue to develop stimuli-responsive nanocomposites to provide spatiotemporal control of local cell responses.[239-240] For example, graphene, another electronically active 2D nanomaterial, has received wide attention for tissue engineering applications due to its ability to deliver a multitude of signals to surrounding cells.[241-242] The success of graphene as a 2D material in biomedical engineering has initiated investigations into many new layered materials.[243] While graphene oxides have provided suitable biocompatibility, heterogeneities in surface chemistry or functionalization can reduce functionality in biological systems, opening the door to TMDs.[244] TMDs, like MoS_2, hold similar promise to stimulate changes in cell behavior through their optoelectronic qualities and stability in aqueous media while demonstrating improved cytocompatibility.[245] Although some preliminary studies have investigated cellular compatibility of these materials, no studies thus far to our knowledge have explored their ability to stimulate tissue regeneration.[245-246]

Here we explore the dynamics of exfoliated MoS_2 nanosheet interactions with human mesenchymal stem cells (hMSCs) and the downstream behavioral changes as pertaining to tissue repair. By first examining 2D MoS_2 interplay with biomolecules in different media conditions, we evaluate the potential impact of protein-coated nanosheets on cellular internalization and behavior. We also exploit the inherent photothermal capabilities of exfoliated MoS_2 at near-infrared wavelengths (NIR)[227] to stimulate intracellular pathways and motivate hMSC differentiation. Traditional biological assays are performed to monitor global cellular signaling of hMSCs with sensitization of NIR demonstrated following exposure to MoS_2. Alone, these nanomaterials induce minimal changes to hMSC phenotype at cytocompatible concentrations. Furthermore, we identify the potential of a low-light intensity therapy for regenerative medicine.

4.2 Materials and Experimental/Procedure

4.2.1 MoS2 Synthesis. The bulk MoS_2 was chemically exfoliated following previously reported protocols.[238, 247-248] in a nitrogen filled glove-box, 200 mg of bulk MoS_2 powder (Alfa Aesar) in single-neck 100 mL round-bottom flask was degassed for couple of hours before adding 3 mL *n*-butyllithium (1.6 M in hexane, Sigma USA). The solution was then refluxed at 70 ˚C for 48h with continuous stirring. The reaction mixture was then cooled to room temperature and added with 20 mL dried hexane and filtered with nylon paper (pore size ~ 0.45µm). The excess *n*-butyllithium was washed and diluted with anhydrous hexane and safely transferred to a hazard labeled glass jar and sealed. The black precipitate was taken out from glove box and dispersed in 200 mL chilled water in a round-bottom flask and sonicated for an hour in an ice-cold water-bath to assist the exfoliation. To remove partially stacked layers from the suspension, the solution was centrifuged at 2 x 5000 rpm for 10 min per cycle followed by 2 x 8000 rpm for another 10 min per cycle. The dispersion was collected and stored at 4 ˚C for further experiments.

4.2.2 MoS2 Characterization. Transmission electron microscopy (TEM) was performed on a carbon grid at an accelerating voltage of 200 kV using a JEOL-JEM 2010 (Japan). Physical characterization of chemically exfoliated MoS_2 (ce-MoS_2) was investigated in the presence of physiological proteins via introduction of lysozyme or albumin. The zeta potential and hydrodynamic size of MoS_2-albumin solutions were measured with a Zetasizer Nano ZS (Malvern Instrument, U.K.) furnished with a He−Ne laser at 25°C. Changes in protein conformation after adding MoS_2 were evaluated using the ANS assay (8-anilino-1-naphthalenesulfonic acid).[249] Fluorescence was analyzed using a Tecan plate reader.

4.2.3 Stem Cell Culture. Human mesenchymal stem cells (hMSCs) were cultured under normal media conditions consisting of α-minimal essential media (alpha-MEM, Hyclone, GE Sciences) with 16.5% fetal bovine serum (Atlanta Biologicals, USA) and 1% penicillin/streptomycin (100 U/100 µg/mL, Gibco). After every 2-3 days, half of culture media was exchanged for fresh media. Cells were passaged with 0.5% trypsin-EDTA upon reaching confluency of ~70% and seeded at ~2500 cells/cm^2. All experiments were completed with cell populations under P5. Leaching studies were completed using both 2D exfoliated and bulk MoS_2 (1 mg/mL) placed within transwell membranes in a 24-well plate. As positive controls, solutions of ammonium molybdate salt in equivalent molar concentrations as the physical particles, which came out to 0.6 mg/mL, were placed onto transwell membranes. Cell health was monitored using an MTT assay (ATCC) at time points of 1 day and 7 days.

4.2.4 Cell Morphology. For actin staining, hMSCs were treated with MoS_2 for 24 hours, then fixed with 2.5% glutaraldehyde and permeabilized with 0.1% TritonX-100. Phalloidin stain was then added and samples were incubated for 1 hour at 37 °C. The stain was removed, washed with 1X PBS. Actin stained samples were imaged with a fluorescent inverted microscope. Cell area was quantified using ImageJ analysis software. Scanning electron microscopy of hMSCs treated with MoS_2 on glass cover slips were captured after sample (50 µg/mL) treatment for 1 hour. Cells were washed with PBS to remove weakly bound particles. Subsequently cells were fixed with 2.5% glutaraldehyde for 30 minutes at RT, washed again with PBS, and dehydrated using serial dilutions of ethanol and then by placing the slides in hexamethyldisilazane (HMDS) (James Cook University, Biological SEM sample preparation protocol). SEM images were taken on gold sputter-coated samples (JEOL NeoScope).

4.2.5 Cell Culture with NIR Stimulation. To evaluate changes in cell behavior with NIR exposure, cells were incubated under low intensity NIR LED light for two hours over a three hour period each day. Specifically, an LED array with a 3.4 W output power was placed 6 cm from the surface of the plate. The power density across the plate was measured to be around 20 mW/cm^2. Following exposure with or without $ceMoS_2$ (25 µg/mL), cell behavior was monitored through multiple studies. An alamarBlue assay was performed according to the manufacturer's protocol over the course of a week to measure proliferation. Further, changes in cell phenotype were explored using western blot for osteogenic markers, like ALP and Runx2. Specifically for Western Blot analysis, cells were cultured under the same media conditions as previous assays. Both intracellular and extracellular proteins were isolated by direct application of a boiling Laemmli Buffer (4% SDS, 20% glycerol, 10% 2-mercaptoethanol, 100 mM Tris HCl, and 0.2% bromophenol blue). Gel electrophoresis (Invitrogen, Mini Gel Tank) was performed on samples and protein bands were transferred (Invitrogen, iBlot 2) to a nitrocellulose membrane according to manufacture protocol. Membranes were blocked using 5% BSA in PBST (PBS + 0.1% Tween 20) for 30-60 minutes then processed (Invitrogen, iBind). β-actin, ALP, and p-MEK1/2, primary antibodies (ThermoFisher) and HRP conjugated secondary antibodies (Boster Bio) and incubation was performed per manufacture protocols. Blots were developed (SuperSignalTM West Pico PLUS Chemiluminescent Substrate, ThermoFisher) and imaged via LI-COR® 3600 C-Digit Blot Scanner. Protein bands were quantified with LI-COR software. The blots were then stripped and re-blocked with 5% BSA in PBST for further analysis.

Alternatively, high power NIR applications were also evaluated. hMSCs were cultured to a confluent monolayer in a 6-well plate in normal growth media. Prior to ceMoS$_2$ treatment, cells were starved in media lacking FBS for 2 hours. Cells were then placed back into normal growth media with a concentration of 100 μg/mL of MoS$_2$ for an incubation period of 3 hours. Cells were then washed multiple times with PBS and provided with new growth media. Control and treated cell populations were exposed to pulsed laser ($\lambda = 800$ nm) at ~340 mW/cm^2 for 7 minutes, with a 6.5 ms pixel dwell time spanning 256 x 256 pixels. Following NIR exposure, cells were incubated for 3 hours and then treated with a Calcein AM/Ethidium homodimer solution for 30 minutes to stain for viable and compromised cells. The zone of ablated cells was visualized using Nikon fluorescent microscope.

4.2.6 Statistical Analysis. Determination of statistical significance between multiple groups was completed via analysis of variance (ANOVA) with Tukey method. Significant p-values were considered <0.05 unless otherwise noted. All analysis was completed in GraphPad Prism (San Diego, CA).

4.3 Results and Discussion

4.3.1 Synthesis and Chemical Analysis of Exfoliated MoS_2 Nanosheets

Bulk MoS_2 is composed of atomically thin S-Mo-S sheets stacked by short-range Van der Waals forces. The phase and morphology of ceMoS_2 nanosheets were characterized by AFM, TEM, XRD, XPS and PL spectra techniques. AFM revealed layered sheets were 2 – 7 µm in diameter with thicknesses around 3 nm (**Figure 4-1a**). The theoretical calculation suggests S-Mo-S atomic lattice thickness to be about 0.65 nm which indicates the selected flake in the magnified image contain 3-5 sheets of monolayer MoS_2.[250] Transmission electron microscopy indicated smooth layer topography and defined nanosheet structure. Additionally, the selected area electron diffraction (SAED) pattern confirmed the formation of 1T phase after lithium intercalation assisted exfoliation which was further corroborated by X-ray diffraction (**Figure 4-1b**).

The binding energies (BE) for molybdenum and sulfur core level electrons determined by X-ray photoelectron spectra (XPS, **Figure 4-1c**) revealed the crystallographic phases associated with bulk MoS_2 transformed to a few layers. The BE for Mo3d doublets ($3d_{5/2}$ and $3d_{3/2}$) gave rise to signals at 228.5 and 231.7 eV for bulk MoS_2 which, after exfoliation, shifted to 228.2 and 231.5 eV, respectively, indicating the 2H to 1T phase transformation. Similarly, the BE for S2p doublets ($2p_{3/2}$ and $2p_{1/3}$) appeared at 161.4 and 162.6 eV which correlate with the 2H phase while 1T phase signals appeared at 161.1 and 162.3 eV, respectively, following exfoliation. Raman spectroscopy

(Horiba Inc, green laser 532 nm) was further used to ascertain the vibrational modes associated with the MoS_2 lattices for both bulk and exfoliated sheets (**Figure 4-1d**).

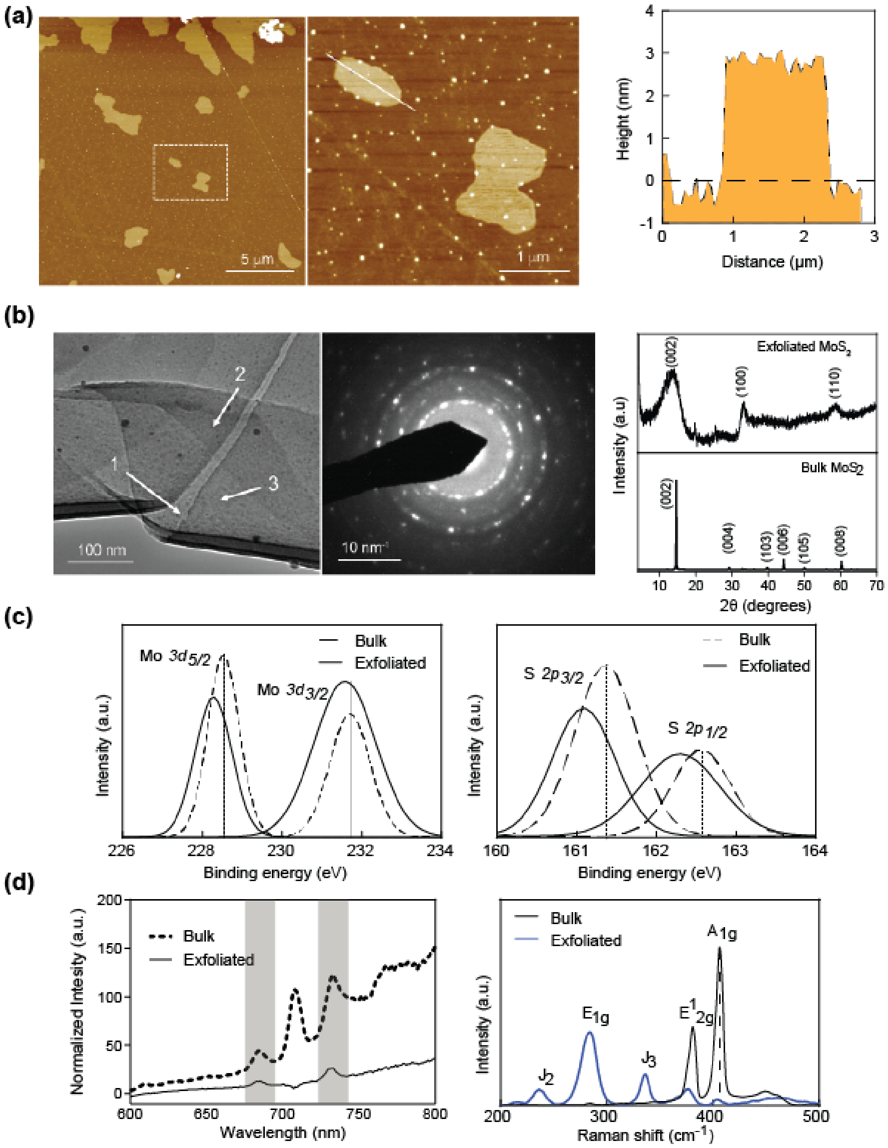

Figure 4-1. Phyicochemical characterization of chemically exfoliate MoS_2 nanosheets. (a) Atomic force microscopy measure micron-sized nanosheets with nanometer thickness, confirming 2D shape. (b) TEM images of ultrathin MoS_2 sheets displayed overlapping layers; each individual layer is numbered. Further, XRD corroborated the formation of the 1T phase following lithium intercalation. (c) Crystallographic transformations from bulk to exfoliated MoS_2 were monitored with XPS analysis with shifts from 2H to 1T phases observed. (d) Raman spectroscopy and photoluminescent measurements likewise indicated structural modifications had occurred seen through changes in vibrational energy bands and luminescent intensity.

As expected the two characteristic modes, E^1_{2g} corresponding to in-plane vibrations of sulfur atoms with respect to molybdenum and A_{1g} corresponding to out-of-plane vibration of sulfur atoms gave rise prominent signals at 380.8 and 406.5 cm^{-1} respectively in bulk form. Upon exfoliation, the A_{1g} band witnessed a downward shift to about 403.9 while E^1_{2g} shifted to 376.5 cm^{-1} respectively. It is interesting to note the relative intensities of both the bands in bulk as well as exfoliated forms. The in-plane vibration (E^1_{2g}) rose significantly in comparison to out-of-plane (A_{1g}) after layer exfoliation which corroborates the fact that due to layers exfoliation more sulfur atoms are free to contribute to the signal, while A1g for which major contributions come from edges remained same. Furthermore, due to phase change from 2H to 1T, additional vibrational bands such as E_{1g}, J_2 and J_3 were also observed for exfoliated MoS_2 sample.[251] Photoluminescent intensity decreased for exfoliated samples as the material density within 3D space was reduced, corroborating successful transition to a 2D nanosheet architecture.

4.3.2 MoS_2 Stability in Aqueous Environments

Following chemical intercalation, aqueous stability of the nanosheets was evaluated in multiple media conditions. While these nanosheets are typically dried or easily dispersed in deionized water (diH_2O) for characterization, cell studies require a regulated ionic environment to ensure cell survival. Zeta-potential was monitored of $ceMoS_2$ in both diH_2O and phosphate buffered saline (PBS) with and without albumin to evaluate stability in relevant media conditions (**Figure 4-2a**). Nanosheets were stable in both aqueous environments with zeta-potential measurements of -32.7±1.1 mV and -29.2±1.7 mV for diH_2O and PBS, respectively. After the addition of protein, however, the surface of shear, or the interface of bound charges and diffuse layer, is shifted further from the surface, effectively reducing the zeta-potential. This phenomenon was observed as the zeta-potential significantly dropped to -17.3±0.8 mV and -14.0±0.6 mV, respectively. This indicated that while biomolecules were strongly interacting with the nanomaterial surface, the repulsive forces between MoS_2 nanosheets are reduced, leading to eventual flocculation at longer timescales.

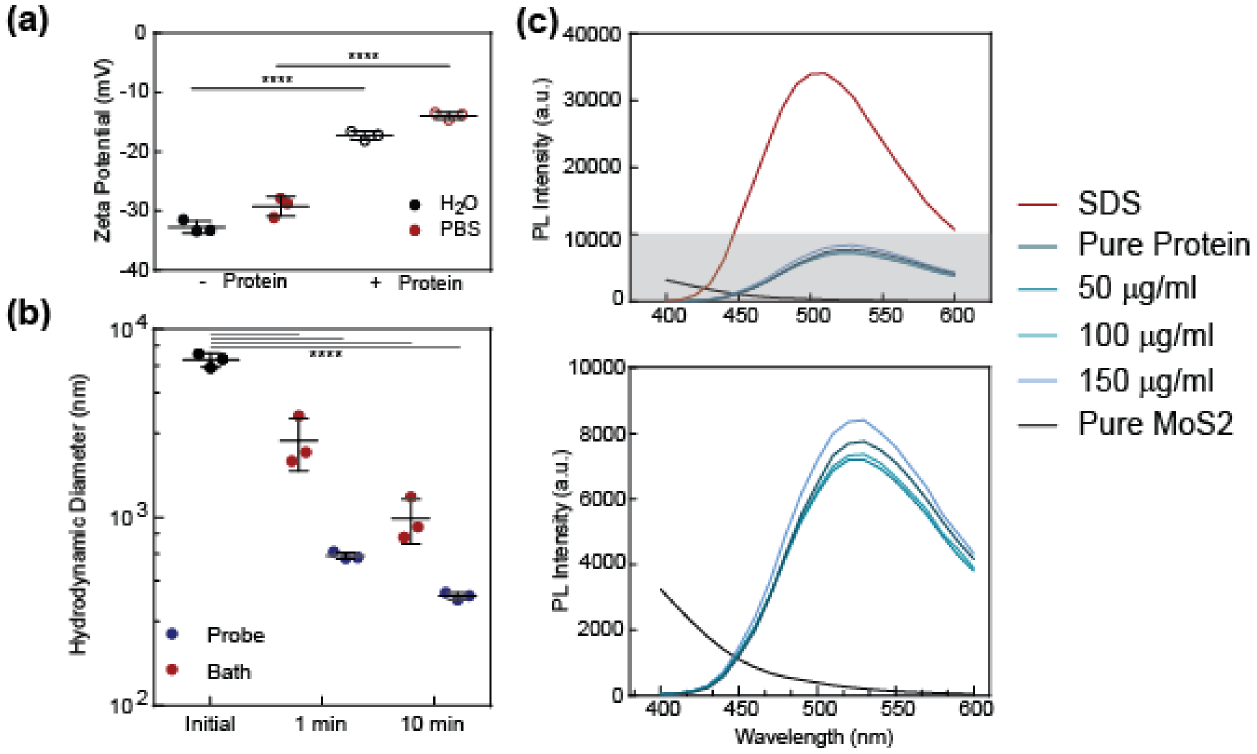

Figure 4-2. Evaluation of ceMoS$_2$ in relevant biological aqueous environments. (a) Dispersions of ceMoS$_2$ sheets were stable prior to the addition of protein (albumin) with a subsequent decrease in zeta potential magnitude, indicating a reduction of electrostatic stability of the particles. (b) Sonication utilized to improve dispersion of the MoS$_2$ resulted in a decrease in hydrodynamic diameter, with probe sonication imparting greater disruptive force than bath sonication over both time points. (c) ANS assay was completed over a range of ceMoS$_2$ concentrations to evaluate effects on protein structure following binding to the nanosheet surface. Compared to the positive control (SDS), the sheets imparted little effect on protein structure and would enable functional binding between coated proteins within the corona and cell membrane.

To improve nanosheet dispersions within these aqueous media environments, bath or probe sonication can be utilized. These mechanical methods to reduce interactions between sheets may also reduce the effective sheet size. To investigate the effects of type and duration of sonication, DLS was utilized on aqueous dispersions of ceMoS_2 (**Figure 4-2b**). Samples lacking sonication displayed relatively large particles size to hMSCs with an average hydrodynamic diameter of 6.86±0.57 µm. Following a minute sonication with a bath or probe sonicator, there was a significant reduction in size to 2.56±0.78 µm and 0.62±0.03 µm, respectively. Extending to 10 minutes further reduced the hydrodynamic size in both environments to 0.99±0.26 µm in the bath and 0.38±0.02 µm with the probe. There is a significant reduction in physical size within 1 minute of sonication which has important ramifications for sample preparation prior to cellular exposure. Specifically, even a brief sonication to improve dispersions of the nanosheets may result in physical changes to the MoS_2. Smaller MoS_2 nanosheet sizes will affect binding dynamics to proteins in the aqueous environment and subsequently to the cell membrane. Based on previous studies examining size-dependent mechanisms for endocytosis, nanosheets remaining after 1 minute of sonication would be outside of the size range for effective internalization.[252] Nanosheets bound to the membrane, however, can still be utilized for external NIR stimulation.

Another consideration is that of the protein corona as protein arrangement on the nanomaterial surface will dictate binding to cell membrane receptors and drive stimulation of intracellular pathways. To evaluate changes in protein conformation, an 8-anilinonapthalene-1-sulfonic acid (ANS) assay was utilized (**Figure 4-2c**). Compared to a known disruptor of protein structure, sodium dodecyl sulfate (SDS), binding of a model protein with positive charge at buffered pH, lysozyme (isoelectric point – 11.35), to MoS_2 displayed minimal change. Furthermore, increasing the ceMoS_2 concentration from 50 – 150 µg/mL had no significant impact on fluorescent signal, indicating maintenance of native structure over a range of relevant concentrations. The micron size in two dimensions of the ceMoS$_2$ lends itself to binding of solubilized proteins; furthermore, proteins with native structure intact will enable clustering of receptors on the cell membrane and stimulate downstream intracellular pathways.[253-254]

4.3.3 Concentration Dependent Cytcompatibility

To determine optimal concentrations for future cell studies, cytocompatibility of MoS$_2$ was evaluated using Alamar Blue metabolic assay. Results indicated that cytotoxic effects of MoS$_2$ were not evident until concentrations exceeding 100 µg/mL after seven days of culture (**Figure 4-3**). These results were corroborated with cell area measurements. Concentrations up to 100 µg/mL showed little change to cell morphology, while large concentrations resulted in the reduction of cell area as apoptotic processes inhibited the synthesis of cytoskeletal components. These results provide insight as to potential therapeutic concentrations for subsequent photothermal activation experiments. We selected concentrations between 25 - 100 µg/mL to uncover specific changes in hMSC behavior following nanomaterial introduction and NIR activation.

Due to the electrostatic forces of ceMoS$_2$ within aqueous media, particles are expected to maintain colloidal stability while enabling significant interactions with solubilized biomolecules and consequently, the cell interface. The average size of these nanosheets, with minimal sonication, limit their uptake within hMSCs due to thermodynamic constraints of membrane tension, thereby confining these nanomaterials to the cell surface.[254-255] Maximizing contact with the cell membrane not only enables enhanced immobilization of MoS_2, but also endows the local environment with stimuli-responsiveness towards NIR light sources.

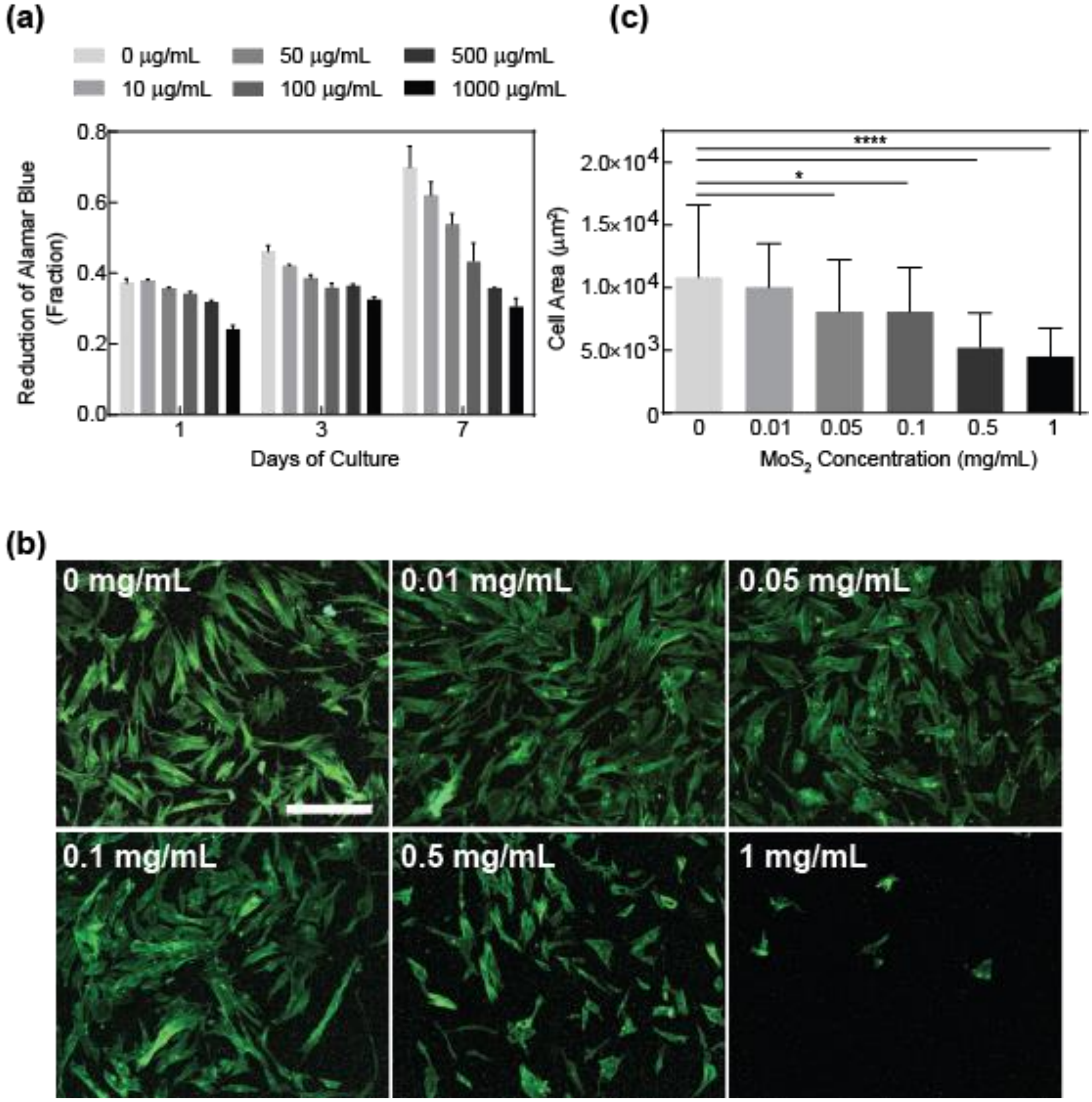

Figure 4-3. In vitro effects of $ceMoS_2$. Nanosheets displayed cytocompatibility up to 100 µg/mL, as seen with alamarBlue (a) and morphological analysis (b,c). As concentrations increased, cell morphology was likewise affected as cells limited their cytoskeletal expansion, with a significant decrease occurring upon reaching a concentration of 50-100 µg/mL. (Scale bar 300 µm).

Bright field imaging indicated substantial binding to cell surfaces with a 50 µg/mL treatment concentration (**Figure 4-4a**). Electron microscopy was used to evaluate the extent of membrane coating by these nanomaterials following introduction into the media (**Figure 4-4b, c**). Interestingly, images of the cell body depicted homogeneous coverage of submicron sized material across the membrane. Untreated cells presented no such phenomenon, ruling out sample preparation as a cause of the speckle formation. One hypothesis for the smaller than expected appearance of the materials could be the result of sonication. The reduced size of particles may facilitate binding to the cell membrane through a reduction in surface energy. Furthermore, larger particles remaining in solution may have been less thoroughly bound and washed away during the sample preparation process. The extent of coverage of ceMoS_2 on the cell surface is expected to improve the likelihood of photothermal activation of cellular pathways.

While localization of these nanomaterials on the cell surface enable future stimulation with NIR sources, long-term exposure to aqueous environments can initiate the dissociation and release of chemical species. Specifically, investigations into MoS_2 persistence within cell culture media have displayed sensitivity to oxidative conditions with ~30% dissolution occurring after one week.[256] Chemically exfoliated MoS_2 likewise demonstrated increased dissociation rates relative to ultrasonically exfoliated materials. Likewise, these results indicated that the concentrations utilized in our studies, even with 100% dissolution, would not be expected to induce cell death.[256] To further examine a potential mechanism of cytotoxicity of the ceMoS_2, dissociated species were compared to a multiple concentrations of solubilized Mo. Briefly, ceMoS_2 and bulk MoS_2 were placed within transwell membranes at known cytotoxic concentrations (1 mg/mL). Mo was introduced at molar equivalences of 100% dissociation of ceMoS_2 nanosheets. At solubilized Mo concentrations around 6 mM, a slight decrease in cell viability would be expected.[256] After 24 hours of exposure, a 35% decrease in metabolic activity was observed for cells treated with bulk MoS_2, with a 15% decrease noted for both $ceMoS_2$ and solubilized Mo (**Figure C.1**).

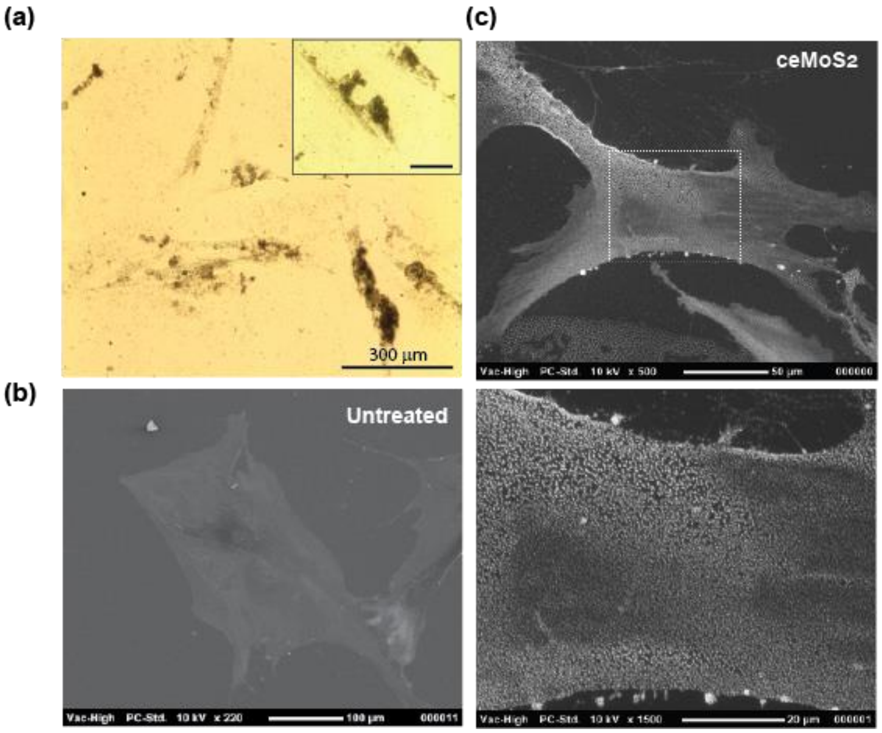

Figure 4-4. Images of cells with $ceMoS_2$ treatment. (a) Bright field microscopy images displayed coating on cell membranes of cells to varying degrees, with clusters of nanosheets occurring if not fully dispersed due to protein and ion interactions. (b, c) SEM of control cells show no effects on cell surface while MoS_2-treated cells have a robust coating of sub-micron materials. (Insert scale bar 100 µm).

By limiting direct exposure of $ceMoS_2$ to hMSCs, cell viability was somewhat improved compared to cell morphology studies. Likewise, solubilized Mo displayed limiting impact on cell viability. In combination, these results may indicate that a decrease in hMSC viability and function is attributed to stresses placed onto cells by the physical binding and direct interactions of ceMoS$_2$ rather than chemical dissociation. Further studies will be needed to evaluate the kinetics of ceMoS$_2$ dissociation into its ion components under biological conditions.

4.3.4 NIR-mediated Evaluation of Cell Behavior

Considering ceMoS$_2$ alone did not trigger any noticeable changes in hMSCs until reaching cytotoxic concentrations, low intensity NIR stimulation was applied as a means to induce behavioral changes. The application of NIR light via a LED source in conjunction with ceMoS$_2$ was explored for potential therapeutic use (**Figure 4-5a**). Prior to introducing the exfoliated nanosheets within the local cell environment, the NIR responsiveness was evaluated to ensure photothermal effects could be utilized for future cell stimulation. To evaluate the generation of heat following an application of NIR light to a solution of ceMoS$_2$, temperature was monitored over the course of 10 minutes using a thermocouple as well as IR imaging (**Figure 4-5b**). Two 500 µL solutions, one containing 2 mg/mL of ceMoS$_2$ and one of pure diH$_2$O, were subjected to an NIR laser used in continuous wave mode at multiple intensities. Upon subjecting the ceMoS$_2$ to NIR light, the temperature of the solution increased by ~5.5 °C and ~3.5 °C for the high and low power trials, respectively. For the pure water, the temperature remained stable around room temperature throughout the entire exposure time. This demonstrated that photothermal effects could be expected following NIR exposure to ceMoS$_2$ treated cells. While the low power intensity, which mimicked an upper limit of LED arrays used in future studies, increased the temperature of the solution, we hypothesize that cells would be stimulated by fluctuations constrained to the cell membrane rather than a broadly increasing media temperature considering cytocompatible ceMoS$_2$ concentrations are a factor of 20 to 80 times lower.

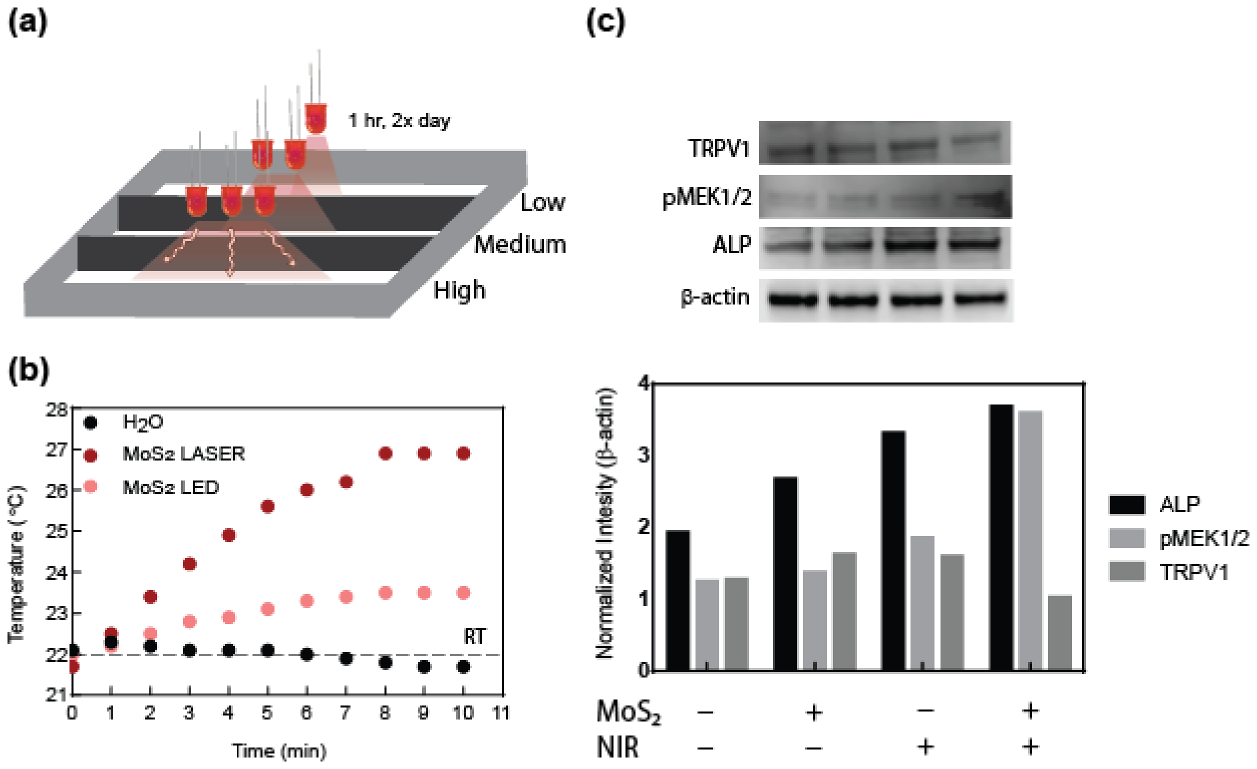

Figure 4-5. Low intensity NIR exposure of ceMoS$_2$ treated cells to modulate behavior. (a) Schematic of setup with multiple LED arrays placed within the lid of a plastic enclosure to explore varying degrees of LED intensity to impact cell phenotype. Each LED intensity region was separated with light impenetrable dividers to minimize scattering effects. (b) The combination of NIR and ceMoS$_2$ can modulate media temperature over time. Decreasing light intensity to that found within the highest power LED array used for all *in vitro* experiments correlated with a reduction in temperature increases. (c) Western blot analysis indicated an increase in protein synthesis for samples receiving NIR exposure, with the greatest correlating to those with both ceMoS$_2$ and NIR light.

Following daily NIR exposure with and without ceMoS$_2$, cultured hMSCs and synthesized proteins were collected for western blot analysis to characterize any changes in cell behavior. A protein within the receptor activated MAPK or ERK1/2 cascade (pMEK1/2) and early osteogenic marker (ALP) were selected as potential targets to track phenotype changes in the hMSCs. Specifically, activation of the ERK1/2 pathway may indicate the presence of photothermal effects at the membrane, while ALP has been implicated in downstream activation of this MAPK cascade in osteoblasts.[257] Heat Shock Protein 70 (HSP70) is also involved in both osteogenic and chondrogenic differentiation, while also impacting downstream MAPK signaling.[258-259] Therefore, HSP70 may also be a potential target of photothermal activation and requires further investigation. Cells receiving both ceMoS$_2$ and NIR exposure displayed the highest synthesis of both proteins of interest (**Figure 4-5c**). As expected, ceMoS$_2$ alone did not induce any phenotypic changes. Interestingly, NIR exposure without a photothermal inductive material, like MoS$_2$, provided a slight increase in protein translation. Interestingly, a transient receptor cation ion channel subfamily V (TRPV1) resulted in decrease synthesis after one week of NIR exposure with ceMoS$_2$ treated hMSCs. While this receptor is implicated in heat responses to cells, a decrease was noted. Previous studies have indicated the potential of activated heat shock proteins (HSPs), specifically HSP70, to have an inhibitory effect on TRPV1. Additionally, HSP70 has been observed to initiate and regulate regenerative responses for both osteogenic and chondrogenic lineages.[260-261] More studies are required to evaluate the potential of NIR light as an inductive mechanism for hMSCs and the role of HSP70 as a mediator of this response.

4.3.5 Exposure for Photothermal Ablation

While LEDs provided low intensity stimulation of nanosheets bound to the cell membrane, a laser applied across the cell area would provide enhanced NIR absorption. Increasing light intensity delivered to ceMoS$_2$ treated hMSCs is expected to induce photothermal ablation of the local cell population.[262-264] Following treatment of the nanosheets, cells clearly displayed a sensitization toward NIR stimulation as cells within the rastered area of the laser were locally ablated. The apparent zone in the images was consistent with the predicted distance covered by the laser (280 µm x 280 µm) (**Figure 4-6**). Furthermore, dead cells following laser treatment can be washed away. These 2D voids on the seeding surface can be replaced with a new cell population for spatially controlled tissue patterning to investigate interactions between various cell types. As indicated from western blot data, cells treated with ceMoS$_2$ lacking NIR exposure show minimal changes to cell phenotype; therefore, cells outside the rastered zone would be expected to maintain normal cell function.

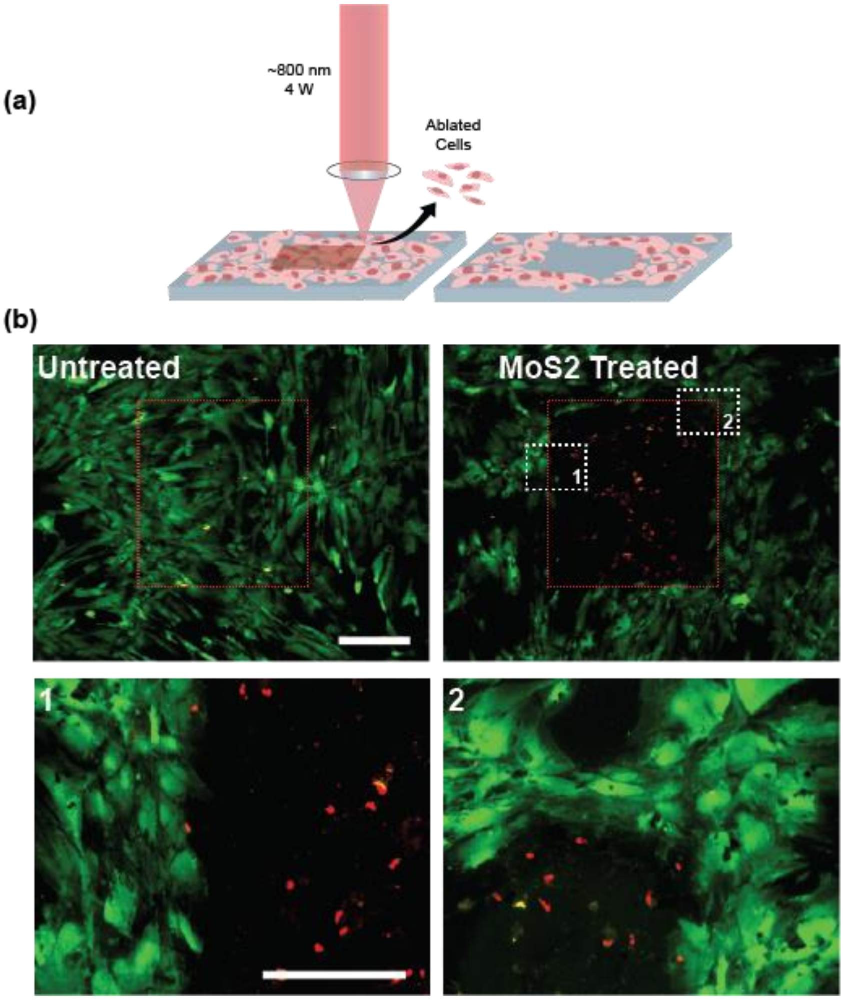

Figure 4-6. High intensity NIR exposure for local ablation of cells. (a) Schematic of 2D monolayer ablation of cultured cells through selective exposure of high intensity NIR light on ceMoS$_2$ treated cells. (b) Untreated cells remain viable even after exposure to NIR light, while cells pretreated with nanosheets were photothermally ablated with a high degree of spatial control over the zone of apoptosis. (Scale bar 300 µm)

4.4 Conclusion

Here we have evaluated the bioengineering potential of a chemically exfoliated transition metal dichalcogenide, specifically molybdenum disulfide. The 2D structure of this nanomaterial enables stable interactions with biological molecules that can facilitate subsequent binding with the cell membrane. Once localized to the cell surface, the ceMoS$_2$ nanosheets can be exploited with NIR light to generate a thermal stimulation. At high enough intensities, the light may be utilized to achieve a high degree of spatial control over cell death or release of biomolecules. Further, the combination of ceMoS$_2$ and low intensity NIR light may stimulate differentiation pathways within hMSCs, providing a novel route of stem cell induction. Future studies will explore the specific genetic mechanisms of this induction as well as optimal combinations of nanosheet combination and NIR exposure length and duration for a more robust cell response. This photothermal system provides a temporal mechanism over phenotype changes in treated stem cell populations and provides an exciting avenue for regenerative applications.

5. TRANSITION METAL DICHALCOGENIDE NANOCOMPOSITE FOR REGENRATIVE ENGINEERING[*]

5.1 Introduction

Two-dimensional (2D) transition metal dichalcogenides (TMD), such as molybdenum disulfide (MoS_2), have gained unprecedented attention due to their unique atomically thin, layered, and well-defined structure that provide distinctive physical and chemical properties compared to bulk 3D counterparts.[228, 265-267] 2D TMDs have high electron density and facile formation of lattice atomic defects, enabling researchers to explore a wide-variety of applications in nanoelectronics[229, 268], energy[269-270], optics, sensors[228], catalysis[271], photothermal agents for cancer treatments[227, 272], and biomedical research[224]. Despite interesting properties of 2D TMDs, they are not extensively investigated for regenerative medicine due to an inability to incorporate within biomaterial scaffolds.

Here, we demonstrate a new approach of chemically conjugating 2D MoS_2 with polymeric binder to form high-water content gels. This new approach of chemical conjugation between 2D nanomaterials and polymeric chains utilizes the planar and edge atomic defects[225] available on these nanomaterials. This will generate a chemically-reinforced polymeric network thereby promoting the formation of mechanically resilient networks. The role of the atomic defects present on the lattice plane of 2D MoS_2 to serve as an efficient catalyst in electrochemical production of hydrogen has been well studied.[271, 273] These atomic defects are mostly due to sulfur vacancies and

---

[*] Reprinted with permission from, "Jaiswal, M.K.; Carrow, J.K.; Gentry, J.L.; Gupta, J.; Altangerel, N.; Scully, M.; Gaharwar, A.K. Vacancy-driven gelation using defect-rich nanoassemblies of 2D transition metal dichalcogenides and polymeric binder for biomedical applications. *Advanced Materials*, 2017. Copyright 2017 John Wiley & Sons, Inc."

can act as an active center for catalysis. Molybdenum (Mo) is thiophilic[268] and Sulphur (S) has a strong affinity toward forming disulfide bond[274], together they offer facile binding centers for thiolated-molecules. Some recent works have demonstrated this ability of the 2D MoS_2 nanosheets *via* thiol-activated ligand conjugation.[226, 275-277] We intend to exploit these vacancy-driven '*active centers*' to conjugate macromolecules with thiol-activated terminal such as PEG-SH *via* chemisorption to form elastomeric and robust gel.

5.2 Materials and Methods

5.2.1 Materials and Synthesis: Defect-rich MoS_2 nanoflowers were synthesized by dissolving Hexaammonium heptamolybdate tetrahydrate, $(NH_4)_6{\cdot}Mo_7O_{24}{\cdot}4H_2O$ and Thiourea, NH_2CSNH_2 (procured from Alfa Aesar) in 35 mL of deionized water. This solution was then autoclaved at 220°C for 18h [1]. After the solution cooled down to room temperature, the MoS_2 was washed with water and ethanol several times to remove unreacted reagents and other impurities. To synthesize all the compositions of MoS_2 nanoassemblies (1:1, 1:2, 1:4, and 1:6) the molar ratios of the reagents were accordingly varied, (e.g. 1:1 MoS_2 was synthesized using 1 mmol of $(NH_4)_6{\cdot}Mo_7O_{24}{\cdot}4H_2O$ and 7 mmol of thiourea).

The hydrogels were prepared by dissolving tetra-arm PEG-SH (Mol. wt. 20,000; procured from Jenchem Technology, China) in a dispersion of MoS2 nanoassemblies (1:4) in deionized water. The prepolymer solution of MoS2 and polymer binder was sonicated for 3h to ensure homogeneous mixture was obtained. The solution was then stirred magnetically until it turned viscous and eventually gel was obtained. Since the gelation time was directly linked with the available number of vacancy sites in MoS2 lattices, hence the duration can easily be altered from a week of stirring (for significantly low number of vacancies e.g. 1:1) to few hours (for significantly higher vacancies e.g. 1:4) and vice-versa. Furthermore, the solution can then be injected into a desired shaped-mold and allow to gel. The prepared gel is further removed from the mold and soaked in water/PBS to remove any unreacted reagents.

5.2.2 Calculation of active sites by cyclic voltammetry*:* Cyclic voltagram was performed for the calculation of active sites in the samples following the standard protocol [1]. For this study, a three-electrode configuration was used. During the measurements, a glassy carbon electrode (GCE, diameter φ = 2 mm), a platinum wire, and an Ag/AgCl (KCl saturated) electrode were used as the working, the auxiliary and the reference electrode, respectively. Prior, experiments, the electrodes were properly cleaned by polishing with different Alpha-alumina powder (1.0 and 0.3 micron and 0.05 micron provided by *CH Instruments*) suspended in ultrapure water on a Nylon polishing pad (*CH Instruments*). After polishing with different alumina powder, the electrodes were thoroughly rinsed with water. The electrodes were further sonicated with water and ethanol for 5 min to make them clean properly. Electrochemical measurements were carried out using an electrochemical workstation (Model No. CHI-660D instrument).

All MoS_2 samples (labelled 1:1, 1:2, 1:4, 1:6) were then deposited on the glassy carbon electrode as working electrode. Typically, 10 mg mL^{-1} of each sample was dispersed in ultrapure water and 50 µg of the sample was deposited on the GCE and dried it at room temperature. The active sites were calculated by taking the absolute components of voltammetric charges (cathodic and anodic) from the Cyclic Voltametry scan between -0.2 and 0.6 V (vs. RHE) with 50 $mV.s^{-1}$ scan rate in phosphate buffer solution (pH~7.0) and shown in Fig. S1. By considering one electron redox process was occurred during the reaction; therefore, the total charges were divided by two. The number of active sites was obtained for the sample deposited on the electrode by using the following equation.

Number of active sites (mol/g), n = Q/2F

F: Faraday constant (C mol^{-1}); Q: Voltammetric charges

5.2.3 Material Characterization: For morphological imaging of the MoS_2 nanoassemblies and transverse section of the freeze-dried hydrogels, FEI Quanta 600 field emission-scanning electron microscopy (FE-SEM) was used. Typically, the operational voltage was maintained at 20 keV with secondary electron mode selected. Further for elemental mapping to confirm the presence of molybdenum and sulfur in the gel samples, software controlled EDS (Energy-dispersive X-ray spectra) detector was used and particular area was selected to map the presence elements and record binding energy spectra. Prior imaging samples were exposed to Pt/Pd plasma coating of the thickness of approx. 8 nm to enhance surface conductivity.

For transmission electron microscopy (TEM) images and selected area electron diffraction (SAED), JEOL 2010 operated at 200 keV was used. For sample preparation, aqueous dispersion of MoS2 samples were drop-casted and air-dried on copper grid (procured from Ted Pella Inc.).

The crystallographic phase of defect-rich MoS_2 nanoassemblies were confirmed by X-ray powder diffraction (Bruker D8 advanced) using copper source (wavelength ~ 1.54 Å). The data were recorded from 5 to 70 degrees and obtained peaks were indexed using JCPDS card No. 73-1508. The characteristic peak (002) was used to calculate crystallite size (D) using Scherrer equation given as below:

$$D = \frac{K\,\lambda}{\beta \cos\theta}$$

Where K is shape factor (approx. 0.94), λ is X-ray wavelength, β is line broadening at full withd half maxima (FWHM), and θ is the Bragg angle.

Raman spectra is strong tool to confirm the phase composition of the nanoassemblies as well as their chemical conjugation to the polymer binders. Solid powder samples of MoS_2 nanoassemblies (1:1 to 1:6) were placed on glass slides and were excited by 532 nm green laser to obtain Raman spectra (LabRam HR confocal Raman microscope, Horiba Inc. Japan). In case of gel, the Raman spectra were recorded between 250 to 2850 cm^{-1} after placing a gel piece onto the glass slide and excited by the laser beam.

The confirmation of 2H phase of the synthesized defect-rich MoS_2 nanoassemblies and their conjugation with polymer binder obtained from Raman spectra were further corroborated with X-ray photoelectron spectroscopy (XPS) (Omicron XPS system with Argus detector). The binding energies (B.E.) for Mo (*3d*) and S (*2p*) for MoS_2 samples along with that of carbon (C *1s*) for nanocomposites were recorded. The raw data were further processed and deconvoluted by CasaXPS multiple peak fit software version 2.3.15 and indexed using standard library.

Further to determine the characteristic absorbance peaks of defect-rich MoS2, aqueous suspension of MoS_2 nanoassemblies were subjected to UV-visible spectrophotometer (Perkin Elmer Inc.) and the date were recorded from 300 to 800 nm. The presence of three peaks at approx. 470, 622, 668 nm confirmed the formation of dominant 2H phase. In order to determine the vacancy induced photoluminescence (PL) intensity of the defect-rich MoS2 samples (1:1 to 1:6), aqueous dispersions were excited at 470 nm and room-temperature emission spectra were recorded from 550 to 700 nm using Spectrofluorometer (Zeiss Inc.) equipped with xenon arc lamp.

The gelation kinetics, viscoelastic properties, stress relaxation and stress/frequency sweeps of the prepolymer solution/gel samples were analyzed using oscillatory stress controlled rheometer (Anton Paar MCR 301) equipped with 1cm diameter geometry and 2mm gap. The uniaxial compression tests were performed on the cylindrical samples (6mm×2 mm) at a strain rate of 1 mm/min using (Admet eXpert 7600 testing machine). The compressive modulus was calculated from the slope in the toe region corresponding to 0.10–0.20 strain in engineering stress–strain curve (force divided by original cross-sectional area).

5.2.4 In vitro Assay: Murine derived preosteoblasts (NIH MC3T3 E1−4, ATCC, USA) were cultured in normal growth media (Alpha MEM, Life Technologies, USA), supplemented with 10% FBS (Life Technologies, USA) and 1% penicillin/streptomycin (100 U/100 µg/mL; Life Technologies, USA) at 37 °C with 5% CO_2. Nanoassembly uptake was monitored with bright field microscopy following 3h treatment with a 100 µg/mL solution. Metabolic activity was measured using MTT assay following manufacturer’s protocol. Briefly, cells cultured in a 24-well plate were treated with a concentration sweep of 1:4 MoS_2 nanoassemblies, washed after 24h with PBS, and cultured in new media with MTT reagent. Newly formed formazan crystals were dissolved in a 1:1 solution of DMSO:IPA and then measured on a spectrophotometer. Cell cycle analysis was performed on cells cultured on tissue cultured polystyrene. DNA signal (FL2A channel) was measured using the BD Accuri C6 Flow Cytometer and propidium iodine (PI) stain. Following initial seeding, MC3T3’s were starved for 24 h to synchronize cell populations and treated with a concentration sweep of 1:4 MoS_2 nanoassemblies. Cells were trypsinized after 24 h of treatment and fixed in cold 70% ethanol. Cell pellets were formed and washed in PBS, followed by incubation in a PI staining solution containing RNase at 37 °C for 30 min. Cells were stored at 4 °C until analysis. Cell populations were initially selected based on forward scatter/side scatter profiles, with subsequent gating placed on fluorescent signal plots to select individual stages throughout the cell cycle. Gates remained consistent throughout measurement of different concentrations. For 3D encapsulation, the nanocomposite solutions were prepared in control media and placed in a sonicating bath until gelation was initiated as determined by rheology. Solutions were then used to resuspend cells for encapsulation, where gels (8 mm diameter, 500 µm thick) were enabled to form in a 12-well plate and then covered in media. For monitoring cell viability after 48 h, a prepared Live/Dead assay reagent from Calcein AM and Ethidium Homodimer (Santa Cruz Biotechnology, Inc., USA) were added to the nanocomposites and incubated for 30 min at 37 °C. The samples were washed with PBS thrice and imaged using an epifluorescence microscope (TE2000-S, Nikon, USA).

5.3 Results and Discussion

5.3.1 Nanoassembly Characterization

In 2D MoS_2, molybdenum occupies a trigonal prismatic (Mo^{IV}) coordination and bound to six sulfide ligands. Sulfur occupies a pyramidal (S^{2-}) location and is coordinated with three molybdenum atoms. This results in the formation of a layered structure with interconnected trigonal prisms, wherein molybdenum atoms are sandwiched between layers of sulfur atoms. Therefore, pristine MoS_2 structures provide minimum planar defects and lack sufficient "*active centers*" for conjugation with polymeric molecules. To overcome this issue, we synthesized defect-rich MoS_2 by constraining the growth of the lattice to include atomic defects. By modulating the precursor mole ratios of molybdenum:sulfur (1:1 to 1:2, 1:4, and 1:6), a series of nanosheets with various degrees of defects were obtained (**Figure 5-1a**). These 2D nanosheets assembles to form co-centric, well-segregated, hierarchical structures which resemble to a *"flower"* wherein the nanosheet flakes form *"petals"*.[270, 278-279] The formation of MoS_2 nanoassemblies occurs mainly due to Ostwald ripening of flakes grown during hydrothermal process at higher temperature.[272] Due to the rippled morphology, MoS_2 nanosheets remain unstacked and provide larger surface area and easy access to planar defects.

The aqueous stability of MoS_2 nanoassemblies was investigated by zeta potential (ς) measurements. Nanoassemblies were stable in water with ς in the range of -35mV (±10%). No significant difference in zeta potential was observed due to change in Mo:S ratios; however, increase in thiourea content resulted in enhanced aqueous stability. The hierarchical nanoassemblies were analyzed by scanning electron microscopy (SEM) and showed a typical size was ~1.5-2 µm (**Figure 5-1b**). The effect of thiourea precursor ratio (1:1, 1:2, 1:4, 1:6) and aging time (6, 18 and 30h) on the morphological features of nanoassemblies were also investigated. Following an increase in thiourea precursor ratio, the MoS_2 flakes tended to grow and evolved rapidly, resulting in fully exfoliated and expanded "*flower-like"* morphology. The aging time also had significant effect on the structure of nanoassemblies. We observed that 18h is required to obtain fully exfoliated, rippled nanoassemblies, while no significant effect was observed for longer aging time (30 h).

We then confirmed the hexagonal arrangement (2H phase) of 2D MoS_2, where each Mo atom is

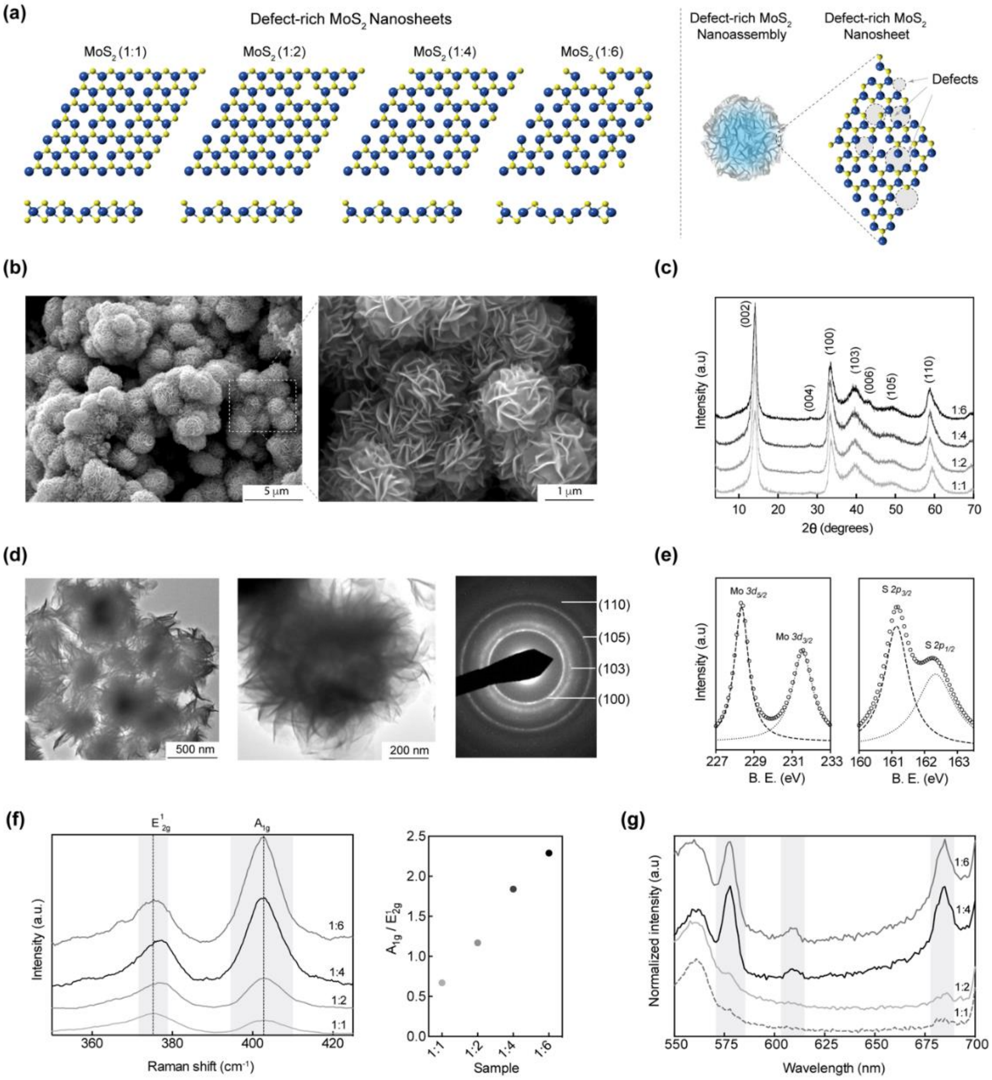

Figure 5-1. Defect-rich MoS_2 nanoassemblies. (a) The atomic lattice of MoS_2 with different Mo:S ratio, where each molybdenum atom is coordinated by six sulfur atoms at 120˚ each, giving it hexagonal arrangement. Atomic vacancies can be created by confined growth of the lattice. Defect-rich 2D MoS_2 assembles form spherical nanoassemblies. (b) SEM image of nanoassemblies shows rippled flakes arranged spherically. (c) The 2H phase of MoS_2 lattice was confirmed by X-ray diffraction pattern obtained for different feed precursor ratios (molybdenum:sulfur). (d) TEM of the nanoassemblies along with selected area electron diffraction (SAED) confirmed hierarchy of assembled nanostructure. (e) X-ray photoelectron spectroscopy of MoS_2 samples analyzed for Mo and S binding energies confirm the hexagonal arrangement. (f) Raman spectra confirmed the presence of two prominent peaks (E^1_{2g} and A_{1g}) corresponding to 2H phase, while their intensity ratio supported the consistent increment in intensity related to out-of-plane vibration of S atoms with increase in sulfur feed precursor ratio. (g) Photoluminescence (PL) spectra of MoS_2 nanoassemblies depicting the evolution of signals due to defect sites and was directly proportional to the number of active-centers. Reprinted with permission from Jaiswal et al., 2017.

coordinated with 3 in-plane sulfur atoms at 120°, using x-ray diffraction (XRD), selected area electron diffraction (SAED) and X-ray photoelectron spectra (XPS).

The diffraction peaks of nanoassemblies (100, 002, 103, 110, and 004) agree well with the hexagonal MoS_2 (JCPDS card No. 73-1508), indicating the high purity of synthesized MoS_2 (**Figure 5-1c**). The gradual decrease in peak broadness (002) as characterized by full width at half maximum (FWHM) using the Scherrer equation indicated an increase in crystallite size. FWHM for 1:1 (Mo:S) was 1.137 radians, which reduced to 0.893 radians for 1:6 (Mo:S). The crystallite size, calculated from Scherrer equation, increased from 7.82 nm for 1:1 ratio to approx. 9.96 nm for 1:6 ratio sample. These findings suggest the formation of more ordered phase of MoS_2 with increasing thiourea content, which correlates with previous reports[279-280]. The representative transmission electron microscopy (TEM) images along with the SAED pattern indicated the crystalline nature of 2D MoS_2 nanoassemblies (**Figure 5-1d**). The indexed SAED patterns corroborated the MoS_2 lattice planes observed in XRD pattern. The rippled morphology of MoS_2 nanoflakes provides easy access to active centers as it inhibits flake stacking. The XPS of MoS_2 nanoassemblies were de-convoluted for Mo and S (**Figure 5-1e**). XPS data indicate the binding energies of Mo^{4+} $3d_{5/2}$ (228.31 eV) and $3d_{3/2}$ (231.46 eV), while for to S^{2-} $2p_{3/2}$ (161.06 eV) and $2p_{1/2}$ (162.25 eV). The difference in binding energy between Mo^{4+} $3d_{5/2}$ and $3d_{3/2}$ was Δ=3.15 eV, which further confirmed the formation of dominant 2H phase. These observations indicate the formation of defect-rich MoS_2.

The number of active-centers (or defect sites) available on 2D MoS_2 nanoassemblies was determined by Raman spectroscopy and cyclic voltammetry. From the Raman spectra (**Figure 5-1f**), in-plane vibrations of two S atoms with respect to Mo (E^1_{2g}) was blue-shifted from sample 1:1

(374.3 cm^{-1}) to 1:6 (376.5 cm^{-1}), while the out-of-plane vibration of single S atom, A_{1g} (401.8 cm^{-1}) remained the same for all samples. Raman spectroscopy is a strong tool to ascertain increased built-in lattice strain by changes occurring at the E^1_{2g} peak position, which can be attributed to the rippled morphology of the crystal. Furthermore, the peak intensity of A_{1g}, which otherwise signifies the interlayer van der Waals interactions, was amplified with an increase in thiourea content, more so, the ratio of A_{1g}/E^1_{2g} was significantly enhanced from 1:1 (0.7) to 1:6 (2.3) nanoassemblies. This further demonstrates the presence of unsaturated lattice atoms and increased crystal layer thickness, as predicted by Scherrer formula in XRD data which eventually give rise to high intensity Raman peaks[281]. We further used cyclic voltammetry to determine the number of active-centers. The density of the active-centers in 1:1 was found to be 0.59×10^{-4} moles/g, which increased to 2.10×10^{-4} moles/g for 1:6. To further validate the presence of defect sites, we performed photoluminiscence (PL) spectra of nanoassemblies, as an increase in defect sites directly affects photoluminiscence characteristics of 2D MoS_2. A strong UV absorption peak was observed at 470 nm for MoS_2 nanoassemblies. Therefore, we carried out the PL spectra of these nanoassemblies by exciting at 470 nm and recording the emission spectra between 550 to 700 nm **(Figure 5-1f).** The gradual amplification in peak intensities (580, 610 and 680 nm) from 1:1 to 1:6 samples can be attributed to the increased number of defects in the crystal lattice. For lower precursor ratios (e.g. 1:1 and 1:2), due to oriented growth of the crystals, we observed fewer atomic vacancies; however, the excess addition of thiourea resulted in confined MoS_2 growth and generated more atomic vacancies. Overall these results suggested that with the increase in thiourea concentration, the number of '*active centers* (or defect site)' was also increased.

5.3.2 Gelation Kinetics of Nanoassembly Composites

We hypothesize the defect-rich MoS_2 nanoassemblies provide abundant "*active centers*" for covalent binding with multi-arm poly(ethylene-glycol) thiol (4-arm PEG-SH).

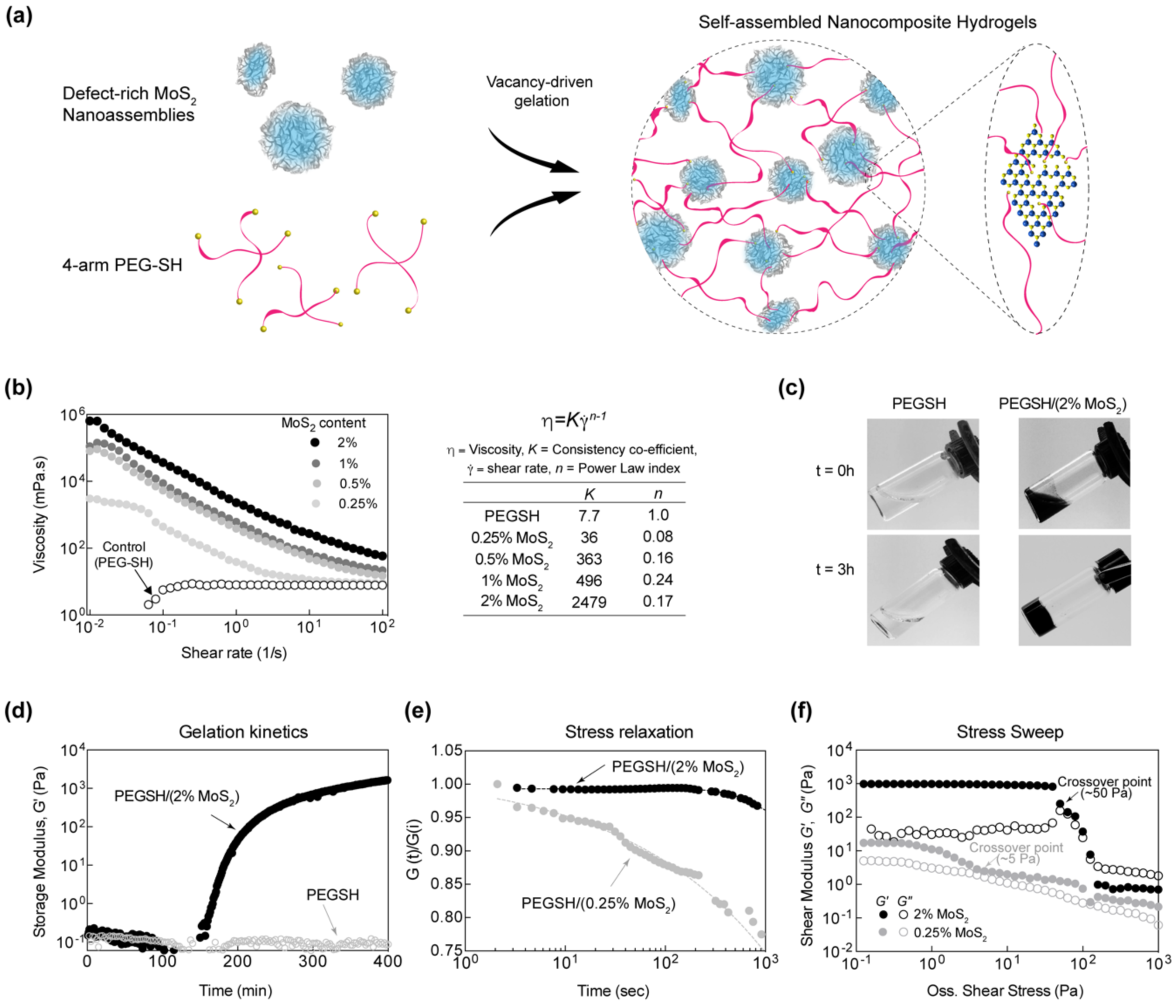

$\eta = K\dot{\gamma}^{n-1}$

η = Viscosity, K = Consistency co-efficient, $\dot{\gamma}$ = shear rate, n = Power Law index

	K	n
PEGSH	7.7	1.0
0.25% MoS_2	36	0.08
0.5% MoS_2	363	0.16
1% MoS_2	496	0.24
2% MoS_2	2479	0.17

Figure 5-2. Vacancy-driven gelation of MoS_2 and PEG-SH. (a) The presence of vacancies in MoS_2 provide "*active centers*" for chemisorption (Mo-S and S-S interactions) of thiolated polymer chains (4-arm PEG-SH) leading to formation of crosslinked hydrogels. (b) Shear-thinning characteristic of prepolymer solutions. 10% PEG-SH show Newtonian behavior. The viscosity of prepolymer solutions increases with the addition of MoS_2 and display shear-thinning characteristics. Power Law model was fitted to determine power law index and consistency co-efficient. (c) Photographs showing formation of crosslinked hydrogels from PEG-SH/2%MoS_2. While PEG-SH remain sol after 3h. (d) Gelation kinetics of PEG-SH and PEG-SH/2%MoS_2 confirm vacancy-driven gelation of defect-rich MoS_2 nanoassemblies and PEG-SH. (e) Stress relaxation behavior of crosslinked hydrogels revealed higher network stability with 2% MoS_2 compared to 0.25% MoS_2 under 5% strain. (f) Stress sweep indicate stability of crosslinked gel under shear stress. Reprinted with permission from Jaiswal et al., 2017.

Molybdenum from MoS_2 nanoassemblies maintains preferential conjugation to sulfur from PEG-SH and results in the formation of covalently crosslinked network **(Figure 5-2a)**. The potential of defect-rich MoS_2 nanoassemblies for the gelation of a polymeric network has not been previously reported to our knowledge.

By controlling the concentration of MoS_2 nanoassemblies, gelation kinetics, mechanical stiffness, and physiochemical characteristics of the hydrogel network can be modulated. The advantages of this vacancy driven gelation process are it does not require external stimuli such as UV exposure and thermal agitation and provide facile approach to encapsulate cells and proteins for biomedical applications.

Due to presence of "*active centers*", it is expected that MoS_2 nanoassemblies will strongly interact with PEG-SH. To investigate these interactions, the viscosity of prepolymer solution was determined at different shear rates using a rheometer (**Figure 5-2b**). The shear-thinning characteristics of pre-polymer solution was investigated by fitting Power Law (or Ostwald) Model. The power law index (n), calculated from fitting viscosity ($\eta = K\dot{\gamma}^{n-1}$), where K is consistency factor and $\dot{\gamma}$ is shear rate. A Newtonian fluid will have $n = 1$, while a shear-thinning fluid will have $0 < n < 1$. The viscosity of PEG-SH is unchanged at shear rate from 0.01 to 100 1/s, indicating Newtonian behavior. However, with the addition of MoS_2 nanoassemblies (1:4), viscosity of the pre-polymer solution changes significantly and display a shear-thinning characteristic ($n < 0.3$). For example, the viscosity of PEG-SH/2%MoS_2 was 10^6 mPa.s at low shear (0.01 s^{-1}) which drastically reduced to about 10 mPa.s at 100 s^{-1}.

The addition of MoS_2 nanoassemblies to PEG-SH induced vacancy-driven gelation. The gelation phenomenon is evident from the photographic images of the PEG-SH and PEG-SH/MoS_2

compositions **(Figure 5-2c)**. The gelation kinetics was monitored by placing the pre-polymer solution containing 4-arm PEG-SH (10%, M_w ~ 20,000) and MoS_2 nanoassemblies (2%) in DI-H_2O, and monitoring storage modulus (*G´*) overtime **(Figure 5-2d)**. The PEG-SH solution does not form gel as *G´* remained unchanged over 6h, while the addition of 2% MoS_2 resulted into crosslinked hydrogel within 4h as *G´* plateau at 3kPa. This indicated that the chemisorption of sulfur atoms *via* Mo-S interactions between MoS_2 nanoassemblies and PEG-SH transformed the polymer network into a viscoelastic gel.

By modulating the number of defect sites, gelation kinetics can be controlled. The gelation kinetics of pre-polymer solutions containing PEG-SH and different ratios of MoS_2 nanoassemblies (1:1, 1:2 and 1:6) were investigated. The results show that the number of defect in MoS_2 nanoassemblies control the gelation kinetics and mechanical strength of crosslinked network. For example, with an increase in vacancy sites rapid gelation and stiffer network were formed. Other parameters that can be modulated to obtain desired gelation kinetics and mechanical properties are molecular weight and/or number of thiol-activated terminals in polymeric binder. For example, shorter chain length of polymeric binder might result in significantly higher crosslinking density and limited elastomeric characteristics, while long chain polymeric binder might promote elastomeric characteristics of nanocomposite hydrogels. It is possible that if chain lengths of polymeric binders are shorter, thiol-activated terminals present on polymeric binder might conjugate on same MoS_2 nanoassemblies and may result in lower mechanical stiffness.

The network stability of the crosslinked gels is highly dependent on the molybdenum-sulfur interactions, further highlighted by stress-relaxation experiments **(Figure 5-2e)**. The crosslinked hydrogel (2 mm thick) was subjected to 5% strain (*γ*) at 1Hz and stress, *σ*, was determined as a function of time (t).

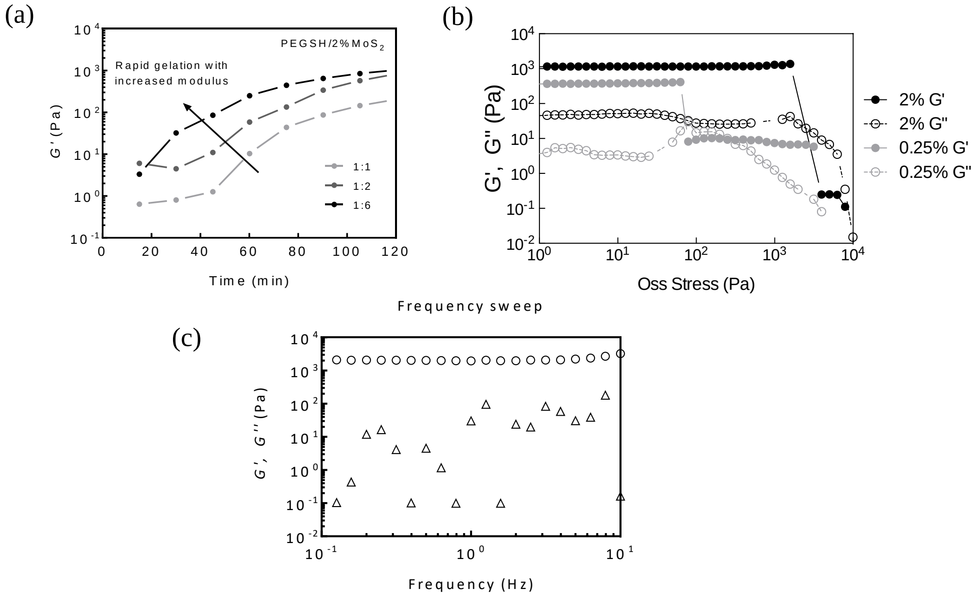

Figure 5-3. (a) Gelation of PEG-SH in presence of defect-rich MoS_2 nanoassembly synthesized in precursor ratios 1:1, 1:2 and 1:6 in cell-culture media. The presence of increased number of atomic vacancies on the MoS_2 lattice facilitates the rapid gelation and forms stiff network. (b) Osscilatory stress sweep of hydrogels prepared in cell culture media. The effect of cell culture media is substantial on crossover point of hydrogels and mechanical properties when compared gels prepared in DI water (Figure 5-2f). (c) Rheological frequency sweep for gel made with 2% MoS_2 depicts the stability of the gel up to 10 Hz of oscillation. Reprinted with permission from Jaiswal et al., 2017.

Normalized relaxation modulus was calculated as *G(t)/G(i),* where non-linear shear relaxation modulus is defined as $G(t)=\sigma(t)/\gamma$ and instantaneous modulus as *G(i).* The results showed a significant change in stability of the network with higher MoS_2 concentration over a longer time. The hydrogel with low MoS_2 concentration (PEG-SH/0.25%MoS_2) relaxed rapidly (~40s) and dissipated more than 25% of initial strain energy within 1000s. While hydrogel loaded with higher concentration of MoS_2 (PEG-SH/2%MoS_2) did not dissipate its strain energy and maintained network stability, indicating a greater prevalence of Mo-S interactions between PEG-SH and MoS_2

nanoassemblies. Furthermore, the network stability was also determined using oscillatory shear sweep experiments (**Figure 5-2f**). The crossover of G' and G'', which essentially signifies the dynamics of network rupture, occurred at ~5 Pa for PEG-SH/0.25%MoS$_2$ hydrogels and ~ 50Pa for PEG-SH/2%MoS$_2$. From the stress sweep experiment, we also determined yield stain of the crosslinked networks, where G' deviate from the linear viscoelastic region (LVR). The rheological time, stress, and frequency sweeps for PEG-SH/2% MoS$_2$ indicate a dependency on nanoassembly ratios as well as concentration of the nanoassemblies (**Figure 5-3).** The crosslinked hydrogels (PEG-SH/2%MoS$_2$) showed remarkable mechanical resilience and could be stretched, bended and twisted easily (**Figure 5-4a**).

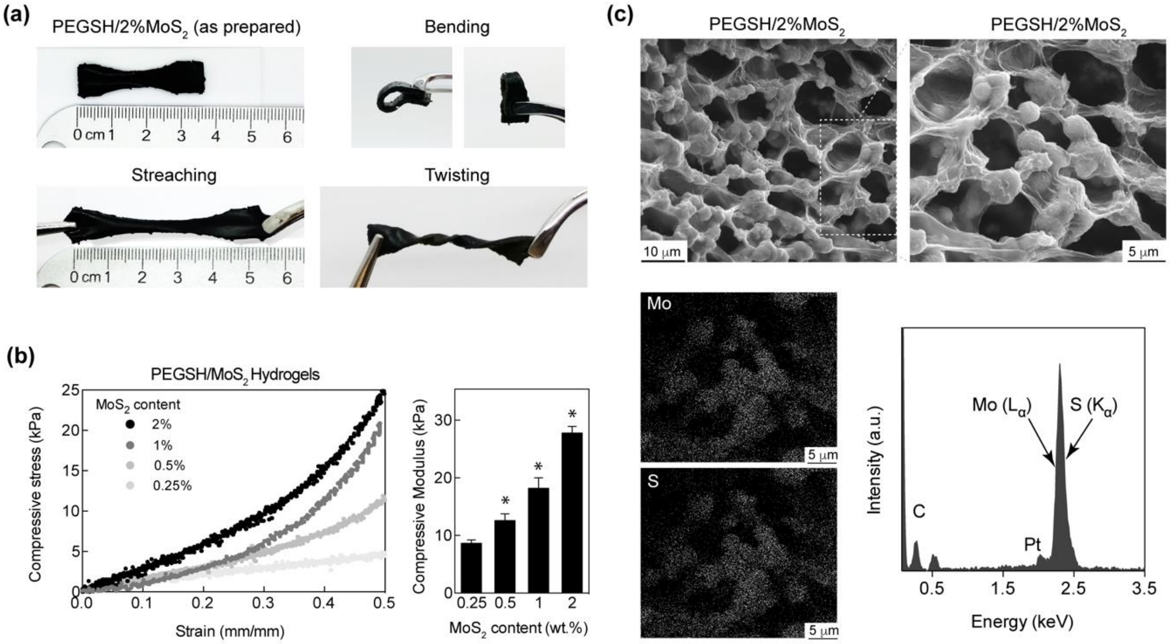

Figure 5-4. Mechanically stiff and elastomeric hydrogel from defect-rich MoS$_2$ nanoassemblies and PEG-SH. (a) Photographs of crosslinked hydrogels (PEG-SH/2% MoS$_2$) show high mechanical flexibility. Crosslinked hydrogels can sustain stretching, bending and twisting without plastic deformation and can recover back to original shape. (b) Uniaxial compression demonstrate formation of mechanically stiff hydrogel network. The compressive modulus increases from 8 kPa to 25 kPa with an increase in MoS$_2$ concentration from 0.25 to 2%. (c) SEM images of a transverse section of hydrogel (PEG-SH/2% MoS$_2$) show porous and interconnect network. Energy-dispersive X-ray spectroscopy (EDS) spectra and mapping confirmed the presence of Mo and S in the crosslinked network. Reprinted with permission from Jaiswal et al., 2017.

These hydrogels could be twisted five-times without fracture, indicating its potential use in several biomedical applications under dynamic mechanical environments. The hydrogels were further characterized *via* uniaxial compression test to determine compressive modulus from stress-strain curves. Due to a lack of gelation, PEG-SH compositions lacking MoS_2 were not evaluated. The addition of MoS_2 to PEG-SH resulted in linear increase in compressive modulus from 8.6±0.6 kPa (PEG-SH/0.25%MoS_2) to 27.7±1.1 kPa (PEG-SH/2%MoS_2) **(Figure 5-4b)**. Elastomeric characteristics of crosslinked hydrogels were investigated using cyclic compression (40% compressive strain). All PEG-SH/MoS_2 hydrogels displayed >99% recovery in compressive modulus following four cycles. These results demonstrated the mechanical robustness and elasticity of PEG-SH/MoS_2 hydrogels, highlighting the role of "*active centers*" present on MoS_2 sheets to chemically conjugate with PEG-SH.

We further carried out scanning electron microscopy (SEM) of the transverse section of freeze-dried hydrogels to determine the distribution of MoS_2 nanoassemblies within the crosslinked network (**Figure 5-4c**). SEM images show interconnected porous network with pore size ~ 10 µm. We further confirm the presence of MoS_2 nanoassemblies using energy-dispersive X-ray spectra (EDS). The EDS mapping of the selected area for Mo and S clearly confirms the presence of MoS_2 nanoassemblies interconnected with polymer.

5.3.3 Gelation Mechanism of MoS_2 Nanoassemblies

To investigate the gelation mechanism, Raman and X-ray photoelectron spectroscopy (XPS) was performed to determine the chemical conjugation between MoS_2 nanoassemblies and PEG-SH. It was expected that the vacancy-driven gelation involved Mo (from MoS_2 nanoassemblies) and S (from PEG-SH) as well as possible disulfide linkages between PEG-SH and S (from MoS_2

nanoassemblies). 4-arm PEG-SH interactions with Mo on the MoS_2 lattice formed Mo-S bond due to chemisorption at the "*active centers*" (or defect sites). Raman spectra analysis of PEG-SH shows two thiol peaks at about 670 cm^{-1} (due to -SH deformation) and 2570 cm^{-1} (due to -SH stretching) (**Figure 5-5a**). These peak intensities reduced significantly when the hydrogel was formed in presence of 0.25% MoS_2 and completely disappeared when 2% MoS_2 was added. An overall attenuation in the characteristic Raman signatures of PEG-SH in the nanocomposites was observed. This might be due to the presence of MoS_2 nanoassemblies and/or porous nature of the dried hydrogel network which hinders the number of molecules from the polymer chain to interact

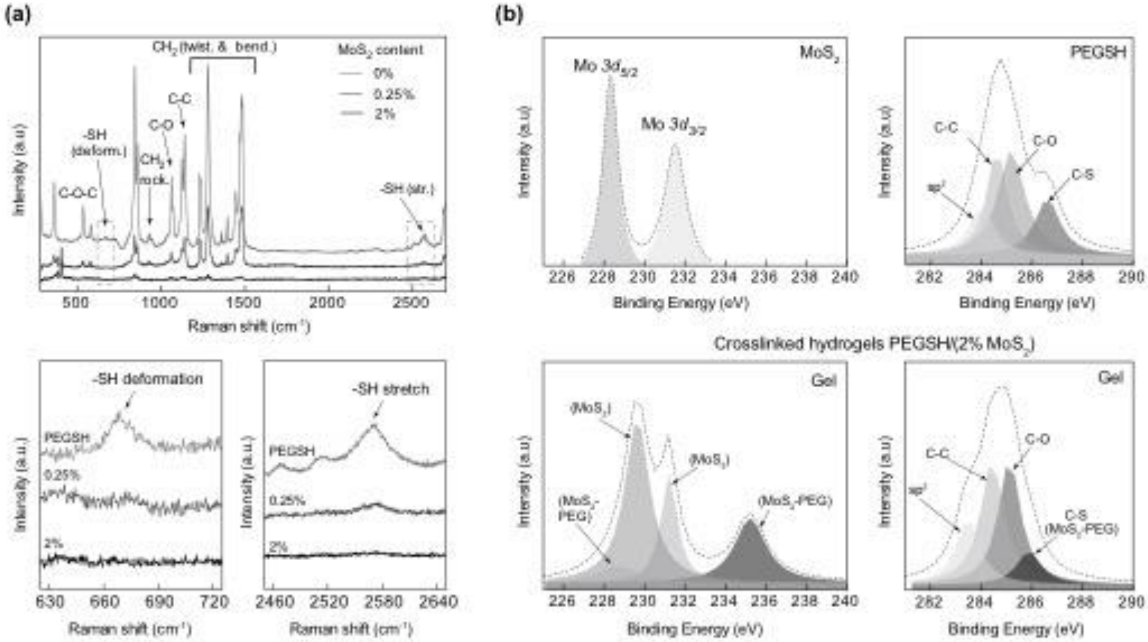

Figure 5-5. Chemical confirmation of vacancy-driven gelation. (a) Raman spectra of PEG-SH along with gels made with 0.25% and 2% MoS_2. The thiol vibrations at 670 cm^{-1} and 2570^{-1} from PEG disappeared in the crosslinked hydrogels due to formation of new bond with MoS_2. (b) XPS of hydrogel shows the change in binding energy of carbon (C 1*s*) peak due to C-S-Mo formation while two additional peaks appeared in Mo 3*d* spectrum belonging to PEG-MoS_2. Raman and XPS together suggest the new bond formation at the site of vacancy *via* chemisorption. Reprinted with permission from Jaiswal et al., 2017.

with the incident laser beam and produce Raman signals. In nanocomposite samples, the disappearance of thiol peaks demonstrates the chemisorption of sulfur (from PEG-SH) to the MoS_2 lattice due to the strong affinity of Mo atoms towards sulfur. In addition, two additional peaks at 377 cm^{-1} and 402 cm^{-1} belonging to E^1_{2g} (in-plane vibration of S atoms with respect to Mo) and A_{1g} (out-of-plane vibration of S atom) of MoS_2 were also affected due to crosslinking. For example, A_{1g}/E^1_{2g} ratio for MoS_2 nanoassemblies (1:4) was 1.9, while for crosslinked hydrogels A_{1g}/E^1_{2g} ratio was 2.05 (PEG-SH/0.25%MoS_2) and 3.44 (PEG-SH/2%MoS_2), indicating an increase in van der Waals interactions from crosslinking between MoS_2 nanoassemblies and polymer chains.

To corroborate the Raman data on gelation mechanism, we carried out XPS analysis of carbon 1*s* and molybdenum 3*d* core level electrons from covalently crosslinked hydrogels and compared them with PEG-SH and MoS_2 (**Figure 5-5b**). From carbon (1*s*) spectra, peaks belonging to sp^2, C-C, C-O and C-S in PEG appeared at 284.1, 284.7, 285.1 and 286.5 eV respectively. Binding energies for all peaks decreased after gelation, while the C-S peak decreased significantly due to direct interaction of molybdenum from MoS_2 with PEG-SH, which facilitates C-S-Mo formation. From molybdenum (3*d*) spectra, the peaks of $3d_{5/2}$ and $3d_{3/2}$ from MoS_2 shifted following gelation. In addition, Mo spectra from crosslinked hydrogels revealed formation of two new bands when compared with pristine MoS_2. Specifically, new peaks appeared at 228.2 and 235.2 eV, which can be attributed to the formation of C-S-Mo due to chemisorption of sulfur. Overall, both Raman and XPS confirmed vacancy-driven gelation mechanism between MoS_2 nanoassemblies and PEG-SH.

To evaluate the biomedical application of 2D MoS_2 nanoassemblies, we first investigated the interaction between nanoassemblies and mouse preosteoblast cells (MC3T3 E1-subclone 4). As limited studies have investigated MoS_2 nanoassemblies for biomedical applications, we evaluated morphology of cells in presence of MoS_2 nanoassemblies. Bright field microscopy revealed that MoS_2 nanoassemblies (10 μg/mL) readily attach to cell membrane and potentially internalized by cells *via* endocytosis (**Figure 5-6a**). The cells showed normal spindle shape phenotype in presence of MoS_2 nanoassemblies and no adverse toxicity was observed at macroscopic level. Following these initial assessments, cytotoxicity assay (MTT) was performed after cells were subjected to increasing concentration of MoS_2 nanoassemblies (0-10 mg/mL) (**Figure 5-6b**). The cell viability was not affected at lower concentration of MoS_2 nanoassemblies (<100 μg/mL). At higher MoS_2 nanoassemblies concentration (100μg/mL to 10 mg/mL), a decrease in cellular viability was observed ~60%. It is possible that at higher concentrations, MoS_2 nanoassemblies limit cellular function through activation of intracellular stress responses. Despite subjecting cells to 10 mg/mL MoS_2 nanoassemblies, half maximal inhibitory concentration (IC_{50}) was not observed, while other 2D nanomaterials such as nanosilicates and graphene have IC_{50} of ~ 5 mg/mL and ~1 mg/mL, respectively.[125, 282] To investigate the effect of MoS_2 nanoassemblies on cell proliferation, cell cycle analysis was performed (**Figure 5-6c**). At lower MoS_2 concentration (~ 10 μg/mL), no significant change in the G2/M population was observed, however at higher concentrations (~ 100 and 1000 μg/mL), a significant decrease in G2/M cell population was observed signifying a shift into a lower proliferative state. Moreover, at higher concentrations, a significant increase in the apoptotic population was also observed, supporting the cell viability assay. Overall, these studies demonstrate the cytocompatibility of these nanomaterials, particularly in comparison to other types of 2D nanomaterials. Furthermore, these results indicate the eventual degradation products of PEG-SH/MoS_2 gels would not inhibit normal cellular function in the surrounding tissue.

5.3.4 Biomedical Relevance of Nanocomposite Hydrogels

The facile synthesis of nanocomposite hydrogels *via* vacancy-driven gelation between MoS_2 nanoassemblies and PEG-SH can be used to encapsulate and deliver cells for regenerative medicine.

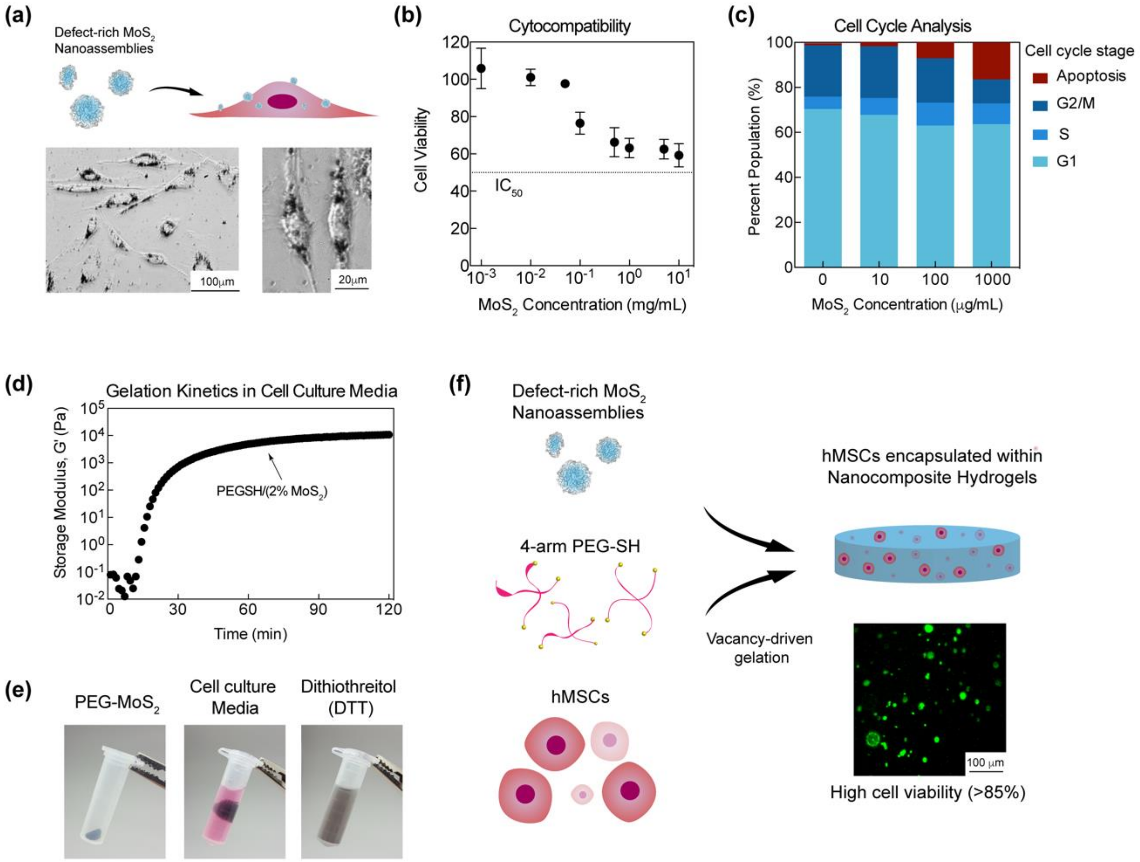

Figure 5-6. *In vitro* cytocompatibility of MoS_2 nanoassemblies and PEG-SH/MoS_2 hydrogels. (a) MoS_2 nanoassemblies readily adhere to cell membrane (dark area) and does not alter cellular morphology. (b) The viability of cells in presence of different concentrations of MoS_2 nanoassemblies was determined using MTT cytotoxicity assay. (c) The effect of MoS_2 nanoassemblies on cell-cycle was evaluated using flow cytometry. The results show that high cell population in G2/M phase at lower MoS_2 concentration shifts to apoptosis phase at higher MoS_2 concentrations. (d) Gelation kinetics of PEG-SH and 2% MoS_2 nanoassemblies (1:4) in culture media exhibited accelerated gelation and stiffer network due to the presence of mineral ions in the media. (e) The physical stability of gel in culture media as well as in excess thiol was determined. While gel maintains its structural integrity in culture media, it gets dissolve in DTT due to presence of excess thiol. (f) The facile vacancy-driven gelation between PEG-SH and MoS_2 nanoassemblies allows easy cell encapsulation without adversely affecting cell viability (> 85%) after 48h as observed in confocal microscopy image (Green=live cell, Red=dead cell). Reprinted with permission from Jaiswal et al., 2017.

To confirm the ability of hydrogel formation in cell culture media (α-MEM), we mixed MoS_2 nanoassemblies and PEG-SH and monitor the gelation kinetics using rheometer. A significant reduction in gelation time and increase in storage modulus ($G' \sim$ 11kPa) in 1.5 h was observed (**Figure 5-6d**). The improved gelation kinetics in cell culture media compared to DI water might be attributed to the presence of mineral ions that facilitate the vacancy-driven reaction. The stability of nanocomposite hydrogels in cell culture media was monitored for 48 hours to evaluate its ability to support encapsulated cells (**Figure 5-6e**). PEG-SH/2%MoS_2 hydrogels readily swelled (4-6 times) in media and retained the initial shape. However, a significant dissociation was observed in solutions containing excess thiols (*e.g.* dithiothreitol (DTT)), indicating a breakdown of thiol-based linkages between PEG-SH and MoS_2 nanoassemblies. The stability of nanocomposites hydrogels in media is expected to limit the immediate release of MoS_2 nanoassemblies, maintaining concentrations within cytocompatible ranges.

Due to facile cross-linking process, we can encapsulate cells within the nanocomposite hydrogel network. As no photoinitiator or radical initiators were used, it is expected that cells will be able to survive the gelation process. We added cells to pre-polymer solutions containing 10% PEG-SH and 2% MoS_2 nanoassemblies in cell culture media. The gelation was allowed by placing the gel solution within a well-plate and incubated at 37 ^{o}C. Cells survive the gelation process and maintain high viability after 48 hours, as evident by high number of live (green) cells compared to dead cells (red) (**Figure 5-6f**). This show that vacancy-driven gelation between MoS_2 nanoassemblies and PEG-SH has the potential to deliver cells for regenerative medicine.

5.4 Conclusion

Overall, we demonstrated a new approach to form chemically crosslinked hydrogels by utilizing vacancies in 2D TMDs and polymeric binder. This approach explored planar and edge atomic defects available on 2D nanomaterials, which can be easily generalized to other 2D nanomaterials. We successfully synthesized a range of defect-rich MoS_2 nanoassemblies by allowing the confined growth of the lattice with atomic defects. These defect-rich MoS_2 nanoassemblies provided abundant "*active centers*" for covalently binding multi-arm PEG thiol. The addition of MoS_2 nanoassemblies to PEG-SH induced vacancy-driven gelation and results in covalently crosslinked hydrogel networks. Molybdenum, from MoS_2 nanoassemblies, demonstrated preferential conjugation to sulfur from PEG-SH. As nanoassemblies can have controlled generation of active sites, conjugation to multiple polymeric chains is enabled, virtually acting as a crosslink epicenter to reinforce polymeric hydrogels. Mechanically robust and elastic hydrogels were formed using this facile process without external stimuli such as UV exposure, thermal agitation, chemical radical etc. MoS_2 nanoassemblies and nanocomposite hydrogels are cytocompatible and can be used to encapsulate cells. The vacancy-driven gelation approach can be used for a range of biomedical applications including tissue engineering, regenerative medicine, and cell and therapeutic delivery. In addition, the hydrogels loaded with MoS_2 nanoassemblies can be used to develop light-actuating structures using 3D bioprinting. The proposed vacancy-driven gelation can be widely-applied to form hydrogels from different types of 2D nanomaterials for biomedical applications.

6. FUTURE RECOMMENDATIONS

The current tissue engineering paradigm is a convergence of three primary components that work in concert to produce functional tissue regeneration, specifically biological cells, biochemical factors, and scaffolding material.[175] As evidence by much of this work, researchers are currently devising methods to transition away from incorporating biological cues to that of a completely synthetic system for stem cell induction. Central to this transition; however, is the determination of cellular analysis techniques that best predict regenerative outcomes short of introducing the investigated nanomaterial into the body. The majority of publications in literature tend to limit their scope to known genetic and protein targets indicative of differentiation. While we extended our examinations of nanomaterial-cell interactions to monitor whole-transcriptome changes within the population using RNA-sequencing, we were still limited to a single time point, single dosage and duration, and single cell type. Even though our study provided this view at a single moment in time, we can add our data to the Gene Expression Omnibus (GEO). This online repository enables investigators from around the world to submit their functional genomics data within a single digital location. External users can leverage this curated information by searching for specific transcripts of interest and scale factors against each other to elucidate mechanistic patterns.

One group that has taken advantage of this availability of information is that of the Discher Group at the University of Pennsylvania. In a recent publication, they utilized previous findings by other groups to generate nonlinear scaling relationships between factors or transcripts that were previously undiscovered.[283] This post-hoc analysis enables investigations between gene targets stimulated by a variety of mechanisms. From this, we can better understand potential pathways regulating cell behavior during the regenerative process. Following a similar protocol, it would be useful to generate a library of scaling sets as predictors for stem cell induction that could further be expanded to bioactive nanomaterial evaluation. Furthermore, these genomic factors could be compared against proteomic data considering RNA transcript translation into proteins are superior indicators of changes to stem cell phenotype.

This comparison of 2D nanomaterials provided a novel investigation into the effects of nanoparticle chemistry and size on cell behavior while maintaining anisotropic structure. A limitation of this perspective, however, is that the size and chemistry could not be decoupled following nanomaterial synthesis. To better address this concern, new 2D nanoparticles could be synthesized to generate nanoparticles with variable chemistry while maintaining size and 2D structure. Specifically, a variety of stoichiometric mineral combinations could be attempted using a modified Stöber method.[284] A synthesized library of mineral nanoparticles would differentiate the effects size and chemistry on stem cell behavior. These particles could be multiplexed using the newly defined RNA-seq methodology outlined here. Results generated from these experiments would indicate changes to stem cell transcriptome and direct future investigations into potential regenerative avenues for the 2D nanomaterials.

Lastly, there is a lack of understanding regarding nanoparticle outcomes within hydrogel systems with encapsulated cells. Specifically, tracking nanoparticle interactions with cells over time is difficult without chemical modifications to the particle surface. One potential option would be to section constructs after fixation and perform Raman Scattering analysis over areas of a single cell to evaluate uptake within a 3D environment. Alternatively, hyperspectral imaging may be able to discern the distribution of nanoparticles in and around embedded cells. Results from these experiments would provide insight as to the kinetics and amount of direct interactions with nanomaterials within these potentially implantable materials. It is expected that uptake of particles within hydrogels would be significantly reduced due to the physical and/or chemical interactions with the surrounding polymeric matrix. The effect of this reduction on engineering cell behavior will require future *in vivo* analysis to quantify biocompatibility and regenerative success.

7. CONCLUSIONS

Over the course of these studies, we introduced a novel comprehensive methodology to approach nanoparticle characterization with stem cells. Specifically, by uncovering the interactions between cells and 2D nanoparticles, cell behavior can be tailored toward a specific regenerative response. Furthermore, following characterization, we can incorporate these nanomaterials into 3D hydrogel scaffolds. In all, we have concluded that whole transcriptome analyses provides a suitable foundation from which to build a collection of nanocomposite scaffolds for regenerative engineering.

In Study 1, “Whole-Transcriptome Analysis of 2D Nanosilicate Treated Stem Cells,” a novel methodology was developed to evaluate holistic changes to stem cell signaling for regenerative engineering applications following an introduction of a nanomaterial. Specifically, Laponite XLG, a nanosilicate, was introduced to evaluate potential genomic mechanisms of bioactivity towards osteochondral lineages. From this study, nanosilicates triggered a cascade of signaling pathways, predominantly through membrane receptor-triggered and stress-responsive MAPK avenues. Subsequently, stem cells synthesized proteins indicative of both osteo- and chondrogenic lineages, depending on media conditions, and could be inhibited through a chemical means targeting MEK1/2 signaling within MAPK. In all, we developed a framework from which to evaluate the regenerative potential of novel nanomaterials.

In Study 2, “Nanosilicate-Polysaccharide Composites for Cartilage Bioprinting” bioactive nanosilicates from Study 1 were incorporated within multiple natural polymer kappa-Carrageenan systems. Chemical modifications to the polymer backbone enabled multiple crosslinking mechanisms, providing enhanced control over mechanical and biological properties. The inclusion of nanosilicates within these polymeric solutions rendered these nanocomposites injectable and printable as bioinks, useful particularly for fabricating personalized cartilage-specific matrices. On-demand UV crosslinking of methacrylated kappa-Carrageenan inks provided structural robustness capable of generating unique 3D structures following extrusion from a printer nozzle while maintaining cell viability.

From the perspective of a separate 2D nanomaterial, in Study 3, “Molybdenum Disulfide as a stimuli responsive 2D nanomaterial for regenerative medicine” we characterized changes in stem cell behavior again using molecular biology techniques following nanomaterial introduction, as demonstrated in Study 1. Synthesized nanosheets of chemically exfoliated molybdenum disulfide displayed notable cytocompatibility in vitro. Furthermore, nanosheets provided near infrared responsiveness to activate stress-responsive pathways within treated stem cells. A focused laser on treated stem cells initiated cell apoptosis due to local ablation. However, a reduction in near infrared power in the form of LEDs motivated stem cells to differentiate.

Lastly, molybdenum disulfide was chemically crosslinked within hydrogels in Study 4, “Manish’s paper”. A four-arm poly(ethylene glycol) with terminal thiol groups provided sites to attack defect-rich sites on the molybdenum disulfide nanomaterial surface. Hierarchical structures of molybdenum disulfide were developed to leverage the unique anisotropic structure of the nanomaterial for the generation of stable hydrogel constructs. Changing the number of atomic defect sites through chemical means during synthesis impacted gelation kinetics and mechanical robustness. Stem cells could be encapsulated within these nanocomposite solutions during the crosslinking process to generate cell-laden hydrogel constructs.

Taking an unbiased approach to measure the stem cell transcriptome has the potential to uncover pathways of activation not previously considered. To achieve this sensitive yet holistic snapshot, RNA-sequencing plays a central role. At any given time point, we can directly compare signaling of cell populations under a variety of media conditions. Subsequently, we can generate quantitative data that highlights differences or similarities between current growth factor therapies and nanomaterials of interest. While this technique may elucidate a wide array of cellular function from a genetic perspective, all conclusions need to be placed in the context of time. In other words, duration of treatment and timing of RNA isolation from samples will significantly impact transcriptome profiles. As a safeguard for researchers, validation of RNA-sequencing data is required prior to drawing conclusions regarding nanomaterial regenerative potential. Downstream protein synthesis and movement of cell machinery can provide a more targeted measurement of changes to cell phenotype after performing RNA-sequencing.

From a biomedical engineering standpoint, these nanomaterials can be introduced to cells as a therapy through a couple of methods. Nanomaterials can be applied to cultured cells prior to injection of these expanded populations in an attempt to direct cell behavior ex vivo. Due to low viability following injection of these cells, hydrogel vehicles containing the nanomaterial of interest can be utilized to both shield cells from high shear stresses and localize biological material in the body. Furthermore, by incorporating nanomaterials within a three-dimensional space, cells may receive bioactive cues that more aptly mimic the physiological environment. Couple this with a more anatomically relevant hydrogel structure, achieved by three-dimensional printing, and implant success may be improved.

Transcriptomic evaluation uncovers a wide array of signaling events following treatment with two-dimensional nanomaterials. These results can be leveraged to engineer enhanced three-dimensional hydrogel constructs to augment those highlighted signaling processes. In all, this culmination of work takes a fundamental biological perspective to improve the tissue engineering process.

REFERENCES

1. Gaharwar, A. K.; Peppas, N. A.; Khademhosseini, A., Nanocomposite hydrogels for biomedical applications. *Biotechnology and Bioengineering* **2014,** *111* (3), 441-453.

2. Cha, C.; Shin, S. R.; Annabi, N.; Dokmeci, M. R.; Khademhosseini, A., Carbon-Based Nanomaterials: Multifunctional Materials for Biomedical Engineering. *ACS nano* **2013,** *7* (4), 2891-2897.

3. Dvir, t.; timko, B. P.; Kohane, D. S.; langer, r., nanotechnological strategies for engineering complex tissues. *nature nanotechnology* **2010,** *6*.

4. Wang, Z.; Ruan, J.; Cui, D., Advances and Prospect of Nanotechnology in Stem Cells. *Nanoscale Res Lett* **2009,** *4*, 593–605.

5. Zhao, F.; Zhao, Y.; Liu, Y.; Chang, X.; Chen, C.; Zhao, Y., Cellular Uptake, Intracellular Traffi cking, and Cytotoxicity of Nanomaterials. *Small* **2011,** *7* (10), 1322–1337.

6. Maila¨nder, V.; Landfester, K., Interaction of Nanoparticles with Cells. *Biomacromolecules* **2009,** *10*, 2379–2400.

7. Zhang, Y.; Nayak, T. R.; Hongb, H.; Cai, W., Graphene: a versatile nanoplatform for biomedical applications. *Nanoscale* **2012,** *4*, 3833.

8. XIA, Y., Nanomaterials at work in biomedical research. *Nature materials* **2008,** *7*.

9. Ferreira, L., Nanoparticles as Tools to Study and Control Stem Cells. *Journal of cellular biochemistry* **2009,** *108*, 746–752.

10. Singh, A.; Sangital; Sharma, A., Overview of Bottom-up Nano Electronics Materials and Its Application. *JOURNAL OF NANO- AND ELECTRONIC PHYSICS* **2012,** *4* (2).

11. Wan, A. C. A.; Ying, J. Y., Nanomaterials for in situ cell delivery and tissue regeneration. *Advanced drug delivery reviews* **2010,** *62*, 731–740.

12. Martı´nez, E.; E.Engel; J.A.Planell; J.Samitier, Effects ofartificialmicro-andnano-structured surfacesoncellbehaviour. *Anals of Anatomy* **2009,** *191*, 126—135.

13. Suh, W. H.; Suh, Y.-H.; Stucky, G. D., Multifunctional nanosystems at the interface of physical and life sciences. *Nano Today* **2009,** *4*, 27-36.

14. Kshitiz; Kim, D.-H.; Beebe, D. J.; Levchenko, A., Micro- and nanoengineering for stem cell biology: the promise with a caution. *Trends Biotechnol* **2011,** *29* (8).

15. Okamoto, M.; John, B., Synthetic biopolymer nanocomposites for tissue engineeringscaffolds. *Progress in Polymer Science* **2013,** *xxx*, xxx-xxx.

16. Ferreira, L.; Karp, J. M.; Nobre, L.; Langer, R., New Opportunities: The Use of Nanotechnologies to Manipulate and Track Stem Cells. *Cell Stem Cell* **2008,** *3*.

17. Shi, J.; Votruba, A. R.; Farokhzad, O. C.; Langer, R., Nanotechnology in Drug Delivery and Tissue Engineering: From Discovery to Applications. *Nano letters* **2010,** *10*, 3223–3230.

18. Gaharwar, A. K.; Mihaila, S. M.; Swami, A.; Patel, A.; Sant, S.; Reis, R. L.; Marques, A. P.; Gomes, M. E.; Khademhosseini, A., Bioactive Silicate Nanoplatelets for Osteogenic Differentiation of Human Mesenchymal Stem Cells. *Advanced Materials* **2013**.

19. Ding, H.; Helguera, G.; Rodríguez, J. A.; Markman, J.; Luria-Pérez, R.; Gangalum, P.; Portilla-Arias, J.; Inoue, S.; Daniels-Wells, T. R.; Black, K.; Holler, E.; Penichet, M. L.; Ljubimova, J. Y., Polymalic acid nanobioconjugate for simultaneous immunostimulation and inhibition of tumor growth in HER2/neu-positive breast cancer. *J Control Release* **2013,** *xxx*, xxx-xxx.

20. Liu, J.; Sun, Y.; Drubin, D. G.; Oster, G. F., The mechanochemistry of endocytosis. *PLoS biology* **2009,** *7* (9), e1000204.

21. Langston Suen, W. L.; Chau, Y., Size-dependent internalisation of folate-decorated nanoparticles via the pathways of clathrin and caveolae-mediated endocytosis in ARPE-19 cells. *J Pharm Pharmacol* **2014,** *66* (4), 564-73.

22. Gan, Q.; Dai, D.; Yuan, Y.; Qian, J.; Sha, S.; Shi, J.; Liu, C., Effect of size on the cellular endocytosis and controlled release of mesoporous silica nanoparticles for intracellular delivery. *Biomed Microdevices* **2012,** *14* (2), 259-70.

23. He, Y.; Park, K., Effects of the Microparticle Shape on Cellular Uptake. *Molecular pharmaceutics* **2016,** *13* (7), 2164-71.

24. Chen, L.; Xiao, S.; Zhu, H.; Wang, L.; Liang, H., Shape-dependent internalization kinetics of nanoparticles by membranes. *Soft Matter* **2016,** *12* (9), 2632-41.

25. Dawson, E.; Mapili, G.; Erickson, K.; Taqvi, S.; Roy, K., Biomaterials for stem cell differentiation. *Advanced drug delivery reviews* **2008,** *60*, 215–228.

26. Ravichandran, R.; Liao, S.; Ng, C. C.; Chan, C. K.; Raghunath, M.; Ramakrishna, S., Effects of nanotopography on stem cell phenotypes. *World J Stem Cells* **2009,** *1* (1), 55-66.

27. Martinez; Lagunas; Mills, C.; Rodriguez-Segui; Estevez; Oberhansl; Comelles; Samitier, Stem cell differentiation by functionalized micro- and nanostructured surfaces. *Nanomedicine* **2009,** *4* (1), 65–82.

28. Ilie, I.; Ilie, R.; Mocan, T.; Bartos, D.; Mocan, L., Influence of nanomaterials on stem cell differentiation: designing an appropriate nanobiointerface. *International Journal of Nanomedicine* **2012,** *2* (7), 2211–2225.

29. Bang, A. G.; Carpenter, M. K., Deconstructing Pluripotency. *Science* **2008,** *320*.

30. Tachibana, M.; Amato, P.; Sparman, M.; Gutierrez, N. M.; Tippner-Hedges, R.; Ma, H.; Kang, E.; Fulati, A.; Lee, H.-S.; Sritanaudomchai, H.; Masterson, K.; Larson, J.; Eaton, D.; Sadler-Fredd, K.; Battaglia, D.; Lee, D.; Wu, D.; Jensen, J.; Patton, P.; Gokhale, S.; Stouffer, R. L.; Wolf, D.; Mitalipov, S., Human Embryonic Stem Cells Derived by Somatic Cell Nuclear Transfer. *Cell* **2013,** *153*, 1228–1238.

31. Stadtfeld, M.; Hochedlinger, K., Induced pluripotency: history, mechanisms, and applications. *GENES & DEVELOPMENT* **2010,** *24*, 2239–2263.

32. Zhang, L.; Webster, T. J., Nanotechnology and nanomaterials: Promises for improved tissue regeneration. *Nano Today* **2009,** *4*, 66—80.

33. McNamara, L. E.; McMurray, R. J.; Biggs, M. J. P.; Kantawong, F.; Oreffo, R. O. C.; J.Dalby, M., Nanotopographical Control of Stem Cell Differentiation. *Journal of Tissue Engineering* **2010,** *1*.

34. Martino, S.; D'Angelo, F.; Armentano, I.; Kenny, J. M.; Orlacchio, A., Stem cell-biomaterial interactions for regenerative medicine. *Biotechnology advances* **2012,** *30*, 338–351.

35. stro¨m, T. S.; Dalby, M. J.; Hart, A.; Tare, R.; Oreffo, R. O. C.; Sua, B., Fabrication of pillar-like titania nanostructures on titanium and their interactions with human skeletal stem cells. *Acta Biomater* **2009,** *5*, 1433–1441.

36. AshaRani, P. V.; Mun, G. L. K.; Hande, M. P.; Valiyaveettil, S., Cytotoxicity and Genotoxicity of Silver Nanoparticles in Human Cells. *ACS Nano* **2009,** *3* (2), 279–290.

37. Hackenberg, S.; Scherzed, A.; Kessler, M.; Hummel, S.; Technau, A.; Froelich, K.; Ginzkey, C.; Koehler, C.; Hagen, R.; Kleinsasser, N., Silver nanoparticles: Evaluation of DNA damage, toxicity and functional impairment in human mesenchymal stem cells. *Toxicology Letters* **2011,** *201*, 27–33.

38. Smith, L. A.; Liu, X.; Ma, P. X., Tissue engineering with nano-fibrous scaffolds. *Soft Matter* **2008,** *4*, 2144–2149.

39. Parker, K. K.; Ingber, D. E., Extracellular matrix, mechanotransduction and structural hierarchies in heart tissue engineering. *Phil. Trans. R. Soc. B* **2007,** *362*, 1267–1279.

40. Kim, D.-H.; Lipke, E. A.; Kim, P.; Cheong, R.; Thompson, S.; Delannoy, M.; Suh, K.-Y.; Tung, L.; Levchenko, A., Nanoscale cues regulate the structure and function of macroscopic cardiac tissue constructs. *Proc. Natl Acad. Sci. USA* **2010,** *107*.

41. Howard, D.; Buttery, L. D.; Shakesheff, K. M.; Roberts, S. J., Tissue engineering: strategies, stem cells and scaffolds. *Journal of Anatomy* **2008,** *213*, 66–72.

42. Zhang, S.; Uludağ, H., Nanoparticulate Systems for Growth Factor Delivery. *Pharm Res* **2009,** *26* (7).

43. Armentano, I.; Dottori, M.; Fortunati, E.; Mattioli, S.; Kenny, J. M., Biodegradable polymer matrix nanocomposites for tissue engineering: A review. *Polymer Degradation and Stability* **2010,** *95*, 2126-2146.

44. Tran, L. A.; Krishnamurthy, R.; Muthupillai, R.; Cabreira-Hansen, M. d. G.; Willerson, J. T.; Perin, E. C.; Wilson, L. J., Gadonanotubes as magnetic nanolabels for stem cell detection. *Biomaterials* **2010,** *31*, 9482-9491.

45. Wang, Y.; Xu, F.; Zhang, C.; Lei, D.; Tang, Y.; Xu, H.; Zhang, Z.; Lu, H.; Du, X.; Yang, G.-Y., High MR sensitive fluorescent magnetite nanocluster for stem cell tracking in ischemic mouse brain. *Nanomedicine: Nanotechnology, Biology, and Medicine* **2011,** *7*, 1009–1019.

46. Liu, K.-K.; Wang, C.-C.; Cheng, C.-L.; Chao, J.-I., Endocytic carboxylated nanodiamond for the labeling and tracking of cell division and differentiation in cancer and stem cells. *Biomaterials* **2010,** *30*, 4249–4259.

47. Bakota, E. L.; Wang, Y.; Danesh, F. R.; Hartgerink, J. D., Injectable Multidomain Peptide Nanofiber Hydrogel as a Delivery Agent for Stem Cell Secretome. *Biomacromolecules* **2011,** *12*, 1651–1657.

48. Gul1, H.; Lu1, W.; PengXu1; JamesXing; Chen, J., Magnetic carbon nanotube labelling for haematopoietic stem/progenitor cell tracking. *Nanotechnology* **2010,** *21*, 155101 (9pp).

49. Green, J. J.; Zhou, B. Y.; Mitalipova, M. M.; Beard, C.; Langer, R.; Jaenisch, R.; Anderson, D. G., Nanoparticles for Gene Transfer to Human Embryonic Stem Cell Colonies. *Nano letters* **2008,** *8* (10), 3126-3130.

50. Solanki, A.; Kim, J. D.; Lee, K.-B., Nanotechnology for regenerative medicine: nanomaterials for stem cell imaging. *Nanomedicine* **2008,** *3* (4), 567–578.

51. Yukawa, H.; Mizufune, S.; Mamori, C.; Kagami, Y.; Oishi, K.; Kaji, N.; Okamoto, Y.; Takeshi, M.; Noguchi, H.; Baba, Y.; Hamaguchi, M.; Hamajima, N.; Hayashi, S., Quantum Dots for Labeling Adipose Tissue-Derived Stem Cells. *Cell Transplant* **2009,** *18*, 591–599.

52. Gaharwar, A. K.; Peppas, N. A.; Khademhosseini, A., Nanocomposite hydrogels for biomedical applications. *Biotechnol. Bioeng.* **2014,** *111* (3), 441-453.

53. Sanchez, C.; Arribart, H.; Guille, M. M. G., Biomimetism and bioinspiration as tools for the design of innovative materials and systems. *Nat. Mater.* **2005,** *4* (4), 277-288.

54. Fratzl, P.; Weinkamer, R., Nature's hierarchical materials. *Prog. Mater. Sci.* **2007,** *52* (8), 1263-1334.

55. Bixler, G. D.; Bhushan, B., Bioinspired rice leaf and butterfly wing surface structures combining shark skin and lotus effects (vol 8, pg 11271, 2012). *Soft Matter* **2012,** *8* (48), 12139-12143.

56. Parsons, A. J.; Ahmed, I.; Han, N.; Felfel, R.; Rudd, C. D., Mimicking Bone Structure and Function with Structural Composite Materials. *J. Bionics Eng.* **2010,** *7*, S1-S10.

57. Zhu, Y. J.; Wu, H.; Sun, S. F.; Zhou, T.; Wu, J. J.; Wan, Y., Designed composites for mimicking compressive mechanical properties of articular cartilage matrix. *J. Mech. Behav. Biomed. Mater.* **2014,** *36*, 32-46.

58. Luz, G. M.; Mano, J. F., Biomimetic design of materials and biomaterials inspired by the structure of nacre. *Philos. Trans. A Math. Phys. Eng. Sci.* **2009,** *367* (1893), 1587-1605.

59. Wang, Y. Z.; Kim, H. J.; Vunjak-Novakovic, G.; Kaplan, D. L., Stem cell-based tissue engineering with silk biomaterials. *Biomaterials* **2006,** *27* (36), 6064-6082.

60. Khademhosseini, A.; Langer, R.; Borenstein, J.; Vacanti, J. P., Microscale technologies for tissue engineering and biology. *Proc. Natl. Acad. Sci. U.S.A.* **2006,** *103* (8), 2480-2487.

61. Fisher, O. Z.; Khademhosseini, A.; Langer, R.; Peppas, N. A., Bioinspired materials for controlling stem cell fate. *Acc. Chem. Res.* **2010,** *43* (3), 419-28.

62. Rho, J. Y.; Kuhn-Spearing, L.; Zioupos, P., Mechanical properties and the hierarchical structure of bone. *Med. Eng. Phys.* **1998,** *20* (2), 92-102.

63. Tjong, S. C., Structural and mechanical properties of polymer nanocomposites. *Mater. Sci. Eng. R-Rep.* **2006,** *53* (3-4), 73-197.

64. Kutvonen, A.; Rossi, G.; Ala-Nissila, T., Correlations between mechanical, structural, and dynamical properties of polymer nanocomposites. *Phys. Rev. E* **2012,** *85* (4).

65. Wu, C.-J.; Gaharwar, A. K.; Schexnailder, P. J.; Schmidt, G., Development of biomedical polymer-silicate nanocomposites: a materials science perspective. *Materials* **2010,** *3* (5), 2986-3005.

66. Schexnailder, P. J.; Jin, Q.; Gaharwar, A.; Wu, C. J.; Schmidt, G., Development of bio-nanocomposite hydrogels based on silicate cross-linked Peo for tissue engineering. *Tissue Eng. Pt. A* **2008,** *14* (5), 836-836.

67. Schexnailder, P.; Schmidt, G., Nanocomposite polymer hydrogels. *Colloid. Polym. Sci.* **2009,** *287* (1), 1-11.

68. Chae, T.; Yang, H.; Ko, F.; Troczynski, T., Bio-inspired dicalcium phosphate anhydrate/poly(lactic acid) nanocomposite fibrous scaffolds for hard tissue regeneration: In situ synthesis and electrospinning. *J. Biomed. Mater. Res. A* **2014,** *102* (2), 514-522.

69. Gaharwar, A. K.; Mihaila, S. M.; Swami, A.; Patel, A.; Sant, S.; Reis, R. L.; Marques, A. P.; Gomes, M. E.; Khademhosseini, A., Bioactive silicate nanoplatelets for osteogenic differentiation of human mesenchymal stem cells. *Adv. Mater.* **2013,** *25* (24), 3329-36.

70. Liu, X.; Smith, L. A.; Hu, J.; Ma, P. X., Biomimetic nanofibrous gelatin/apatite composite scaffolds for bone tissue engineering. *Biomaterials* **2009,** *30* (12), 2252-8.

71. Azami, M.; Moosavifar, M. J.; Baheiraei, N.; Moztarzadeh, F.; Ai, J., Preparation of a biomimetic nanocomposite scaffold for bone tissue engineering via mineralization of gelatin hydrogel and study of mineral transformation in simulated body fluid. *J. Biomed. Mater. Res. A* **2012,** *100* (5), 1347-55.

72. Kawashita, M.; Nakao, M.; Minoda, M.; Kim, H. M.; Beppu, T.; Miyamoto, T.; Kokubo, T.; Nakamura, T., Apatite-forming ability of carboxyl group-containing polymer gels in a simulated body fluid. *Biomaterials* **2003,** *24* (14), 2477-84.

73. Oyane, A.; Uchida, M.; Choong, C.; Triffitt, J.; Jones, J.; Ito, A., Simple surface modification of poly(epsilon-caprolactone) for apatite deposition from simulated body fluid. *Biomaterials* **2005,** *26* (15), 2407-13.

74. Kam, N. W. S.; Jan, E.; Kotov, N. A., Electrical Stimulation of Neural Stem Cells Mediated by Humanized Carbon Nanotube Composite Made with Extracellular Matrix Protein. *Nano letters* **2009,** *9* (1), 273-278.

75. Wu, S.; Liu, X.; Hu, T.; Chu, P. K.; Ho, J. P. Y.; Chan, Y. L.; Yeung, K. W. K.; Chu, C. L.; Hung, T. F.; Huo, K. F.; Chung, C. Y.; Lu, W. W.; Cheung, K. M. C.; Luk, K. D. K., A Biomimetic Hierarchical Scaffold: Natural Growth of Nanotitanates on Three-Dimensional Microporous Ti-Based Metals. *Nano letters* **2008,** *8* (11), 3803-3808.

76. Souzal, G. R.; Molina, J. R.; Raphael, R. M.; Ozawa1, M. G.; Stark, D. J.; Levin, C. S.; Bronk, L. F.; Ananta, J. S.; Mandelin, J.; Georgescu, M.-M.; Bankson, J. A.; Gelovani, J. G.;

Killian, T. C.; Arap, W.; Pasqualini, R., Three-dimensional tissue culture based on magnetic cell levitation. *NATURE NANOTECHNOLOGY* **2010,** *5*.

77. Gaharwar, A. K.; Kishore, V.; Rivera, C.; Bullock, W.; Wu, C.-J.; Akkus, O.; Schmidt, G., Physically Crosslinked Nanocomposites from Silicate-Crosslinked PEO: Mechanical Properties and Osteogenic Differentiation of Human Mesenchymal Stem Cells. *Macromol. Biosci.* **2012,** *12*, 779–793.

78. Wang, S.; Castro, R.; An, X.; Song, C.; Luo, Y.; Shen, M.; Tomas, H.; Zhu, M.; Shi, X., Electrospun laponite-doped poly(lactic-co-glycolic acid) nanofibers for osteogenic differentiation of human mesenchymal stem cells. *J Mater Chem* **2012,** *22*, 23357.

79. Gaharwar, A. K.; Mukundan, S.; Karaca, E.; Dolatshahi-Pirouz, A.; Patel, A.; Rangarajan, K.; Mihaila, S. M.; Iviglia, G.; Zhang, H.; Khademhosseini, A., Fabrication and Characterization of Nanoclay-Enriched Poly(e-caprolactone) Electrospun Scaffolds for Osteogenic Differentiation of Human Mesenchymal Stem Cells. *TISSUE ENGINEERING: Part A* **2014,** *9* (S1).

80. Khademhosseini, A.; Vacanti, J. P.; Langer, R., Progress in tissue engineering. *Sci. Am.* **2009,** *300* (5), 64-71.

81. Place, E. S.; Evans, N. D.; Stevens, M. M., Complexity in biomaterials for tissue engineering. *Nat. Mater.* **2009,** *8* (6), 457-470.

82. Mironov, V.; Reis, N.; Derby, B., Review: bioprinting: a beginning. *Tissue engineering* **2006,** *12* (4), 631-4.

83. Hutmacher, D. W.; Sittinger, M.; Risbud, M. V., Scaffold-based tissue engineering: rationale for computer-aided design and solid free-form fabrication systems. *Trends Biotechnol* **2004,** *22* (7), 354-62.

84. Nakamura, M.; Iwanaga, S.; Henmi, C.; Arai, K.; Nishiyama, Y., Biomatrices and biomaterials for future developments of bioprinting and biofabrication. *Biofabrication* **2010,** *2* (1), 014110.

85. Mironov, V.; Visconti, R. P.; Kasyanov, V.; Forgacs, G.; Drake, C. J.; Markwald, R. R., Organ printing: Tissue spheroids as building blocks. *Biomaterials* **2009,** *30* (12), 2164-2174.

86. Ferris, C. J.; Gilmore, K. J.; Beirne, S.; McCallum, D.; Wallace, G. G.; Panhuis, M. I. H., Bio-ink for on-demand printing of living cells. *Biomaterials Science* **2013,** *1* (2), 224-230.

87. Xu, T.; Binder, K. W.; Albanna, M. Z.; Dice, D.; Zhao, W. X.; Yoo, J. J.; Atala, A., Hybrid printing of mechanically and biologically improved constructs for cartilage tissue engineering applications. *Biofabrication* **2013,** *5* (1).

88. Wust, S.; Godla, M. E.; Muller, R.; Hofmann, S., Tunable hydrogel composite with two-step processing in combination with innovative hardware upgrade for cell-based three-dimensional bioprinting. *Acta Biomater* **2014,** *10* (2), 630-640.

89. Ozbolat, I. T.; Yu, Y., Bioprinting Toward Organ Fabrication: Challenges and Future Trends. *Ieee T Bio-Med Eng* **2013,** *60* (3), 691-699.

90. Dolatshahi-Pirouz, A.; Nikkhah, M.; Gaharwar, A. K.; Hashmi, B.; Guermani, E.; Aliabadi, H.; Camci-Unal, G.; Ferrante, T.; Foss, M.; Ingber, D. E.; Khademhosseini, A., A combinatorial cell-laden gel microarray for inducing osteogenic differentiation of human mesenchymal stem cells. *Sci. Rep.* **2014,** *4*.

91. Khademhosseini, A.; Langer, R., Microengineered hydrogels for tissue engineering. *Biomaterials* **2007,** *28* (34), 5087-92.

92. Moeller, H.-C.; Mian, M. K.; Shrivastava, S.; Chung, B. G.; Khademhosseini, A., A microwell array system for stem cell culture. *Biomaterials* **2008,** *29* (6), 752-763.

93. Murtuza, B.; Nichol, J. W.; Khademhosseini, A., Micro- and nanoscale control of the cardiac stem cell niche for tissue fabrication. *Tissue Eng. Pt. B* **2009,** *15* (4), 443-54.

94. Slaughter, B. V.; Khurshid, S. S.; Fisher, O. Z.; Khademhosseini, A.; Peppas, N. A., Hydrogels in regenerative medicine. *Adv. Mater.* **2009,** *21* (32-33), 3307-29.

95. Chen, G. P.; Sato, T.; Ushida, T.; Ochiai, N.; Tateishi, T., Tissue engineering of cartilage using a hybrid scaffold of synthetic polymer and collagen. *Tissue Eng. Pt. A* **2004,** *10* (3-4), 323-330.

96. Biotechnology and BioengineeringSchuurman, W.; Khristov, V.; Pot, M. W.; van Weeren, P. R.; Dhert, W. J. A.; Malda, J., Bioprinting of hybrid tissue constructs with tailorable mechanical properties. *Biofabrication* **2011,** *3* (2).

97. Kundu, J.; Shim, J. H.; Jang, J.; Kim, S. W.; Cho, D. W., An additive manufacturing-based PCL-alginate-chondrocyte bioprinted scaffold for cartilage tissue engineering. *J. Tissue Eng. Regen. Med.* **2013**.

98. Kim, K.; Dean, D.; Lu, A.; Mikos, A. G.; Fisher, J. P., Early osteogenic signal expression of rat bone marrow stromal cells is influenced by both hydroxyapatite nanoparticle content and initial cell seeding density in biodegradable nanocomposite scaffolds. *Acta Biomater.* **2011,** *7* (3), 1249-64.

99. Liu, H. N.; Webster, T. J., Enhanced biological and mechanical properties of well-dispersed nanophase ceramics in polymer composites: From 2D to 3D printed structures. *Mater. Sci. Eng. C* **2011,** *31* (2), 77-89.

100. Holmes, B., Zhang, L. In *Enhanced Human Bone Marrow Mesenchymal Stem Cell Functions in 3D Bioprinted Biologically Inspired Osteochondral Construct*, ASME IMECE, San Diego, CA, San Diego, CA, 2013; p 7.

101. Coleman, J. N.; Lotya, M.; O'Neill, A.; Bergin, S. D.; King, P. J.; Khan, U.; Young, K.; Gaucher, A.; De, S.; Smith, R. J., Two-dimensional nanosheets produced by liquid exfoliation of layered materials. *Science* **2011,** *331* (6017), 568-571.

102. Butler, S. Z.; Hollen, S. M.; Cao, L.; Cui, Y.; Gupta, J. A.; Gutiérrez, H. R.; Heinz, T. F.; Hong, S. S.; Huang, J.; Ismach, A. F., Progress, challenges, and opportunities in two-dimensional materials beyond graphene. *ACS nano* **2013,** *7* (4), 2898-2926.

103. Gupta, A.; Sakthivel, T.; Seal, S., Recent development in 2D materials beyond graphene. *Progress in Materials Science* **2015,** *73*, 44-126.

104. Chen, Y.; Tan, C. L.; Zhang, H.; Wang, L. Z., Two-dimensional graphene analogues for biomedical applications. *Chemical Society reviews* **2015,** *44* (9), 2681-2701.

105. Chimene, D.; Alge, D. L.; Gaharwar, A. K., Two-Dimensional Nanomaterials for Biomedical Applications: Emerging Trends and Future Prospects. *Adv Mater* **2015,** *27* (45), 7261-84.

106. Jiang, W.; Kim, B. Y. S.; Rutka, J. T.; Chan, W. C. W., Nanoparticle-mediated cellular response is size-dependent. *Nature Nanotechnology* **2008,** *3* (3), 145-150.

107. Kerativitayanan, P.; Carrow, J. K.; Gaharwar, A. K., Nanomaterials for Engineering Stem Cell Responses. *Adv Healthc Mater* **2015,** *4* (11), 1600-27.

108. Rauch, J.; Kolch, W.; Laurent, S.; Mahmoudi, M., Big signals from small particles: regulation of cell signaling pathways by nanoparticles. *Chemical reviews* **2013,** *113* (5), 3391-406.

109. Wang, Q.; Chen, B.; Cao, M.; Sun, J.; Wu, H.; Zhao, P.; Xing, J.; Yang, Y.; Zhang, X.; Ji, M.; Gu, N., Response of MAPK pathway to iron oxide nanoparticles in vitro treatment promotes osteogenic differentiation of hBMSCs. *Biomaterials* **2016,** *86*, 11-20.

110. Yi, C.; Liu, D.; Fong, C. C.; Zhang, J.; Yang, M., Gold nanoparticles promote osteogenic differentiation of mesenchymal stem cells through p38 MAPK pathway. *ACS nano* **2010,** *4* (11), 6439-48.

111. Eom, H. J.; Choi, J., Oxidative stress of CeO2 nanoparticles via p38-Nrf-2 signaling pathway in human bronchial epithelial cell, Beas-2B. *Toxicol Lett* **2009,** *187* (2), 77-83.

112. Wu, Y.; Zhu, R.; Zhou, Y.; Zhang, J.; Wang, W.; Sun, X.; Wu, X.; Cheng, L.; Zhang, J.; Wang, S., Layered double hydroxide nanoparticles promote self-renewal of mouse embryonic stem cells through the PI3K signaling pathway. *Nanoscale* **2015,** *7* (25), 11102-14.

113. Shendure, J., The beginning of the end for microarrays? *Nature methods* **2008,** *5* (7), 585-7.

114. Cloonan, N.; Forrest, A. R.; Kolle, G.; Gardiner, B. B.; Faulkner, G. J.; Brown, M. K.; Taylor, D. F.; Steptoe, A. L.; Wani, S.; Bethel, G.; Robertson, A. J.; Perkins, A. C.; Bruce, S. J.; Lee, C. C.; Ranade, S. S.; Peckham, H. E.; Manning, J. M.; McKernan, K. J.; Grimmond, S. M., Stem cell transcriptome profiling via massive-scale mRNA sequencing. *Nature methods* **2008,** *5* (7), 613-9.

115. Mortazavi, A.; Williams, B. A.; McCue, K.; Schaeffer, L.; Wold, B., Mapping and quantifying mammalian transcriptomes by RNA-Seq. *Nature methods* **2008,** *5* (7), 621-8.

116. Lucafo, M.; Gerdol, M.; Pallavicini, A.; Pacor, S.; Zorzet, S.; Da Ros, T.; Prato, M.; Sava, G., Profiling the molecular mechanism of fullerene cytotoxicity on tumor cells by RNA-seq. *Toxicology* **2013,** *314* (1), 183-92.

117. Dawson, J. I.; Oreffo, R. O., Clay: new opportunities for tissue regeneration and biomaterial design. *Adv Mater* **2013,** *25* (30), 4069-4086.

118. Ghadiri, M.; Chrzanowski, W.; Rohanizadeh, R., Biomedical applications of cationic clay minerals. *Rsc Adv* **2015,** *5* (37), 29467-29481.

119. Viseras, C.; Cerezo, P.; Sanchez, R.; Salcedo, I.; Aguzzi, C., Current challenges in clay minerals for drug delivery. *Appl Clay Sci* **2010,** *48* (3), 291-295.

120. Ruzicka, B.; Zaccarelli, E.; Zulian, L.; Angelini, R.; Sztucki, M.; Moussaid, A.; Narayanan, T.; Sciortino, F., Observation of empty liquids and equilibrium gels in a colloidal clay. *Nature materials* **2011,** *10* (1), 56-60.

121. Thompson, D. W.; Butterworth, J. T., The Nature of Laponite and Its Aqueous Dispersions. *Journal of Colloid and Interface Science* **1992,** *151* (1), 236-243.

122. Tawari, S. L.; Koch, D. L.; Cohen, C., Electrical double-layer effects on the Brownian diffusivity and aggregation rate of Laponite clay particles. *Journal of colloid and interface science* **2001,** *240* (1), 54-66.

123. Gaharwar, A. K.; Mihaila, S. M.; Swami, A.; Patel, A.; Sant, S.; Reis, R. L.; Marques, A. P.; Gomes, M. E.; Khademhosseini, A., Bioactive silicate nanoplatelets for osteogenic differentiation of human mesenchymal stem cells. *Adv Mater* **2013,** *25* (24), 3329-36.

124. Mihaila, S. M.; Gaharwar, A. K.; Reis, R. L.; Khademhosseini, A.; Marques, A. P.; Gomes, M. E., The osteogenic differentiation of SSEA-4 sub-population of human adipose derived stem cells using silicate nanoplatelets. *Biomaterials* **2014,** *35* (33), 9087-99.

125. Akhavan, O.; Ghaderi, E.; Akhavan, A., Size-dependent genotoxicity of graphene nanoplatelets in human stem cells. *Biomaterials* **2012,** *33* (32), 8017-8025.

126. Xavier, J. R.; Thakur, T.; Desai, P.; Jaiswal, M. K.; Sears, N.; Cosgriff-Hernandez, E.; Kaunas, R.; Gaharwar, A. K., Bioactive nanoengineered hydrogels for bone tissue engineering: a growth-factor-free approach. *ACS Nano* **2015,** *9* (3), 3109-18.

127. Dawson, J. I.; Kanczler, J. M.; Yang, X. B.; Attard, G. S.; Oreffo, R. O., Clay gels for the delivery of regenerative microenvironments. *Adv Mater* **2011,** *23* (29), 3304-3308.

128. Gaharwar, A. K.; Schexnailder, P. J.; Kline, B. P.; Schmidt, G., Assessment of using Laponite® cross-linked poly (ethylene oxide) for controlled cell adhesion and mineralization. *Acta Biomater* **2011,** *7* (2), 568-577.

129. Gaharwar, A. K.; Avery, R. K.; Assmann, A.; Paul, A.; McKinley, G. H.; Khademhosseini, A.; Olsen, B. D., Shear-thinning nanocomposite hydrogels for the treatment of hemorrhage. *ACS Nano* **2014,** *8* (10), 9833-42.

130. Purwada, A.; Jaiswal, M. K.; Ahn, H.; Nojima, T.; Kitamura, D.; Gaharwar, A. K.; Cerchietti, L.; Singh, A., Ex vivo engineered immune organoids for controlled germinal center reactions. *Biomaterials* **2015,** *63*, 24-34.

131. Paul, A.; Manoharan, V.; Krafft, D.; Assmann, A.; Uquillas, J. A.; Shin, S. R.; Hasan, A.; Hussain, M. A.; Memic, A.; Gaharwar, A. K., Nanoengineered biomimetic hydrogels for guiding human stem cell osteogenesis in three dimensional microenvironments. *Journal of Materials Chemistry B* **2016,** *4* (20), 3544-3554.

132. Peak, C. W.; Stein, J.; Gold, K. A.; Gaharwar, A. K., Nanoengineered Colloidal Inks for 3D Bioprinting. *Langmuir* **2017**, DOI: 10.1021/acs.langmuir.7b02540.

133. Wilson, S. A.; Cross, L. M.; Peak, C. W.; Gaharwar, A. K., Shear-Thinning and Thermo-Reversible Nanoengineered Inks for 3D Bioprinting. *ACS applied materials & interfaces* **2017,** *9* (50), 43449-43458.

134. AshaRani, P.; Low Kah Mun, G.; Hande, M. P.; Valiyaveettil, S., Cytotoxicity and genotoxicity of silver nanoparticles in human cells. *ACS nano* **2008,** *3* (2), 279-290.

135. Figueroa, J. A. L.; Stiner, C. A.; Radzyukevich, T. L.; Heiny, J. A., Metal ion transport quantified by ICP-MS in intact cells. *Scientific reports* **2016,** *6*, 20551.

136. Dobin, A.; Davis, C. A.; Schlesinger, F.; Drenkow, J.; Zaleski, C.; Jha, S.; Batut, P.; Chaisson, M.; Gingeras, T. R., STAR: ultrafast universal RNA-seq aligner. *Bioinformatics* **2013,** *29* (1), 15-21.

137. Anders, S.; Huber, W., Differential expression analysis for sequence count data. *Genome biology* **2010,** *11* (10), R106.

138. Supek, F.; Bošnjak, M.; Škunca, N.; Šmuc, T., REVIGO summarizes and visualizes long lists of gene ontology terms. *PloS one* **2011,** *6* (7), e21800.

139. Shannon, P.; Markiel, A.; Ozier, O.; Baliga, N. S.; Wang, J. T.; Ramage, D.; Amin, N.; Schwikowski, B.; Ideker, T., Cytoscape: a software environment for integrated models of biomolecular interaction networks. *Genome research* **2003,** *13* (11), 2498-2504.

140. Montojo, J.; Zuberi, K.; Rodriguez, H.; Kazi, F.; Wright, G.; Donaldson, S. L.; Morris, Q.; Bader, G. D., GeneMANIA Cytoscape plugin: fast gene function predictions on the desktop. *Bioinformatics* **2010,** *26* (22), 2927-2928.

141. Bindea, G.; Mlecnik, B.; Hackl, H.; Charoentong, P.; Tosolini, M.; Kirilovsky, A.; Fridman, W.-H.; Pagès, F.; Trajanoski, Z.; Galon, J., ClueGO: a Cytoscape plug-in to decipher functionally grouped gene ontology and pathway annotation networks. *Bioinformatics* **2009,** *25* (8), 1091-1093.

142. Huang, D. W.; Sherman, B. T.; Lempicki, R. A., Systematic and integrative analysis of large gene lists using DAVID bioinformatics resources. *Nature protocols* **2008,** *4* (1), 44.

143. Peirson, S. N.; Butler, J. N.; Foster, R. G., Experimental validation of novel and conventional approaches to quantitative real-time PCR data analysis. *Nucleic acids research* **2003,** *31* (14), e73-e73.

144. Gregory, C. A.; Gunn, W. G.; Peister, A.; Prockop, D. J., An Alizarin red-based assay of mineralization by adherent cells in culture: comparison with cetylpyridinium chloride extraction. *Analytical biochemistry* **2004,** *329* (1), 77-84.

145. Hühn, J.; Carrillo-Carrion, C.; Soliman, M. G.; Pfeiffer, C.; Valdeperez, D.; Masood, A.; Chakraborty, I.; Zhu, L.; Gallego, M.; Yue, Z., Selected standard protocols for the synthesis, phase transfer, and characterization of inorganic colloidal nanoparticles. *Chem Mater* **2016,** *29* (1), 399-461.

146. Jatav, S.; Joshi, Y. M., Chemical stability of Laponite in aqueous media. *Appl Clay Sci* **2014,** *97-98*, 72-77.

147. Pena, M. D.; Gottipati, A.; Tahiliani, S.; Neu-Baker, N. M.; Frame, M. D.; Friedman, A. J.; Brenner, S. A., Hyperspectral imaging of nanoparticles in biological samples: Simultaneous visualization and elemental identification. *Microsc Res Tech* **2016**.

148. Doyon, J. B.; Zeitler, B.; Cheng, J.; Cheng, A. T.; Cherone, J. M.; Santiago, Y.; Lee, A. H.; Vo, T. D.; Doyon, Y.; Miller, J. C.; Paschon, D. E.; Zhang, L.; Rebar, E. J.; Gregory, P. D.; Urnov, F. D.; Drubin, D. G., Rapid and efficient clathrin-mediated endocytosis revealed in genome-edited mammalian cells. *Nat Cell Biol* **2011,** *13* (3), 331-7.

149. Han, P.; Wu, C.; Xiao, Y., The effect of silicate ions on proliferation, osteogenic differentiation and cell signalling pathways (WNT and SHH) of bone marrow stromal cells. *Biomaterials Science* **2013,** *1* (4), 379-392.

150. Reffitt, D. M.; Ogston, N.; Jugdaohsingh, R.; Cheung, H. F.; Evans, B. A.; Thompson, R. P.; Powell, J. J.; Hampson, G. N., Orthosilicic acid stimulates collagen type 1 synthesis and osteoblastic differentiation in human osteoblast-like cells in vitro. *Bone* **2003,** *32* (2), 127-35.

151. Yoshizawa, S.; Brown, A.; Barchowsky, A.; Sfeir, C., Magnesium ion stimulation of bone marrow stromal cells enhances osteogenic activity, simulating the effect of magnesium alloy degradation. *Acta Biomater* **2014,** *10* (6), 2834-2842.

152. Clement-Lacroix, P.; Ai, M.; Morvan, F.; Roman-Roman, S.; Vayssiere, B.; Belleville, C.; Estrera, K.; Warman, M. L.; Baron, R.; Rawadi, G., Lrp5-independent activation of Wnt signaling by lithium chloride increases bone formation and bone mass in mice. *Proceedings of the National Academy of Sciences of the United States of America* **2005,** *102* (48), 17406-11.

153. Zhang, F.; Phiel, C. J.; Spece, L.; Gurvich, N.; Klein, P. S., Inhibitory phosphorylation of glycogen synthase kinase-3 (GSK-3) in response to lithium. Evidence for autoregulation of GSK-3. *The Journal of biological chemistry* **2003,** *278* (35), 33067-77.

154. Nel, A. E.; Madler, L.; Velegol, D.; Xia, T.; Hoek, E. M.; Somasundaran, P.; Klaessig, F.; Castranova, V.; Thompson, M., Understanding biophysicochemical interactions at the nano-bio interface. *Nat Mater* **2009,** *8* (7), 543-57.

155. Grzincic, E.; Yang, J.; Drnevich, J.; Falagan-Lotsch, P.; Murphy, C., Global transcriptomic analysis of model human cell lines exposed to surface-modified gold nanoparticles: the effect of surface chemistry. *Nanoscale* **2015,** *7* (4), 1349-1362.

156. Orecchioni, M.; Jasim, D. A.; Pescatori, M.; Manetti, R.; Fozza, C.; Sgarrella, F.; Bedognetti, D.; Bianco, A.; Kostarelos, K.; Delogu, L. G., Molecular and genomic impact of large and small lateral dimension graphene oxide sheets on human immune cells from healthy donors. *Advanced healthcare materials* **2016,** *5* (2), 276-287.

157. Albanese, A.; Tang, P. S.; Chan, W. C., The effect of nanoparticle size, shape, and surface chemistry on biological systems. *Annual review of biomedical engineering* **2012,** *14*, 1-16.

158. Liu, Z. J.; Zhuge, Y.; Velazquez, O. C., Trafficking and Differentiation of Mesenchymal Stem Cells. *Journal of cellular biochemistry* **2009,** *106* (6), 984-991.

159. Wennerberg, K.; Rossman, K. L.; Der, C. J., The Ras superfamily at a glance. *J Cell Sci* **2005,** *118* (5), 843-846.

160. Hutchison, M.; Berman, K. S.; Cobb, M. H., Isolation of TAO1, a protein kinase that activates MEKs in stress-activated protein kinase cascades. *Journal of Biological Chemistry* **1998,** *273* (44), 28625-28632.

161. Wang, F. S.; Wang, C. J.; Sheen-Chen, S. M.; Kuo, Y. R.; Chen, R. F.; Yang, K. D., Superoxide mediates shock wave induction of ERK-dependent osteogenic transcription factor (CBFA1) and mesenchymal cell differentiation toward osteoprogenitors. *The Journal of biological chemistry* **2002,** *277* (13), 10931-7.

162. Lai, Z. W.; Yan, Y.; Caruso, F.; Nice, E. C., Emerging techniques in proteomics for probing nano-bio interactions. *ACS nano* **2012,** *6* (12), 10438-48.

163. Cargnello, M.; Roux, P. P., Activation and function of the MAPKs and their substrates, the MAPK-activated protein kinases. *Microbiology and molecular biology reviews* **2011,** *75* (1), 50-83.

164. Song, L.; Webb, N. E.; Song, Y.; Tuan, R. S., Identification and functional analysis of candidate genes regulating mesenchymal stem cell self-renewal and multipotency. *Stem Cells* **2006,** *24* (7), 1707-18.

165. Rawlings, J. S.; Rosler, K. M.; Harrison, D. A., The JAK/STAT signaling pathway. *J Cell Sci* **2004,** *117* (Pt 8), 1281-3.

166. Clevers, H., Wnt/β-Catenin Signaling in Development and Disease. *Cell* **2006,** *127* (3), 469-480.

167. Cantley, L. C., The Phosphoinositide 3-Kinase Pathway. *Science* **2002,** *296* (5573), 1655-1657.

168. Zhang, D.; Liu, D.; Zhang, J.; Fong, C.; Yang, M., Gold nanoparticles stimulate differentiation and mineralization of primary osteoblasts through the ERK/MAPK signaling pathway. *Mater Sci Eng C Mater Biol Appl* **2014,** *42*, 70-7.

169. Hu, X.; Wang, H.; Liu, J.; Fang, X.; Tao, K.; Wang, Y.; Li, N.; Shi, J.; Wang, Y.; Ji, P.; Cai, W.; Bai, X.; Zhu, X.; Han, J.; Hu, D., The role of ERK and JNK signaling in connective tissue growth factor induced extracellular matrix protein production and scar formation. *Arch Dermatol Res* **2013,** *305* (5), 433-45.

170. Caro-Gonzalez, H. Y.; Nejsum, L. N.; Siemers, K. A.; Shaler, T. A.; Nelson, W. J.; Barth, A. I., Mitogen-activated protein kinase (MAPK/ERK) regulates adenomatous polyposis coli during growth-factor-induced cell extension. *J Cell Sci* **2012,** *125* (Pt 5), 1247-58.

171. Santos, S. D.; Verveer, P. J.; Bastiaens, P. I., Growth factor-induced MAPK network topology shapes Erk response determining PC-12 cell fate. *Nat Cell Biol* **2007,** *9* (3), 324-30.

172. Mansour, S. J.; Matten, W. T.; Hermann, A. S.; Candia, J. M.; Rong, S.; Fukasawa, K.; Vande Woude, G. F.; Ahn, N. G., Transformation of mammalian cells by constitutively active MAP kinase kinase. *Science* **1994,** *265* (5174), 966-70.

173. Yan, L.; Luo, H.; Gao, X.; Liu, K.; Zhang, Y., Vascular endothelial growth factor-induced expression of its receptors and activation of the MAPK signaling pathway during ovine oocyte maturation in vitro. *Theriogenology* **2012,** *78* (6), 1350-60.

174. Costa, P. M.; Fadeel, B., Emerging systems biology approaches in nanotoxicology: Towards a mechanism-based understanding of nanomaterial hazard and risk. *Toxicology and applied pharmacology* **2016,** *299*, 101-111.

175. Langer, R.; Vacanti, J. P., Tissue engineering. *Science* **1993,** *260* (5110), 920-6.

176. Lutolf, M.; Hubbell, J., Synthetic biomaterials as instructive extracellular microenvironments for morphogenesis in tissue engineering. *Nature biotechnology* **2005,** *23* (1), 47-55.

177. Makris, E. A.; Gomoll, A. H.; Malizos, K. N.; Hu, J. C.; Athanasiou, K. A., Repair and tissue engineering techniques for articular cartilage. *Nature Reviews Rheumatology* **2014**.

178. Nikkhah, M.; Edalat, F.; Manoucheri, S.; Khademhosseini, A., Engineering microscale topographies to control the cell–substrate interface. *Biomaterials* **2012,** *33* (21), 5230-5246.

179. Zorlutuna, P.; Annabi, N.; Camci-Unal, G.; Nikkhah, M.; Cha, J. M.; Nichol, J. W.; Manbachi, A.; Bae, H.; Chen, S.; Khademhosseini, A., Microfabricated biomaterials for engineering 3D tissues. *Advanced materials* **2012,** *24* (14), 1782-1804.

180. Aguado, B. A.; Mulyasasmita, W.; Su, J.; Lampe, K. J.; Heilshorn, S. C., Improving viability of stem cells during syringe needle flow through the design of hydrogel cell carriers. *Tissue engineering. Part A* **2012,** *18* (7-8), 806-15.

181. Kloxin, A. M.; Kloxin, C. J.; Bowman, C. N.; Anseth, K. S., Mechanical Properties of Cellularly Responsive Hydrogels and Their Experimental Determination. *Adv. Mater.* **2010,** *22* (31), 3484-3494.

182. Sant, S.; Hancock, M. J.; Donnelly, J. P.; Iyer, D.; Khademhosseini, A., Biomimetic gradient hydrogels for tissue engineering. *The Canadian journal of chemical engineering* **2010,** *88* (6), 899-911.

183. Burdick, J. A.; Murphy, W. L., Moving from static to dynamic complexity in hydrogel design. *Nature communications* **2012,** *3*, 1269.

184. Alge, D. L.; Anseth, K. S., Bioactive hydrogels: Lighting the way. *Nature materials* **2013,** *12* (11), 950-952.

185. Oliveira, J. M.; Sousa, R. A.; Kotobuki, N.; Tadokoro, M.; Hirose, M.; Mano, J. F.; Reis, R. L.; Ohgushi, H., The osteogenic differentiation of rat bone marrow stromal cells cultured with dexamethasone-loaded carboxymethylchitosan/poly(amidoamine) dendrimer nanoparticles. *Biomaterials* **2009,** *30* (5), 804-813.

186. Schuldiner, M.; Yanuka, O.; Itskovitz-Eldor, J.; Melton, D. A.; Benvenisty, N., Effects of eight growth factors on the differentiation of cells derived from human embryonic stem cells. *Proc. Natl. Acad. Sci. U. S. A.* **2000,** *97* (21), 11307-11312.

187. Paul, A., Nanocomposite hydrogels: an emerging biomimetic platform for myocardial therapy and tissue engineering. *Nanomedicine* **2015,** *10* (9), 1371-1374.

188. Carrow, J. K.; Gaharwar, A. K., Bioinspired Polymeric Nanocomposites for Regenerative Medicine. *Macromolecular Chemistry and Physics* **2015,** *216* (3), 248−264.

189. Kerativitayanan, P.; Carrow, J. K.; Gaharwar, A. K., Nanomaterials for Engineering Stem Cell Responses. *Advanced healthcare materials* **2015,** *4* (11), 1600–1627.

190. Goenka, S.; Sant, V.; Sant, S., Graphene-based nanomaterials for drug delivery and tissue engineering. *Journal of Controlled Release* **2014,** *173,* 75-88.

191. Chimene, D.; Alge, D. L.; Gaharwar, A. K., Two-Dimensional Nanomaterials for Biomedical Applications: Emerging Trends and Future Prospects. *Advanced Materials* **2015,** *27* (45), 7261–7284.

192. Paul, A.; Hasan, A.; Kindi, H. A.; Gaharwar, A. K.; Rao, V. T.; Nikkhah, M.; Shin, S. R.; Krafft, D.; Dokmeci, M. R.; Shum-Tim, D., Injectable graphene oxide/hydrogel-based angiogenic gene delivery system for vasculogenesis and cardiac repair. *ACS nano* **2014,** *8* (8), 8050-8062.

193. Kumar, S.; Raj, S.; Sarkar, K.; Chatterjee, K., Engineering a multi-biofunctional composite using poly(ethylenimine) decorated graphene oxide for bone tissue regeneration. *Nanoscale* **2016,** *8* (12), 6820-6836.

194. Gaharwar, A. K.; Avery, R. K.; Assmann, A.; Paul, A.; McKinley, G. H.; Khademhosseini, A.; Olsen, B. D., Shear-thinning nanocomposite hydrogels for the treatment of hemorrhage. *ACS nano* **2014,** *8* (10), 9833-9842.

195. Xavier, J. R.; Thakur, T.; Desai, P.; Jaiswal, M. K.; Sears, N.; Cosgriff-Hernandez, E.; Kaunas, R.; Gaharwar, A. K., Bioactive Nanoengineered Hydrogels for Bone Tissue Engineering: A Growth-Factor-Free Approach. *ACS nano* **2015,** *9* (3), 3109-3118.

196. Peak, C.; Carrow, J.; Thakur, A.; Singh, A.; Gaharwar, A., Elastomeric Cell-Laden Nanocomposite Microfibers for Engineering Complex Tissues. *Cel. Mol. Bioeng.* **2015,** *8* (3), 404-415.

197. Hennink, W. E.; van Nostrum, C. F., Novel crosslinking methods to design hydrogels. *Advanced Drug Delivery Reviews* **2002,** *54* (1), 13-36.

198. Gaharwar, A. K.; Mihaila, S. M.; Swami, A.; Patel, A.; Sant, S.; Reis, R. L.; Marques, A. P.; Gomes, M. E.; Khademhosseini, A., Bioactive silicate nanoplatelets for osteogenic differentiation of human mesenchymal stem cells. *Advanced Materials* **2013,** *25* (24), 3329-3336.

199. Ruzicka, B.; Zaccarelli, E.; Zulian, L.; Angelini, R.; Sztucki, M.; Moussaïd, A.; Narayanan, T.; Sciortino, F., Observation of empty liquids and equilibrium gels in a colloidal clay. *Nature materials* **2011,** *10* (1), 56-60.

200. Waters, R.; Pacelli, S.; Maloney, R.; Medhi, I.; Ahmed, R. P. H.; Paul, A., Stem cell secretome-rich nanoclay hydrogel: a dual action therapy for cardiovascular regeneration. *Nanoscale* **2016**.

201. Campo, V. L.; Kawano, D. F.; da Silva, D. B.; Carvalho, I., Carrageenans: Biological properties, chemical modifications and structural analysis–A review. *Carbohydrate Polymers* **2009,** *77* (2), 167-180.

202. Li, L.; Ni, R.; Shao, Y.; Mao, S., Carrageenan and its applications in drug delivery. *Carbohydrate polymers* **2014,** *103*, 1-11.

203. Venkatesan, J.; Lowe, B.; Anil, S.; Manivasagan, P.; Kheraif, A. A. A.; Kang, K.-H.; Kim, S.-K., Seaweed polysaccharides and their potential biomedical applications. *Starch - Stärke* **2015,** *67* (5-6), 381-390.

204. Hermansson, A.-M.; Eriksson, E.; Jordansson, E., Effects of potassium, sodium and calcium on the microstructure and rheological behaviour of kappa-carrageenan gels. *Carbohydrate Polymers* **1991,** *16* (3), 297-320.

205. Peak, C. W.; Stein, J.; Gold, K. A.; Gaharwar, A. K., Nanoengineered Colloidal Inks for 3D Bioprinting. *Langmuir : the ACS journal of surfaces and colloids* **2018,** *34* (3), 917-925.

206. Mangione, M. R.; Giacomazza, D.; Bulone, D.; Martorana, V.; Cavallaro, G.; San Biagio, P. L., K(+) and Na(+) effects on the gelation properties of kappa-Carrageenan. *Biophysical chemistry* **2005,** *113* (2), 129-35.

207. Trius, A.; Sebranek, J. G., Carrageenans and their use in meat products. *Critical reviews in food science and nutrition* **1996,** *36* (1-2), 69-85.

208. Moon, S. H.; Parulekar, S. J., Characterization of kappa-carrageenan gels used for immobilization of Bacillus firmus. *Biotechnology progress* **1991,** *7* (6), 516-25.

209. Piculell, L.; Borgstrom, J.; Chronakis, I. S.; Quist, P. O.; Viebke, C., Organisation and association of kappa-carrageenan helices under different salt conditions. *International journal of biological macromolecules* **1997,** *21* (1-2), 141-53.

210. Mihaila, S. M.; Popa, E. G.; Reis, R. L.; Marques, A. P.; Gomes, M. E., Fabrication of Endothelial Cell-Laden Carrageenan Microfibers for Microvascularized Bone Tissue Engineering Applications. *Biomacromolecules* **2014,** *15* (8), 2849-2860.

211. Murphy, W. L.; McDevitt, T. C.; Engler, A. J., Materials as stem cell regulators. *Nature materials* **2014,** *13* (6), 547-557.

212. Engler, A. J.; Sen, S.; Sweeney, H. L.; Discher, D. E., Matrix elasticity directs stem cell lineage specification. *Cell* **2006,** *126* (4), 677-689.

213. Jaiswal, M. K.; Xavier, J. R.; Carrow, J. K.; Desai, P.; Alge, D.; Gaharwar, A. K., Mechanically Stiff Nanocomposite Hydrogels at Ultralow Nanoparticle Content. *ACS Nano* **2016,** *10* (1), 246–256.

214. Mihaila, S. M.; Gaharwar, A. K.; Reis, R. L.; Marques, A. P.; Gomes, M. E.; Khademhosseini, A., Photocrosslinkable Kappa-Carrageenan Hydrogels for Tissue Engineering Applications. *Advanced Healthcare Materials* **2013,** *2* (6), 895-907.

215. Thakur, A.; Jaiswal, M. K.; Peak, C. W.; Carrow, J. K.; Gentry, J.; Dolatshahi-Pirouz, A.; Gaharwar, A. K., Injectable shear-thinning nanoengineered hydrogels for stem cell delivery. *Nanoscale* **2016,** *8* (24), 12362-72.

216. Schmidt, G.; Nakatani, A. I.; Han, C. C., Rheology and flow-birefringence from viscoelastic polymer-clay solutions. *Rheol Acta* **2002,** *41* (1-2), 45-54.

217. Huang, M. H.; Yang, M. C., Swelling and biocompatibility of sodium alginate/poly(gamma-glutamic acid) hydrogels. *Polym Advan Technol* **2010,** *21* (8), 561-567.

218. Habib, A.; Sathish, V.; Mallik, S.; Khoda, B., 3D Printability of Alginate-Carboxymethyl Cellulose Hydrogel. *Materials (Basel)* **2018,** *11* (3).

219. Padmavathi, N. C.; Chatterji, P. R., Structural characteristics and swelling behavior of poly(ethylene glycol) diacrylate hydrogels. *Macromolecules* **1996,** *29* (6), 1976-1979.

220. Peak, C. W.; Carrow, J. K.; Thakur, A.; Singh, A.; Gaharwar, A. K., Elastomeric Cell-Laden Nanocomposite Microfibers for Engineering Complex Tissues. *Cel. Mol. Bioeng.* **2015,** *8* (3), 404-415.

221. Thakur, T.; Xavier, J. R.; Cross, L.; Jaiswal, M. K.; Mondragon, E.; Kaunas, R.; Gaharwar, A. K., Photocrosslinkable and Elastomeric Hydrogels for Bone Regeneration. *Journal of Biomedical Materials Research Part A* **2016,** *104* (4), 879–888.

222. Popa, E.; Reis, R.; Gomes, M., Chondrogenic phenotype of different cells encapsulated in κ-carrageenan hydrogels for cartilage regeneration strategies. *Biotechnology and applied biochemistry* **2012,** *59* (2), 132-141.

223. Popa, E. G.; Caridade, S. G.; Mano, J. F.; Reis, R. L.; Gomes, M. E., Chondrogenic potential of injectable κ-carrageenan hydrogel with encapsulated adipose stem cells for cartilage tissue-engineering applications. *Journal of tissue engineering and regenerative medicine* **2015,** *9* (5), 550-563.

224. Chimene, D.; Alge, D. L.; Gaharwar, A. K., Two-Dimensional Nanomaterials for Biomedical Applications: Emerging Trends and Future Prospects. *Adv. Mater.* **2015,** *27* (45), 7261–7284.

225. Chhowalla, M.; Shin, H. S.; Eda, G.; Li, L.-J.; Loh, K. P.; Zhang, H., The chemistry of two-dimensional layered transition metal dichalcogenide nanosheets. *Nat. Chem.* **2013,** *5* (4), 263-275.

226. Liu, T.; Wang, C.; Gu, X.; Gong, H.; Cheng, L.; Shi, X.; Feng, L.; Sun, B.; Liu, Z., Drug Delivery with PEGylated MoS2 Nano-sheets for Combined Photothermal and Chemotherapy of Cancer. *Adv. Mater.* **2014,** *26* (21), 3433-3440.

227. Chou, S. S.; Kaehr, B.; Kim, J.; Foley, B. M.; De, M.; Hopkins, P. E.; Huang, J.; Brinker, C. J.; Dravid, V. P., Chemically Exfoliated MoS2 as Near-Infrared Photothermal Agents. *Angew. Chem. Int. Ed.* **2013,** *125* (15), 4254-4258.

228. Late, D. J.; Huang, Y.-K.; Liu, B.; Acharya, J.; Shirodkar, S. N.; Luo, J.; Yan, A.; Charles, D.; Waghmare, U. V.; Dravid, V. P.; Rao, C. N. R., Sensing Behavior of Atomically Thin-Layered MoS2 Transistors. *ACS nano* **2013,** *7* (6), 4879-4891.

229. RadisavljevicB; RadenovicA; BrivioJ; GiacomettiV; KisA, Single-layer MoS2 transistors. *Nat. Nano.* **2011,** *6* (3), 147-150.

230. Jin, K.; Xie, L. M.; Tian, Y.; Liu, D. M., Au-Modified Monolayer MoS2 Sensor for DNA Detection. *J Phys Chem C* **2016,** *120* (20), 11204-11209.

231. Nguyen, E. P.; Carey, B. J.; Ou, J. Z.; van Embden, J.; Della Gaspera, E.; Chrimes, A. F.; Spencer, M. J. S.; Zhuiykov, S.; Kalantar-zadeh, K.; Daeneke, T., Electronic Tuning of 2D MoS2 through Surface Functionalization. *Adv Mater* **2015,** *27* (40), 6225-6229.

232. Frindt, R. F., Single Crystals of Mos2 Several Molecular Layers Thick. *J Appl Phys* **1966,** *37* (4), 1928-&.

233. Joensen, P.; Frindt, R. F.; Morrison, S. R., Single-Layer Mos2. *Mater Res Bull* **1986,** *21* (4), 457-461.

234. Schumacher, A.; Scandella, L.; Kruse, N.; Prins, R., Single-Layer Mos2 on Mica - Studies by Means of Scanning Force Microscopy. *Surf Sci* **1993,** *289* (1-2), L595-L598.

235. Wan, J. Y.; Lacey, S. D.; Dai, J. Q.; Bao, W. Z.; Fuhrer, M. S.; Hu, L. B., Tuning two-dimensional nanomaterials by intercalation: materials, properties and applications. *Chemical Society reviews* **2016,** *45* (24), 6742-6765.

236. Zhang, H.; Lu, S. B.; Zheng, J.; Du, J.; Wen, S. C.; Tang, D. Y.; Loh, K. P., Molybdenum disulfide (MoS2) as a broadband saturable absorber for ultra-fast photonics. *Optics Express* **2014,** *22* (6), 7249-7260.

237. Mieda, E.; Azumi, R.; Shimada, S.; Tanaka, M.; Shimizu, T.; Ando, A., Nanoprobe characterization of MoS2 nanosheets fabricated by Li-intercalation. *Jpn J Appl Phys* **2015,** *54* (8).

238. Yuwen, L.; Yu, H.; Yang, X.; Zhou, J.; Zhang, Q.; Zhang, Y.; Luo, Z.; Su, S.; Wang, L., Rapid preparation of single-layer transition metal dichalcogenide nanosheets via ultrasonication enhanced lithium intercalation. *Chemical communications* **2016,** *52* (3), 529-32.

239. Shanmuganathan, K.; Capadona, J. R.; Rowan, S. J.; Weder, C., Stimuli-responsive mechanically adaptive polymer nanocomposites. *ACS applied materials & interfaces* **2010,** *2* (1), 165-74.

240. Ahn, S.; Lee, S. J., Nanoparticle role on the repeatability of stimuli-responsive nanocomposites. *Scientific reports* **2014,** *4*, 6624.

241. Kumar, S.; Chatterjee, K., Comprehensive Review on the Use of Graphene-Based Substrates for Regenerative Medicine and Biomedical Devices. *ACS applied materials & interfaces* **2016,** *8* (40), 26431-26457.

242. O'Brien, C. M.; Zhang, L. G., Graphene Nanoplatelet Laden Hydrogel for Efficient Electrical Stimulation and Neural Regeneration. *Tissue Eng Pt A* **2014,** *20*, S103-S103.

243. Choi, W.; Choudhary, N.; Han, G. H.; Park, J.; Akinwande, D.; Lee, Y. H., Recent development of two-dimensional transition metal dichalcogenides and their applications. *Materials Today* **2017,** *20* (3), 116-130.

244. Reina, G.; Gonzalez-Dominguez, J. M.; Criado, A.; Vazquez, E.; Bianco, A.; Prato, M., Promises, facts and challenges for graphene in biomedical applications. *Chemical Society reviews* **2017,** *46* (15), 4400-4416.

245. Teo, W. Z.; Chng, E. L. K.; Sofer, Z.; Pumera, M., Cytotoxicity of Exfoliated Transition-Metal Dichalcogenides (MoS2, WS2, and WSe2) is Lower Than That of Graphene and its Analogues. *Chem-Eur J* **2014,** *20* (31), 9627-9632.

246. Appel, J. H.; Li, D. O.; Podlevsky, J. D.; Debnath, A.; Green, A. A.; Wang, Q. H.; Chae, J., Low Cytotoxicity and Genotoxicity of Two-Dimensional MoS2 and WS2. *Acs Biomater Sci Eng* **2016,** *2* (3), 361-367.

247. Chhowalla, M.; Shin, H. S.; Eda, G.; Li, L. J.; Loh, K. P.; Zhang, H., The chemistry of two-dimensional layered transition metal dichalcogenide nanosheets. *Nat Chem* **2013,** *5* (4), 263-75.

248. Eda, G.; Yamaguchi, H.; Voiry, D.; Fujita, T.; Chen, M.; Chhowalla, M., Photoluminescence from chemically exfoliated MoS2. *Nano letters* **2011,** *11* (12), 5111-6.

249. Gasymov, O. K.; Glasgow, B. J., ANS fluorescence: potential to augment the identification of the external binding sites of proteins. *Biochimica et biophysica acta* **2007,** *1774* (3), 403-11.

250. Radisavljevic, B.; Radenovic, A.; Brivio, J.; Giacometti, V.; Kis, A., Single-layer MoS2 transistors. *Nat Nanotechnol* **2011,** *6* (3), 147-50.

251. Cheng, P.; Sun, K.; Hu, Y. H., Memristive Behavior and Ideal Memristor of 1T Phase MoS2 Nanosheets. *Nano letters* **2016,** *16* (1), 572-6.

252. Rejman, J.; Oberle, V.; Zuhorn, I. S.; Hoekstra, D., Size-dependent internalization of particles via the pathways of clathrin- and caveolae-mediated endocytosis. *The Biochemical journal* **2004,** *377* (Pt 1), 159-69.

253. Fleischer, C. C.; Payne, C. K., Secondary structure of corona proteins determines the cell surface receptors used by nanoparticles. *The journal of physical chemistry. B* **2014,** *118* (49), 14017-26.

254. Shang, L.; Nienhaus, K.; Nienhaus, G. U., Engineered nanoparticles interacting with cells: size matters. *J Nanobiotechnology* **2014,** *12*, 5.

255. Zhang, S.; Li, J.; Lykotrafitis, G.; Bao, G.; Suresh, S., Size-Dependent Endocytosis of Nanoparticles. *Adv Mater* **2009,** *21*, 419-424.

256. Wang, Z.; von dem Bussche, A.; Qiu, Y.; Valentin, T. M.; Gion, K.; Kane, A. B.; Hurt, R. H., Chemical Dissolution Pathways of MoS2 Nanosheets in Biological and Environmental Media. *Environmental science & technology* **2016,** *50* (13), 7208-17.

257. Ding, D.; Li, L.; Song, Y.; Du, G.; Wei, X.; Cao, Y., [MAPK-ERK1/2 signaling pathway regulates osteogenic gene expression in rat osteoblasts in vitro]. *Nan Fang Yi Ke Da Xue Xue Bao* **2013,** *33* (10), 1432-6.

258. Gong, X.; Luo, T.; Deng, P.; Liu, Z.; Xiu, J.; Shi, H.; Jiang, Y., Stress-induced interaction between p38 MAPK and HSP70. *Biochemical and biophysical research communications* **2012,** *425* (2), 357-62.

259. Li, C. H.; Sunderic, K.; Nicoll, S. B.; Wang, S. H., Downregulation of Heat Shock Protein 70 Impairs Osteogenic and Chondrogenic Differentiation in Human Mesenchymal Stem Cells. *Scientific reports* **2018,** *8*.

260. Chen, E.; Xue, D.; Zhang, W.; Lin, F.; Pan, Z., Extracellular heat shock protein 70 promotes osteogenesis of human mesenchymal stem cells through activation of the ERK signaling pathway. *FEBS letters* **2015,** *589* (24 Pt B), 4088-96.

261. Li, C.; Sunderic, K.; Nicoll, S. B.; Wang, S., Downregulation of Heat Shock Protein 70 Impairs Osteogenic and Chondrogenic Differentiation in Human Mesenchymal Stem Cells. *Scientific reports* **2018,** *8* (1), 553.

262. Li, Y.; Lu, W.; Huang, Q.; Huang, M.; Li, C.; Chen, W., Copper sulfide nanoparticles for photothermal ablation of tumor cells. *Nanomedicine* **2010,** *5* (8), 1161-71.

263. Feng, W.; Chen, L.; Qin, M.; Zhou, X.; Zhang, Q.; Miao, Y.; Qiu, K.; Zhang, Y.; He, C., Flower-like PEGylated MoS2 nanoflakes for near-infrared photothermal cancer therapy. *Scientific reports* **2015,** *5*, 17422.

264. Yin, W.; Yan, L.; Yu, J.; Tian, G.; Zhou, L.; Zheng, X.; Zhang, X.; Yong, Y.; Li, J.; Gu, Z.; Zhao, Y., High-throughput synthesis of single-layer MoS2 nanosheets as a near-infrared photothermal-triggered drug delivery for effective cancer therapy. *ACS nano* **2014,** *8* (7), 6922-33.

265. Voiry, D.; Goswami, A.; Kappera, R.; SilvaCecilia de Carvalho Castro, e.; Kaplan, D.; Fujita, T.; Chen, M.; Asefa, T.; Chhowalla, M., Covalent functionalization of monolayered transition metal dichalcogenides by phase engineering. *Nat. Chem.* **2015,** *7* (1), 45-49.

266. Chou, S. S.; Sai, N.; Lu, P.; Coker, E. N.; Liu, S.; Artyushkova, K.; Luk, T. S.; Kaehr, B.; Brinker, C. J., Understanding catalysis in a multiphasic two-dimensional transition metal dichalcogenide. *Nat. Commun.* **2015,** *6*.

267. Nicolosi, V.; Chhowalla, M.; Kanatzidis, M. G.; Strano, M. S.; Coleman, J. N., Liquid Exfoliation of Layered Materials. *Science* **2013,** *340* (6139).

268. Nguyen, E. P.; Carey, B. J.; Ou, J. Z.; van Embden, J.; Gaspera, E. D.; Chrimes, A. F.; Spencer, M. J. S.; Zhuiykov, S.; Kalantar-zadeh, K.; Daeneke, T., Electronic Tuning of 2D MoS2 through Surface Functionalization. *Adv. Mater.* **2015,** *27* (40), 6225-6229.

269. Voiry, D.; Yang, J.; Chhowalla, M., Recent Strategies for Improving the Catalytic Activity of 2D TMD Nanosheets Toward the Hydrogen Evolution Reaction. *Adv. Mater.* **2016,** *28* (29), 6197–6206.

270. Hu, Z.; Wang, L.; Zhang, K.; Wang, J.; Cheng, F.; Tao, Z.; Chen, J., MoS2 Nanoflowers with Expanded Interlayers as High-Performance Anodes for Sodium-Ion Batteries. *Angew. Chem. Int. Ed.* **2014,** *126* (47), 13008-13012.

271. Maitra, U.; Gupta, U.; De, M.; Datta, R.; Govindaraj, A.; Rao, C. N. R., Highly Effective Visible-Light-Induced H2 Generation by Single-Layer 1T-MoS2 and a Nanocomposite of Few-Layer 2H-MoS2 with Heavily Nitrogenated Graphene. *Angew. Chem. Int. Ed.* **2013,** *52* (49), 13057-13061.

272. Lee, D. U.; Fu, J.; Park, M. G.; Liu, H.; Ghorbani Kashkooli, A.; Chen, Z., Self-Assembled NiO/Ni(OH)2 Nanoflakes as Active Material for High-Power and High-Energy Hybrid Rechargeable Battery. *Nano Lett.* **2016,** *16* (3), 1794–1802.

273. Ye, G.; Gong, Y.; Lin, J.; Li, B.; He, Y.; Pantelides, S. T.; Zhou, W.; Vajtai, R.; Ajayan, P. M., Defects Engineered Monolayer MoS2 for Improved Hydrogen Evolution Reaction. *Nano Lett.* **2016,** *16* (2), 1097-1103.

274. Fairbanks, B. D.; Singh, S. P.; Bowman, C. N.; Anseth, K. S., Photodegradable, Photoadaptable Hydrogels via Radical-Mediated Disulfide Fragmentation Reaction. *Macromolecules* **2011,** *44* (8), 2444-2450.

275. Chou, S. S.; De, M.; Kim, J.; Byun, S.; Dykstra, C.; Yu, J.; Huang, J.; Dravid, V. P., Ligand conjugation of chemically exfoliated MoS2. *J. Am. Chem. Soc* **2013,** *135* (12), 4584-4587.

276. Kim, J.-S.; Yoo, H.-W.; Choi, H. O.; Jung, H.-T., Tunable volatile organic compounds sensor by using thiolated ligand conjugation on MoS2. *Nano Lett.* **2014,** *14* (10), 5941-5947.

277. Presolski, S.; Pumera, M., Covalent functionalization of MoS 2. *Mater. Today* **2016,** *19* (3), 140-145.

278. Feng, W.; Chen, L.; Qin, M.; Zhou, X.; Zhang, Q.; Miao, Y.; Qiu, K.; Zhang, Y.; He, C., Flower-like PEGylated MoS2 nanoflakes for near-infrared photothermal cancer therapy. *Sci. Rep.* **2015,** *5*, 17422.

279. Xie, J.; Zhang, H.; Li, S.; Wang, R.; Sun, X.; Zhou, M.; Zhou, J.; Lou, X. W.; Xie, Y., Defect-Rich MoS2 Ultrathin Nanosheets with Additional Active Edge Sites for Enhanced Electrocatalytic Hydrogen Evolution. *Adv. Mater.* **2013,** *25* (40), 5807-5813.

280. Tongay, S.; Varnoosfaderani, S. S.; Appleton, B. R.; Wu, J.; Hebard, A. F., Magnetic properties of MoS2: Existence of ferromagnetism. *Appl. Phys. Lett.* **2012,** *101* (12), 123105.

281. Cheng, P.; Sun, K.; Hu, Y. H., Memristive Behavior and Ideal Memristor of 1T Phase MoS2 Nanosheets. *Nano Lett.* **2016,** *16* (1), 572-576.

282. Gaharwar, A. K.; Mihaila, S. M.; Swami, A.; Patel, A.; Sant, S.; Reis, R. L.; Marques, A. P.; Gomes, M. E.; Khademhosseini, A., Bioactive silicate nanoplatelets for osteogenic differentiation of human mesenchymal stem cells. *Adv. Mater.* **2013,** *25* (24), 3329-3336.

283. Discher, D. E.; Smith, L.; Cho, S.; Colasurdo, M.; Garcia, A. J.; Safran, S., Matrix Mechanosensing: From Scaling Concepts in 'Omics Data to Mechanisms in the Nucleus, Regeneration, and Cancer. *Annu Rev Biophys* **2017,** *46*, 295-315.

284. Kloprogge, J. T.; Komarneni, S.; Amonette, J. E., Synthesis of smectite clay minerals: A critical review. *Clay Clay Miner* **1999,** *47* (5), 529-554.

APPENDIX A

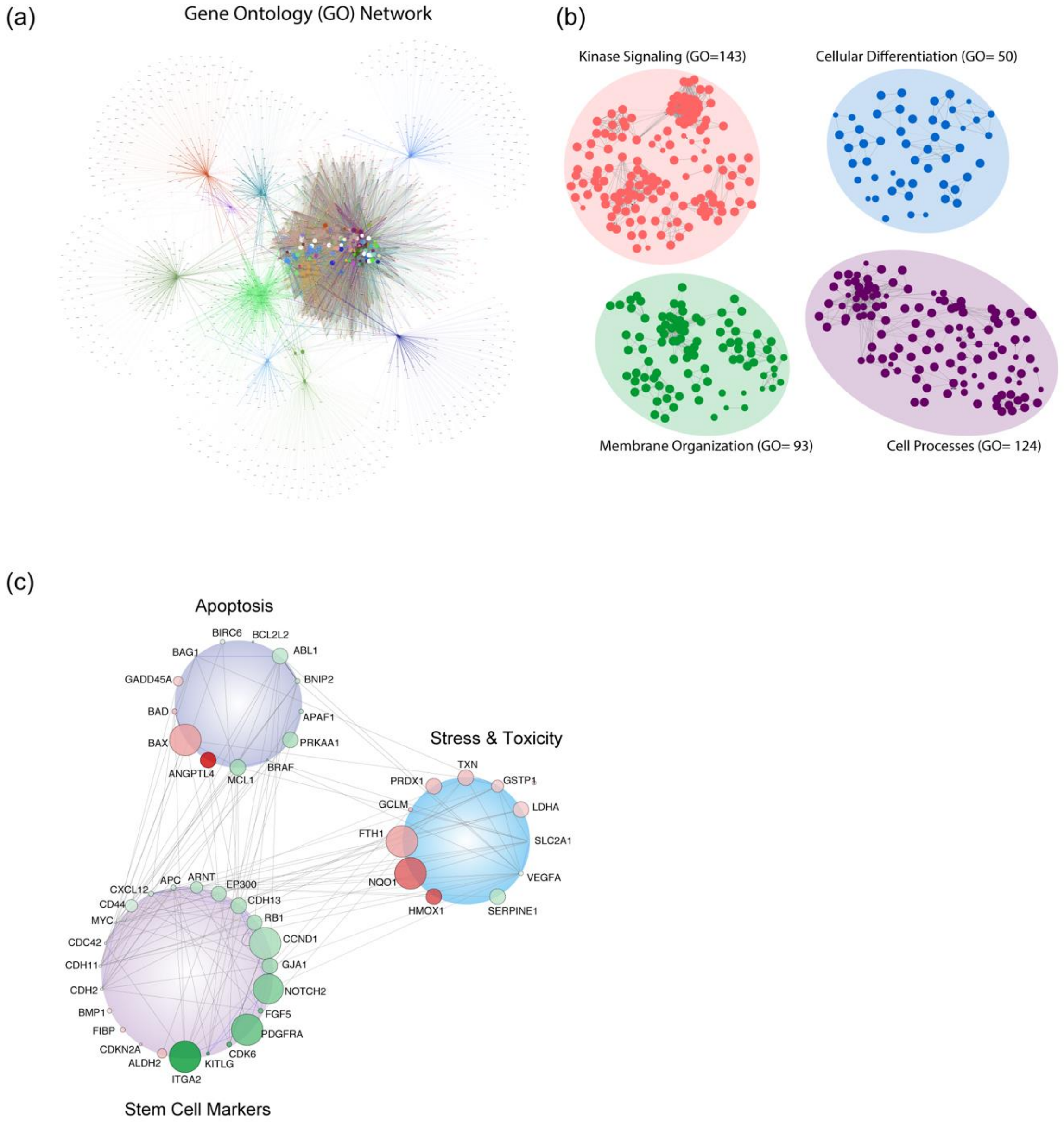

Figure A.1: (a) Network of GO terms and expressed gene clusters around each respective correlating term illustrating highly interconnected stimulation with nanosilicates; (b) GO terms could be subsequently divided into four primary cellular systems including basic processes, membrane organization, kinase signaling, and differentiation responses; (c) gene network displaying interconnected genetic targets after nanosilicate treatment with high degrees of expression and statistical significance (red—upregulated, green—downregulated; size increases with significance).

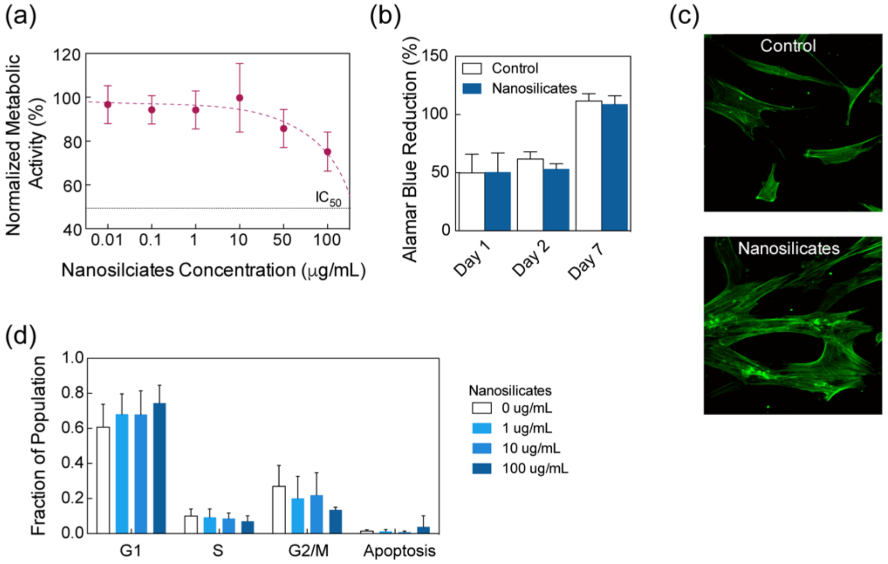

Figure A.2: Nanosilicate effect on cellular processes. (a) Metabolic activity, assessed via MTT assay, remained unaffected by nanosilicate introduction at bioactive concentrations. Minimal effect of nanosilicates was observed on cell health monitor via (b) Alamar blue assay and (d) cell cycle analysis over multiple concentrations. (c) Effect of nanosilicate on cytoskeletal organization.

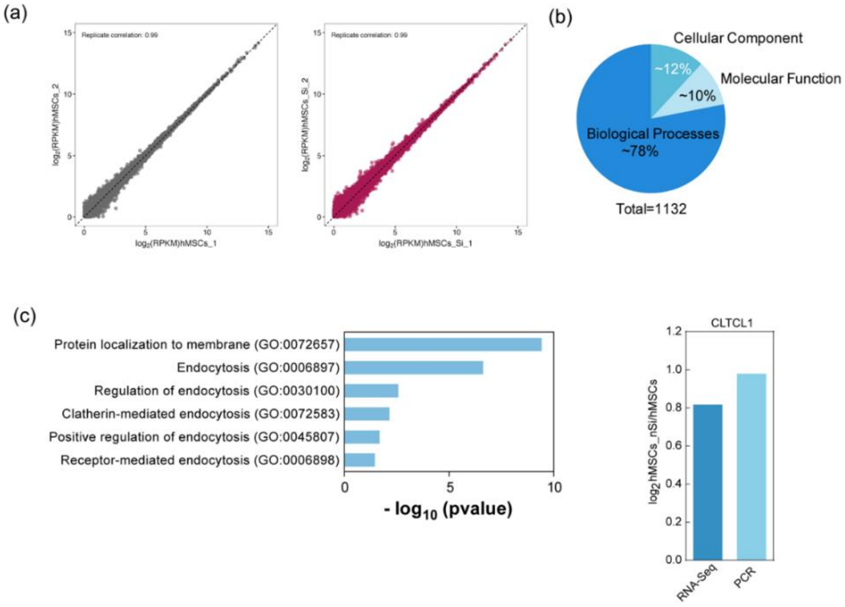

Figure A.3: (a) Replicate variation of RNA-se samples. Correlation for replicates among untreated and treated populations, respectively, indicate high degrees of reliability and consistency between tested samples. (b) Broad grouping of GO terms into three main groups: biological processes, cellular component, and molecular function. (c) GO terms specific to endocytosis process. (d) PCR validation of RNA-seq specific to a gene controlling clathrin machinery (clathrin heavy chain like 1; CLTCL1).

APPENDIX B

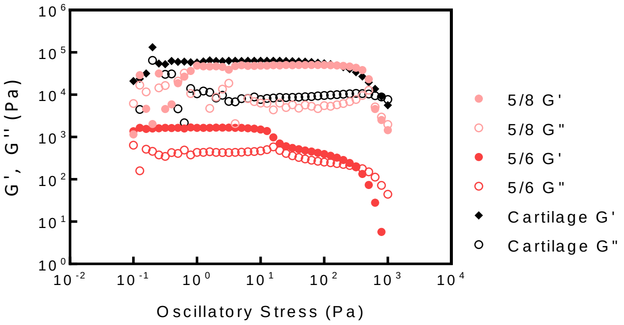

Figure B.1. Oscillatory stress sweep (1 Hz) indicated that high nSi compositions approached the storage and loss moduli of native cartilage with the application of shear stress.

APPENDIX C

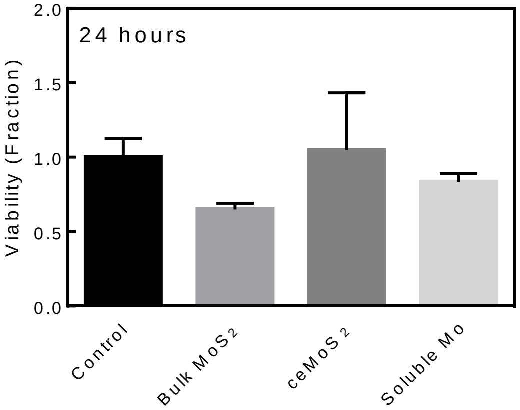

Figure C.1. MTT assay of hMSCs exposed to MoS_2 leachable materials. Bulk MoS_2 showed the greatest change in cell viability following a 24 hour exposure to materials isolated within a transwell membrane. Soluble Mo had an equivalent impact on cell health as ceMoS_2, indicating the negative cell response at high concentrations may be related to stress imparted by physical binding to the cell surface.